Does Size Matter? Exploring the Viability of Measuring the Charge Radius of the First Excited Nuclear State in Muonic Zirconium

by

Benjamin Wilkinson-Zan

Bachelor of Science, Carleton University, 2018

A Thesis submitted in Partial Fulfillment of the Requirements for the Degree of

MASTER OF SCIENCE

in the Department of Physics and Astronomy

We acknowledge with respect the Lekwungen peoples on whose traditional territory the university stands and the Songhees, Esquimalt and W̱SÁNEĆ peoples whose historical relationships with the land continue to this day.

Does Size Matter? Exploring the Viability of Measuring the Charge Radius of the First Excited Nuclear State in Muonic Zirconium

by

Benjamin Wilkinson-Zan

Bachelor of Science, Carleton University, 2018

Supervisory Committee

Dr. Maxim Pospelov, Supervisor
Department of Physics and Astronomy

Dr. Adam Ritz, Departmental Member
Department of Physics and Astronomy

Abstract

From the point of view of the electromagnetic interaction, empirical descriptions of the nucleus involve only a few parameters, one of the most important being the nuclear charge radius. This has been well measured for ground state nuclei, but it is difficult to measure for excited states, since they decay too quickly for conventional methods to be used. We study the atomic transitions in muonic ^{90}Zr and find that the nuclear charge radius of the first excited state can be inferred by measuring the gamma emissions from certain transitions. We find that with 1keV photon resolution, we can infer a difference between the charge radius of the nuclear ground state and first excited state as small as 0.13%. We will work in units where $\hbar = c = 4\pi\epsilon_0 = 1$ so that $e^2 = \alpha \approx 1/137$ (unless otherwise specified). Mass, momentum, and energy will have units of eV, whereas distances will be given in eV^{-1}. In qualitative discussion, we will sometimes revert to discussing distances in meters due to the familiarity of typical scales (e.g. nuclear radius, Bohr radius). When working with 4-vectors in Minkowski space, we use the metric convention $(+,-,-,-)$.

Table of Contents

Supervisor Committee ii

Abstract iii

Table of Contents iv

List of Figures vi

List of Tables viii

Acknowledgements ix

Dedication x

1 Introduction 1
- 1.1 Basics of Atomic Physics . . . 1
- 1.2 The hydrogen-like Atom . . . 3
- 1.3 Photon Transitions . . . 4
- 1.4 Describing the Nucleus . . . 9
- 1.5 The Electric Monopole Transition between Nuclear States . . . 9
- 1.6 The Isotope of Interest, ^{90}Zr . . . 9
- 1.7 A Qualitative Description of the Process . . . 11

2 E0 transition in Electronic Zr 13
- 2.1 The Electric Monopole (E0) Transition . . . 13
- 2.2 A Simple Interaction Model for the Electric Monopole Transition . . . 15
- 2.3 The Non-Relativistic Coulomb Wave Correction . . . 16
- 2.4 The Relativistic Wavefunction Correction . . . 17
- 2.5 Other Corrections . . . 21
- 2.6 Comparison of the Two Methods . . . 22

3 Populating the Excited Nuclear State 24
- 3.1 The Pointlike Nuclear Approximation . . . 24
- 3.2 The Finite Nuclear Charge Distribution . . . 28
- 3.3 Numerical Solutions . . . 30
  - 3.3.1 The Numerov Method . . . 30
  - 3.3.2 Boundary Conditions for the Wavefunctions . . . 31
  - 3.3.3 Calculating the Potential . . . 32
  - 3.3.4 Finding The Energy Eigenstates . . . 33
  - 3.3.5 Numerical Solutions for the Fermi Charge Distribution . . . 35
- 3.4 Finite Size Branching Ratios . . . 39
  - 3.4.1 A Closer Look at the Finite Size Effects . . . 41

4 Decay Modes for Muonic Nuclear De-excitation 45
- 4.1 The Magnetic Dipole Transition . . . 46
  - 4.1.1 Computing the Matrix Element . . . 48
  - 4.1.2 The Muonic Zirconium Transition . . . 53
  - 4.1.3 Calculating the Decay Rate . . . 53
- 4.2 The Two Photon Transition . . . 54
- 4.3 The Two Photon Transition for the Perturbed Muonic Zirconium State . . . 58
  - 4.3.1 Improvements on the Calculation . . . 64

4.4 Comparison to the Electron Electric Monopole Transition 64
4.5 A Quick Note on Parity Violating Effects 65

5 Transition Energy Variation due to Excited Nuclear Charge Radius **67**

6 Conclusion **69**

Bibliography **70**

List of Figures

1.1 The first few s-wave and p-wave radial wavefunctions for the hydrogen atom. 4
1.2 The schematic decay diagram for the muonic zirconium atom. The dotted arrow represents the most common atomic decays. The top solid arrow represents a decay that can populate the nuclear excited state, studied in chapter 3, and the bottom solid arrow represents the decays which can de-excite the nucleus, studied in chapters 2 and 4. 12

2.1 The first two s-wave states solutions of the Dirac and Schrödinger equations for $Z = 40$. The large component Dirac solutions, $f(r)$, are comparable to the Schrödinger solutions as suggested by Eq. 2.32, but we note that the Dirac solutions are divergent near the origin. We can also see that the small component Dirac solutions, $g(r)$ are smaller than the large component solutions by a factor of 6.5 for the case of $Z = 40$. 19

3.1 The Fermi charge distribution for the nucleus of Zirconium. The diffuseness parameter of red and yellow curves has been doubled and halved, for comparison. The normalization of the distribution has been taken to be $\rho = 1$ for simplicity, since it does not affect the curve shape. 28
3.2 The potential found from the Fermi charge distribution is nearly identical to the Coulomb potential outside the nuclear charge radius, but differs significantly as we move towards the origin. 33
3.3 The ground state radial wavefunction for the Coulomb potential ($Z = 40$), and the numerical solutions found by altering the energy guess very slightly. The blue curve represents an energy guess too large by 10^{-7}%, and the red curve represents an energy guess too small by the same amount. 34
3.4 Numerical and pointlike radial wavefunctions for the first two s-wave states of ^{90}Zr. 37
3.5 Numerical and pointlike radial wavefunctions for the first two p-wave states of ^{90}Zr. 38
3.6 Percent variations in energy eigenvalues when altering the number of steps and step size in the Numerov method. The deviations are calculated with respect to the average over all trials. 38
3.7 Perturbed initial and final wavefunctions are shown above. The solid lines connect the states with non-zero E1 matrix elements 39
3.8 The first two s-wave states for pointlike and finite size nuclear distributions. The radial coordinate is scaled by $a_{Z,\mu}^{-1}$ and the radial wavefunctions are scaled by $a_{Z,\mu}^{-3/2}$. 42
3.9 The integrands appearing in the radial matrix elements for pointlike and finite size nuclear distributions. Note that the 2p-1s radial matrix element is more significantly affected by the finite size nuclear effects. The radial coordinate is scaled $a_{Z,\mu}^{-1}$ and the radial wavefunctions are scaled by $a_{Z,\mu}^{-3/2}$. 42
3.10 The integrands appearing in the perturbative mixing matrix elements for pointlike and finite size nuclear distributions. Note that we have scaled the potential by its strength parameter B. The suppression of the finite size nuclear integrand near the origin is due to the factor of r^2 appearing in the spherical volume element. 43

4.1 Perturbed initial and final wavefunctions 45
4.2 Feynman diagrams for the 2E1 matrix element. ω and ω' represent the energies of the two emitted photons. 54
4.3 Analytic radial matrix elements for various values of fractional photon energy. 60
4.4 Radial wavefunctions for the continuum states, for momentum $0 \leq q \leq 5$. We have zoomed in on the region $0 \leq r \leq 5$ to better show the oscillation rate of higher momentum waves. 61
4.5 The first figure (left) displays the "spreading" effect of the r^3 term on the muonic 1s wavefunction, and compares the size of the resulting function to the size of two continuum radial wavefunctions. The second figure (right) displays the oscillatory behaviour of the radial integrand for the same two continuum radial wavefunctions. The momentum values are chosen so that the resulting value of the integral is near the peak ($q = 0.5$) of the spectrum in figure 4.3, where as the other is far out on the tail to the right ($q = 5$) 62

4.6 The first figure (left) displays the comparison between the analytic and computational methods used to compute the momentum integrand, $A_{PL}(q)$ for a few different values of the fractional photon energy y. Note that the analytic results are the same as those displayed above in figure 4.3, and we have now included the computational results derived using the discretization discussed above. We have only shown momentum values $q \in (0, 1)$ to better display the differences between the analytic and computational results. The second figure (right) displays the same momentum integrand, but as applied to the muonic zirconium transition, $A_{FS}(q)$. The differences arise due to the different energy ratio that appears in the denominator (cf. Eq. 4.93) and the fact that we are using the finite size s-wave states. We show the integrand for momentum values $q \in (0, 2)$ to highlight the differences, since the integrand displays similar suppression for $q \geq 2$ as in the regular two photon case. 62
4.7 Dimensionless differential decay rate for the regular hydrogen-like $2s \to 1s$ and muonic zirconium two photon transition, using intermediate p-wave bound states up to n = 5 ($n_{max} = 5$) 63

List of Tables

3.1 Numerical Energies for the Muonic Nuclear Ground State 36
3.2 Contributions to the 2p→1s Transition Rate due to Mixing with Various States 40
3.3 Comparison of the Pointlike and Finite Size Effects in the Branching Ratios to Populate the Excited Nuclear State 43
3.4 Comparing the Pointlike and Finite Size Effects 44

4.1 Numerical energies for the M1 transition 53
4.2 Numerical Values for Radial Integral 54
4.3 Two Photon transition rates for Hydrogen, varying the total number of p-wave states considered . 59

Acknowledgements

I would like to thank:

Dr. Maxim Pospelov for his guidance, being patient and letting me understand concepts instead of pushing through calculations, and his willingness to walk me through steps when I was stuck.

The UVic Theory Group for providing an excellent atmosphere to pursue topics of our own interest, and for creating a space where we could not only acquire knowledge, but also develop our ability to communicate science.

Maheyer, Seamus, Alberto, Kate, Rafi, Sam, and Saeid for keeping things light-hearted and fun, even when we struggled on courses or concepts.

Dedication

To my parents, Steve and Della, who inspire me scientifically.
To my brother, Nathan, who inspires me creatively.
To my partner, Alex, who inspires me emotionally.

Chapter 1

Introduction

1.1 Basics of Atomic Physics

Ernest Rutherford is most famously known for his gold-foil experiment [1] conducted in the early 20^{th} century, where α particles were shot at a thin gold foil. The accepted atomic model was J.J. Thompson's "plum-pudding" model, in which the negatively charged electrons sat as "plums" (or raisins) in a "pudding" of positive charge. When Rutherford's students shot the positively charged α particles through the foil, most passed through largely unaffected, but a small portion was deflected at a large angle, sometimes back towards the α emitter. Rutherford concluded that the atom was mostly empty space, with the positive charge concentrated in a very small region in the center, the nucleus.

The nucleus is so small compared to the orbiting electrons so that it often seems to act as a pointlike particle, but realistically the nucleus has a finite size. The radius of the nucleus is on the femtometer scale (10^{-15}m), four orders of magnitude smaller than the atomic scale of hydrogen (10^{-11}m). Although the pointlike nucleus is an excellent approximation in many cases, we will be interested in studying the finite size effects of the nucleus on its orbiting particles. Although the nucleus is composed of protons and neutrons (each composed of quarks), for the purpose of this research we will describe the nucleus as a single entity.

The most simple way to imagine a classical finite size nucleus is the neutrons and protons interlocking to form an object similar to a ball. If we instead view the nucleus from a quantum picture (as we should) the ball becomes blurry, reflecting the inherent uncertainty in the position and momentum of each of the nucleons. In particular, there is a non-zero probability (albeit extremely small) for the individual nucleons to be found far outside what we would classically think of the edge of the ball.

How should we describe the nucleus, if we can't know the position and momentum of its components? We can focus on the average distribution of the nucleons within the nucleus, and model the nucleus based on these average parameters. Since we want to model the nuclear effect on the orbiting particles via the Coulomb force, we will be interested in modeling the nuclear charge. In this fuzzy ball model, there are three main parameters. Firstly, the total charge of the nucleus, given by the number of protons Z. The second is the nuclear charge distribution $\rho(r)$, which describes how the charge is distributed "within" the nucleus. The third is the nuclear charge radius R_{Nuc}, which describes the "radius" of the fuzzy ball. We should pause to comment on the notion of the "radius" of the fuzzy ball. Based on the qualitative discussion above, the ball is fuzzy because it has no well defined edge. Returning to the classical model, the nucleus is a sphere of charge, so that the charge radius is simply the distance where the charge density falls from a finite value to zero. In the fuzzy picture, the charge density does not fall immediately at the edge, but instead drops to zero over a short distance. In this case we will refer to the radius as the value where the charge density is half of its maximum value.

A short time after Rutherford's experiment, Neils Bohr proposed a model of the atom which came to be known as the Bohr atom [2]. He employed Rutherford's idea of a small nucleus, but Bohr's model was special because it proposed that the electrons orbiting the nucleus could only exist at discrete energy levels. The electrons could jump from one energy level to another, emitting only fixed energies in the process. Although it was soon outdated by more accurate models the fundamental principles of discrete energy levels was an important step in the development of quantum mechanics, and it did predict the correct energy levels of the basic atoms.

Just over a decade later, Erwin Schrödinger came up with one of the most famous equations in physics [3], which became one of the main starting points to describe quantum mechanics. For a particle in a single spatial dimension labeled by x, the Schrödinger equation can be written as

$$i\frac{\partial\Psi(x,t)}{\partial t} = -\frac{1}{2m}\frac{\partial^2}{\partial x^2}\Psi(x,t) + V(x,t)\Psi(x,t) \tag{1.1}$$

where m is the mass of the particle, $V(x,t)$ is the potential, and the function $\Psi(x,t)$ is called the wavefunction, from which physical quantities can be computed. Its complex square modulus can be interpreted as the spatial

probability distribution for the particle of interest, and is thus normalized so that

$$\int |\Psi(x,t)|^2 dx = 1 \tag{1.2}$$

The generalization to three dimensions is straightforward by including second partial derivatives for the other spatial coordinates, so that we have

$$i\frac{\partial \Psi(\mathbf{r},t)}{\partial t} = -\frac{1}{2m}\boldsymbol{\nabla}^2\Psi(\mathbf{r},t) + V(\mathbf{r},t)\Psi(\mathbf{r},t) \tag{1.3}$$

where $\boldsymbol{\nabla}^2 = \partial^2/\partial x^2 + \partial^2/\partial y^2 + \partial^2/\partial z^2$ is the Laplacian in cartesian coordinates. The normalization condition is now taken over the total spatial volume V so that

$$\int_V |\Psi(\mathbf{r},t)|^2 dV = 1 \tag{1.4}$$

If we have a time independent potential, then we can separate the time dependence in the wavefunctions, writing

$$\Psi_j(\mathbf{r},t) = \psi_j(\mathbf{r})e^{-iE_j t} \tag{1.5}$$

where the states ψ_j for a complete set of stationary states, each one satisfying

$$-\frac{1}{2m}\boldsymbol{\nabla}^2\psi_j(\mathbf{r}) + V(\mathbf{r})\psi_j(\mathbf{r}) = E_j\psi_j(\mathbf{r}) \tag{1.6}$$

The general solution is written as a linear combination of the solutions above

$$\Psi(\mathbf{r},t) = \sum_j c_j\psi_j(\mathbf{r})e^{-iE_j t} \tag{1.7}$$

We can simplify the equations further if we are dealing with a spherically symmetric potential. For completeness, we will work in spherical coordinates

$$\begin{aligned} x &= r\sin\phi\sin\theta \\ y &= r\cos\phi\sin\theta \\ z &= r\cos\theta \end{aligned} \tag{1.8}$$

with $\theta \in [0,\pi)$ and $\phi \in [0,2\pi)$. In this case we can write the Laplacian in spherical coordinates and use separation of variables to split the time independent Schrödinger equation into an angular equation and a radial equation (see for example [4, 5, 6]). The radial solutions will depend on the potential of interest, but the solutions to the angular part do not depend on the potential or energy levels, so they can be applied any time we have spherical symmetry. The angular solutions are the spherical harmonics, $Y_{l,m}(\theta,\phi)$ where l is the orbital angular momentum, taking values $0 \leq l < n$ (n is the principle or radial quantum number, which takes natural number values, $n = 1, 2, 3, ...$), and m is its component along any spatial direction (typically chosen to be the z-axis), taking values $-l \leq m \leq l$. For completeness, the normalized spherical harmonics are given by

$$Y_{l,m}(\theta,\phi) = (-1)^{\frac{1}{2}(m+|m|)}\sqrt{\frac{2l+1}{4\pi}\frac{(l-|m|)!}{(l+|m|)!}}e^{im\phi}P_l^m(cos\theta) \tag{1.9}$$

where $P_l^m(\cos\theta)$ are the associated Legendre functions

$$P_l^m(x) = (1-x^2)^{|m|/2}\left(\frac{d}{dx}\right)^{|m|}\left[\frac{1}{2^l l!}\left(\frac{d}{dx}\right)^l (x^2-1)^l\right] \tag{1.10}$$

The function in the square brackets is often written $P_l(x)$, and is the l-th Legendre polynomial. The spherical harmonics are orthonormal, meaning

$$\int_0^{2\pi}\int_0^{\pi} [Y_{l',m'}(\theta,\phi)]^*[Y_{l,m}(\theta,\phi)]\ sin\theta\ d\theta\ d\phi = \delta_{ll'}\delta_{mm'} \tag{1.11}$$

In order to simply notation, we will often write these angular integrals using the solid angle Ω as follows

$$\int f(\theta,\phi)d\Omega \equiv \int_0^{2\pi}\int_0^{\pi} f(\theta,\phi)\ sin\theta\ d\theta\ d\phi \tag{1.12}$$

Upon separation of variables, the radial equation takes the form

$$\frac{d}{dr}\left(r^2\frac{dR_{nl}(r)}{dr}\right) - 2mr^2[V(r) - E_{nl}]R_{nl}(r) = l(l+1)R_{nl} \tag{1.13}$$

In general the energies and radial wavefunctions will depend on both the principle quantum number n as well as the orbital angular momentum l, but not explicitly on the z-component m. With a change of variable $u(r) \equiv rR(r)$, we can bring the radial equation into a more convenient form, resembling the original one dimensional Schrödinger equation (cf. eq. 1.1)

$$-\frac{1}{2m}\frac{d^2u_{nl}(r)}{dr} + \left[V(r) + \frac{1}{2m}\frac{1(l+1)}{r^2}\right]u_{nl}(r) = E_{nl}u_{nl}(r) \tag{1.14}$$

We can interpret the term in square brackets as an effective potential, resulting from the combination of the radial potential and the centrifugal term $l(l+1)/2mr^2$. We can rewrite the radial wavefunction normalization in terms of this new function

$$\int_0^\infty |R_{nl}(r)|^2 r^2 dr = \int_0^\infty |u_{nl}(r)|^2 dr = 1 \tag{1.15}$$

This redefinition is useful as the final form of the Schrödinger equation is cleaner. Furthermore the lack of any linear derivatives of $u(r)$ (in contrast to those in $R(r)$) allows the development of an algorithm for numerical solutions that is very accurate as we will see in section 3.3. In order to make more progress on solutions, one needs to specify the potential and solve the radial equation.

1.2 The hydrogen-like Atom

There exist very few potentials for which the Schrödinger equation can be exactly solved, yielding closed formed solutions for the energy eigenstates and eigenvalues. The hydrogen-like atom is one such case, where the potential is given by the spherically symmetric Coulomb potential

$$V(r) = -\frac{Z\alpha}{r} \tag{1.16}$$

Physically this represents a pointlike nucleus with Z protons and a single orbiting electron. The typical approach is to expand the radial eigenfunctions in a power series and solve for the recursion relation to find the power series coefficients [4, 5, 6]. After properly normalizing the wavefunctions, one finds the solutions

$$R_{nl} = \sqrt{\left(\frac{2}{na_Z}\right)^3 \frac{(n-1-1)!}{2n[(n+l)!]^3}}\left(\frac{2r}{na_Z}\right)^l [L_{n-l-1}^{2l+1}(2r/na_Z)]e^{-r/na_Z} \tag{1.17}$$

where L_{n-l-1}^{2l+1} are the associated Laguerre polynomials, n is the principal quantum number, l is the orbital angular momentum. Lastly, the characteristic orbital distance of the hydrogen-like atom is given by the Bohr radius

$$a_Z = \frac{1}{Z\alpha m} = \frac{\hbar}{Z\alpha mc} \tag{1.18}$$

where the second equation is in SI units, and $\alpha \approx 1/137$ is the fine structure constant. The first few s-wave and p-wave radial wavefunctions are plotted in figure 1.1. Note that the s-wave states are far more likely to be near the origin, and for higher principle quantum numbers n, the states are on average further from the origin.

To be more precise, the mass factor appearing in the Bohr radius and hence the radial wavefunctions is the reduced mass of the nucleus, m_N, and the orbiting particle, m,

$$m_{red} = \frac{m_N m}{m_N + m} \tag{1.19}$$

For the case of hydrogen, $m_e = 9.109 \times 10^{-31}$kg, $m_N = m_p = 1.673 \times 10^{-27}$kg, so we find the reduced mass to be $m_{red} = 9.104 \times 10^{-31}$kg $\approx m_e$. Because the nucleus (proton) is much heavier than the electron, the reduced mass effects are very small, and we can approximate the reduced mass of the system to be equal to the electron mass.

For an electron orbiting hydrogen ($m_e = 9.109 \times 10^{31}$kg, $Z = 1$), we find a Bohr radius of 5.29×10^{-11}m. Heavier particles orbit closer to the atom, and a nucleus with higher charge Z will also cause the orbit to be smaller. It's important to note that we should not think of the electron as orbiting on a fixed path with a certain orbital radius, as we do in classical mechanics. Since we are dealing with quantum mechanics, all we can do is assign probabilities for the electron to be at any given place. Quantifying this statement, the probability of finding

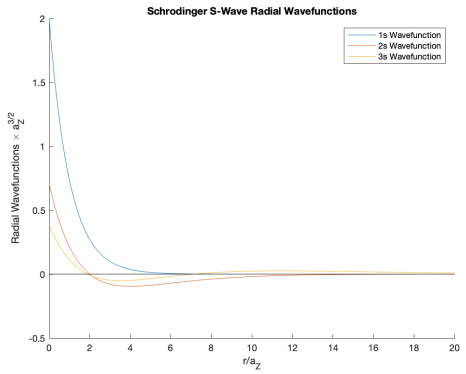

(a) S-Wave Solutions

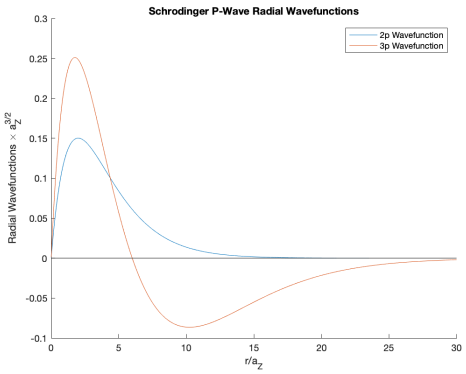

(b) P-Wave Solutions

Figure 1.1: The first few s-wave and p-wave radial wavefunctions for the hydrogen atom.

the electron in the radial interval $[r, r+dr]$ is given by $r^2|R_{nl}(r)|^2 dr$. In this way the average radial distance can be calculated by taking the average over all possible positions. For the hydrogen-like atom, we find [5]

$$\langle R_{nl}|r|R_{nl}\rangle = \int_0^\infty R^*_{nl}(r) r R_{nl}(r) r^2 dr = \frac{a_Z}{2}[3n^2 - l(l+1)] \tag{1.20}$$

We see that the average distance is always proportional to the Bohr radius. States with higher radial quantum numbers will be found, on average, further from the nucleus, and states with higher orbital angular momentum, will be found, on average, closer to the nucleus. By solving the radial equation we also find the energy eigenstates. In this case, the energies are defined so that negative energies represent particles which are bound to the nucleus, whereas positive energy solutions represent particles which feel the effect of the Coulomb potential, but are not bound to the nucleus (more on this later). The larger the absolute value of the energy, the more bound the particle is to the nucleus. The energy spectrum for the bound eigenstates form a discrete spectrum, increasing linearly with particle mass and quadratically with nuclear charge

$$E_n = -\frac{(Z\alpha)^2}{2n^2} m \tag{1.21}$$

The discretization of allowed energy levels is one of the drastic departures from classical mechanics. An atom undergoing a transition in which the state of the orbiting particle changes from a known initial state to a known final state will emit a fixed amount of energy. There are a variety of ways in which this energy can be carried away, but we now turn to the case where it is carried away by a photon. The photon is a spin one particle, so it has at least one unit of total angular momentum, and hence by conservation of angular momentum the initial and final states must differ by at least one unit of angular momentum. In the next section, we will come to understand these statements more precisely. Although this discussion was in the context of a particle orbiting the nucleus, the same rules apply to any system where angular momentum is conserved. We will also be interested in applying them to transitions directly involving the nucleus.

Unlike the hydrogen-like atom, the electron wavefunctions for atoms with multiple electrons cannot be solved analytically since the Coulomb potential introduces electron-electron repulsion. There are a variety of approximations used to treat this problem, see Gasiorowicz Ch.14 [5] for an introduction.

1.3 Photon Transitions

One of the main tools we have for studying atomic and nuclear structure is analyzing the radiation emitted in a transition, where the system "jumps" from a state to another with lower energy (or equivalent absorbs a photon and transitions to a higher energy state). Not only does the energy of the photon(s) provide information about the energy levels of the system, but the type of photon can provide information about the initial and/or final states. Photons can be classified by their parity and total angular momentum. If these are conserved quantities in our system of interest, only certain types of photons can mediate transitions between the initial and final state.

Before discussing the parity and angular momentum, we briefly introduce some review some terminology, following Landau and Lifshitz [7]. The photon field is a four-vector $A^\mu = (\Phi, \boldsymbol{A})$, where Φ is the scalar potential and $\boldsymbol{A}$ is the vector potential. As in classical electrodynamics, we are free to alter the potential by choosing a gauge transformation of the form $A_\mu \to A_\mu + \partial_\mu \chi$, with χ is an arbitrary scalar function of the coordinates and time. We will work in the transverse gauge, where the wave equation for the photon field in free space is given by

$$\frac{\partial^2 \mathbf{A}}{\partial t^2} - \nabla^2 \mathbf{A} = 0 \tag{1.22}$$

The general solution using the plane wave ansatz, and normalizing our wavefunction so that we have one photon in a volume $V = 1$ yields

$$A^{\mu}_{\mathbf{k}}(\mathbf{r}, t) = \sqrt{4\pi}\frac{e^{\mu}}{\sqrt{2\omega}}e^{-i\omega t + i\mathbf{k}\cdot\mathbf{r}} \tag{1.23}$$

where e^{μ} is the unit polarization four vector, ω is the photon energy, and $\mathbf{k}$ is its momentum (or wavenumber), related by the dispersion relation $|\mathbf{k}| = \omega$. Since we are working in the transverse gauge, the polarization vector takes the form

$$e^{\mu} = (0, \mathbf{e}), \qquad \mathbf{e}\cdot\mathbf{k} = 0 \tag{1.24}$$

We will return to this later when we are interested in the photon wavefunctions for definite values of the angular momentum.

It is impossible to distinguish the photon's spin and orbital angular momentum. Spin can be thought of as the angular momentum when the particle is at rest, but the photon is massless and therefore cannot be at rest, so this interpretation fails. We can also note that we typically associate spin with the mathematical transformation properties of the vector wavefunction of interest, but this fails because choosing a gauge for the photon field necessarily breaks this symmetry, for more details see Vol 4 of Landau and Lifshitz [7]. Hence only the total angular momentum of the photon has meaning, which can take non-zero positive integer values. However, we still speak of the photon spin s and its orbital angular momentum l, but the context is different. We say the photon has spin 1 because it is a vector quantity. We will usually perform an expansion of the photon wavefunction in terms of the spherical harmonics Y_{lm} and the orbital angular momentum corresponds to the value of l of the term in this expansion. In this manner the photon has at least one unit of angular momentum because it is a spin one particle, but it can have higher values depending on the order of the spherical harmonics. Due to the properties of the spherical harmonics, the number l also defines the parity of the photon, according to

$$P_{ph} = (-1)^{l+1} \tag{1.25}$$

The expansion mentioned above is typically done as a multipole expansion, and we classify the photons based on their total angular momentum j as well as the parity. A photon with angular momentum j and parity $(-1)^j$ is called an electric 2^j-pole (or Ej) photon. A photon with angular momentum j and parity $(-1)^{j+1}$ is called a magnetic 2^j-pole (or Mj) photon.

In order to find the wavefunctions of the electric and magnetic photons, we need to know the eigenfunctions of $\mathbf{J}$ and j_z. This corresponds to finding the spherical harmonic vectors $\mathbf{Y}_{lm}$, which satisfy $\mathbf{J}^2\mathbf{Y}_{lm} = j(j+1)\mathbf{Y}_{lm}$, and $j_z\mathbf{Y}_{lm} = m\mathbf{Y}_{lm}$, with z referring to a specific Cartesian coordinate axis. It turns out that the solutions are given by [7]

$$\begin{aligned} \mathbf{Y}^{(e)}_{jm} &= \frac{1}{\sqrt{j(j+1)}}\boldsymbol{\nabla}_{\boldsymbol{n}}Y_{jm}, & P &= (-1)^j \\ \mathbf{Y}^{(m)}_{jm} &= \mathbf{n}\times\mathbf{Y}^{(e)}_{jm}, & P &= (-1)^{j+1} \\ \mathbf{Y}^{(l)}_{jm} &= \mathbf{n}Y_{jm}, & P &= (-1)^j \end{aligned} \tag{1.26}$$

where $\mathbf{n} = \mathbf{r}/r$, and $\nabla_{\mathbf{n}} = |\mathbf{k}|\nabla_{\mathbf{k}}$ which acts on functions which depend only on the direction of $\mathbf{n}$. For completeness, in spherical coordinates its two components are given by

$$\nabla_{\mathbf{n}} = \left(\frac{\partial}{\partial\theta}, \frac{1}{sin\theta}\frac{\partial}{\partial\phi}\right) \tag{1.27}$$

The parities of the eigenfunctions have been listed to the right. The superscript e, m, and l refer to the fact that the first two will be the elctric and magnetic photons which are both transverse, whereas the last function $\mathbf{Y}^{(l)}_{jm}$ is longitudinal. The vector $\mathbf{Y}^{(m)}_{jm}$ can be written as a linear combination of the scalar spherical harmonics Y_{lm} of order $l = j$ only. The other two spherical harmonics vectors can be written as linear combinations of the scalar spherical harmonics with $l = j \pm 1$. This can be observed by comparing the parities, noting that the parity of the scalar harmonics is $(-1)^{l+1}$.

We now turn to the photon wavefunctions. Due to our transversality condition, we can only use $\mathbf{Y}^{(e)}_{jm}$ and $\mathbf{Y}^{(m)}_{jm}$, since $\mathbf{Y}^{(l)}_{jm}$ is longitudinal. If we want an Ej photon, we must choose the vector spherical harmonic with parity $(-1)^j$, which is clearly $\mathbf{Y}^{(e)}_{jm}$. Similarly the Mj photon has parity $(-1)^{j+1}$, so we must choose $\mathbf{Y}^{(m)}_{jm}$. Hence the wavefunction for a photon with definite angular momentum j and z-component m with energy ω is given by

$$\mathbf{A}_{\omega jm}(\mathbf{k}) = \frac{4\pi^2}{\omega^{3/2}}\delta(|\mathbf{k}| - \omega)\mathbf{Y}_{jm}(\mathbf{n}) \tag{1.28}$$

where the specific spherical harmonic vector is chosen for either the electric or magnetic case. The normalization is different from what we previously considered (cf. eq. 1.23) because this is the momentum space wavefunction

of the photon, which is related to the coordinate space representation by a fourier transform. Note that the delta function enforces the photon's dispersion relation $|\mathbf{k}| = \omega$.

So far we have been working in the transverse gauge, where the scalar potential satisfies $\Phi = 0$, and we have only worked on the magnetic potential $\mathbf{A}$. If we choose to work in another gauge, the magnetic photon wavefunction is left unchanged because none of the other components have the same parity. However the electric photon can be written as a linear combination in the following way

$$\begin{aligned} \mathbf{A}^{(e)}_{\omega jm}(\mathbf{k}) &= \frac{4\pi^2}{\omega^{3/2}}\delta(|\mathbf{k}| - \omega)(\mathbf{Y}^{(e)}_{jm} + C\mathbf{n}Y_{jm}) \\ \Phi^{(e)}_{\omega jm}(\mathbf{k}) &= \frac{4\pi^2}{\omega^{3/2}}\delta(|\mathbf{k}| - \omega)CY_{jm} \end{aligned} \tag{1.29}$$

Now that the photon wavefunctions are known, we can evaluate electric and magnetic multipole transition rates. We quickly pause to introduce Dirac's equation and the corresponding fermion solutions. We do not offer a complete discussion here, just the basics needed. For further discussion, there are a number of textbooks with significantly more detail, for example [7, 8]. Dirac's equation is the relativistic extension of the Schrödinger equation for fermions. For a particle of mass m, charge e, which feels an external field with four potential A_μ, Dirac's equation is given by

$$[\gamma^\mu(p_\mu - eA_\mu) - m]\psi = 0 \tag{1.30}$$

where p is the 4 momentum operator $p_\mu = (i\partial/\partial t, \boldsymbol{\nabla})$, ψ is the (4-component) wavefunction, and γ are the Dirac matrices,

$$\gamma^0 = \begin{pmatrix} I_2 & 0 \\ 0 & -I_2 \end{pmatrix}, \qquad \boldsymbol{\gamma} = \begin{pmatrix} 0 & \boldsymbol{\sigma} \\ -\boldsymbol{\sigma} & 0 \end{pmatrix} \tag{1.31}$$

Here I_2 is the 2x2 identity matrix, and $\boldsymbol{\sigma} = (\sigma_1, \sigma_2, \sigma_3)$ is the vector formed by the three pauli matrices. It should be emphasized the that the notation $\boldsymbol{\gamma}$ implies there are 3 spatial 4x4 gamma matrices, each formed with the respective pauli matrix. It is obvious to see that the Dirac equation includes the spin of the particle. We thus expect that the energy levels are spin dependent, in contrast to the Schrödinger theory where spin dependent energy contributions are only introduced via perturbations. Although we will not derive it, a low velocity expansion, $v < 1$, yields the Schrödinger equation plus 3 extra terms (up to order $1/c^2$) [7]. The first two are the relativistic kinematic and spin-orbit perturbations, and the third is the Darwin term, which can be thought of (in the non-relativistic framework) as the smearing of the potential due to the inherent uncertainty of the particles position. We will give more details on these perturbations in section 3.3.

To understand the interaction between a Dirac fermion and a photon, we use the term $-ej^\mu_{fi}A_\mu$ found in the Lagrangian in classical electrodynamics. Here $j^\mu_{fi} \equiv \psi^*_f\gamma^\mu\psi_i = (\psi^*_f\psi_i, \psi^*_f\gamma^0\boldsymbol{\gamma}\psi_i)$ is the electromagnetic current, and A_μ is the photon wavefunction. For the purposes of the quantum interaction, we replace the operators by their quantum counterparts, so that the matrix element for such an interaction takes the form

$$\begin{aligned} V_{fi} &= e\int d^3x\ j^\mu_{fi}(\boldsymbol{r})A^*_\mu(\boldsymbol{r}) \\ &= e\int d^3x\ j^\mu_{fi}(\boldsymbol{r})\int \frac{d^3k}{(2\pi)^3}A^*_\mu(\boldsymbol{k})e^{-i\boldsymbol{k}\cdot\boldsymbol{r}} \end{aligned} \tag{1.32}$$

We have omitted the subscripts (ωjm) from the photon wavefunction for simplicity. Suppose we are interested in the emission of a photon with definite values of angular momentum j, and its component m in some direction z. Furthermore, we will suppose it is an electric photon, so we use the wavefunctions given in eq. 1.29. We will take the arbitrary constant $C = -\sqrt{(j+1)/j}$. This choice will cause a cancellation of the spherical harmonics of order $j-1$ from the contribution of the spatial components of the photon wave function ($\boldsymbol{A}$). Compared to the contribution from $A^0 = \Phi$, this is a higher order in a_0/λ (where λ is the photon wavelength), which includes spherical harmonics of the lowest order j. Hence we take our photon wavefunction as

$$A^\mu = (\Phi, \mathbf{0}), \qquad \Phi(\mathbf{k}) = -\sqrt{\frac{j+1}{j}}\frac{4\pi^2}{\omega^{3/2}}\delta(|\mathbf{k}| - \omega)Y_{jm} \tag{1.33}$$

We now substitute this photon wavefunction into our matrix element (eq. 1.32) and integrating over the delta function giving

$$\begin{aligned} V_{fi} &= e\int d^3x\ \psi^*_f(\boldsymbol{r})\psi_i(\boldsymbol{r})\int \frac{d^3k}{(2\pi)^3}\left[-\sqrt{\frac{j+1}{j}}\frac{4\pi^2}{\omega^{3/2}}\delta(|\mathbf{k}| - \omega)Y_{jm}\right]^* e^{-i\boldsymbol{k}\cdot\boldsymbol{r}} \\ &= -e\sqrt{\frac{j+1}{j}}\frac{\sqrt{\omega}}{2\pi}\int d^3x\ \psi^*_f(\boldsymbol{r})\psi_i(\boldsymbol{r})\int d\Omega_k Y^*_{jm}(\boldsymbol{n}_k)e^{-i\boldsymbol{k}\cdot\boldsymbol{r}} \end{aligned} \tag{1.34}$$

To evaluate the angular part of the momentum integral, we use the plane wave expansion

$$e^{i\boldsymbol{k}\cdot\boldsymbol{r}} = 4\pi \sum_{l=0}^{\infty} \sum_{m'=-l}^{l} i g_l(kr) Y^*_{lm'}(\boldsymbol{n}_k) Y_{lm'}(\boldsymbol{n}_r) \tag{1.35}$$

where $\boldsymbol{n}_{k,r}$ are the unit vectors in momentum and position space, respectively. The functions $g_l(kr) = \sqrt{\pi/2kr} J_{l+1/2}(kr)$ are the spherical Bessel functions, which are related to the Bessel function of the first kind $J_\alpha(x)$, having the expansion

$$J_\alpha(x) = \sum_{n=0}^{\infty} \frac{(-1)^n}{n!\Gamma(n+\alpha+1)} \left(\frac{x}{2}\right)^{2n+\alpha} \tag{1.36}$$

The plane wave expansion is useful because we can now use the orthonormal properties of the spherical harmonics to evaluate the angular integral. Integration over $d\Omega_k$ will give Kronecker deltas $\delta_{jl}\delta_{mm'}$, and then the summations in the Bessel expansion will pick out the term with $l = j$ and $m' = m$. In other words

$$\int d\Omega_k Y^*_{jm}(\boldsymbol{n}_k) e^{-i\boldsymbol{k}\cdot\boldsymbol{r}} = 4\pi i^j g_j(kr) Y^*_{jm}(\boldsymbol{n}_r) \tag{1.37}$$

so that the matrix element becomes

$$V_{fi} = -2ei^j \sqrt{\omega} \sqrt{\frac{j+1}{j}} \int d^3x \; \psi^*_f(\boldsymbol{r}) \psi_i(\boldsymbol{r}) g_j(kr) Y^*_{jm}(\boldsymbol{n}_r) \tag{1.38}$$

At this point the integral could be computed numerically, but we can also impose some physical constraints in order to simplify the integral. Schematically, the characteristic scale of the radial orbitals is given by the Bohr radius, which scales as $a_0 = 1/Z\alpha m$. The transition occurs between two energy levels in the atom, so the wavelength scales as $\lambda \sim 1/E \sim 1/(Z\alpha)^2 m$. Hence the product of the momentum and the radial distance scales as $ka_0 \sim a_0/\lambda \sim Z\alpha < 1$. Given that we expect our wavefunctions to localized around the nucleus with roughly exponential decay of characteristic radial scale equal to the Bohr radius, the integrand will only be significant for $kr \ll 1$ (for $Z\alpha \ll 1$). This allows us to perform a Taylor expansion on the functions $g_j(kr)$, keeping the first term

$$g_j(kr) \approx \frac{(kr)^j}{(2j+1)!!} \tag{1.39}$$

It is important to note that this expansion is also valid up to order $(kr)^{j+1}$. This is because the Bessel functions have a power series expansion about 0 which is either in odd or even powers (depending on the index l, see eq. 1.36). Naively we expect that the term containing $(kr)^j$ will proportional to $(a_0/\lambda)^j \sim (Z\alpha)^j$ so that the next order term will give a contribution of order $(Z\alpha)^2$ smaller. Hence we find, using $Y_{j,-m} = (-1)^{j-m} Y^*_{jm}$

$$V_{fi} = -2ei^j \frac{\omega^{j+1/2}}{(2j+1)!!} \sqrt{\frac{(2j+1)(j+1)}{\pi j}} (Q^{(e)}_{j,-m})_{fi} \tag{1.40}$$

where

$$(Q^{(e)}_{jm})_{fi} = \sqrt{\frac{4\pi}{2j+1}} \int d^3x \; \psi^*_f(\boldsymbol{r}) \psi_i(\boldsymbol{r}) r^j Y_{jm}(\boldsymbol{n}_r) \tag{1.41}$$

are called the 2^j-pole electric transition moments of the system. Applying Fermi's golden rule $\Gamma = \int 2\pi |V_{fi}|^2 \delta(E_i - E_f - \omega) d\omega$ and integrating over ω to set the photon energy yields the probability of Ej radiation

$$\Gamma^{(e)}_{jm} = \frac{2(2j+1)(j+1)}{j[(2j+1)!!]^2} \omega^{2j+1} |(Q^{(e)}_{j,-m})_{fi}|^2 \tag{1.42}$$

Before studying this in more depth, we look at the lowest case, corresponding to $j = 1$ ($j = 0$ is not possible because the photon must have at least one unit of total angular momentum). The above formula reduces to

$$\begin{aligned} \Gamma^{(e)}_{1m} &= \frac{4\omega^3}{2} e^2 |(Q^{(e)}_{1,-m})_{fi}|^2 \\ &= \frac{4\alpha\omega^3}{2} \left| \int d^3x \; \psi^*_f(\boldsymbol{r}) \psi_i(\boldsymbol{r}) \left[\sqrt{\frac{4\pi}{3}} r Y_{1m}(\boldsymbol{n}_r) \right] \right|^2 \end{aligned} \tag{1.43}$$

To work on the term inside the square bracket, we note that by writing the spherical harmonics and rearranging, we find

$$\begin{aligned}\sqrt{\frac{4\pi}{3}}rY_{10}(\boldsymbol{n}_r) &= z \\ \sqrt{\frac{4\pi}{3}}rY_{1,\pm1}(\boldsymbol{n}_r) &= \mp\frac{i}{\sqrt{2}}(x \pm iy)\end{aligned} \tag{1.44}$$

Summing over m in eq. 1.43 above to find the transition rate to all final states, we have

$$\begin{aligned}\Gamma^{(e)} &= \sum_m \frac{4\alpha\omega^3}{2}\left|\int d^3x\ \psi_f^*(\boldsymbol{r})\psi_i(\boldsymbol{r})\left[\sqrt{\frac{4\pi}{3}}rY_{1m}(\boldsymbol{n}_r)\right]\right|^2 \\ &= \frac{4\alpha\omega^3}{2}(|\langle x\rangle|^2 + |\langle y\rangle|^2 + |\langle z\rangle|^2) \\ &= \frac{4\alpha\omega^3}{2}|\langle \boldsymbol{r}\rangle|^2 \\ &= \frac{4\omega^3}{2}|\langle \boldsymbol{d}\rangle|^2\end{aligned} \tag{1.45}$$

where $\boldsymbol{d} = e\boldsymbol{r}$ is the electric dipole operator. This is the probability for a transition involving an electric dipole photon, or the E1 transition. The formula is the same in the non-relativistic case [5], except that we would replace the Dirac wavefunctions with the Schrödinger wavefunctions.

Each successive term in the multipole expansion above contains another power of r. Hence we would expect the radial integral in the Ej transition probability to scale as $a_0^j/\lambda^j \sim (Z\alpha)^j$, up to some constants which are dependent on the initial and final states. Given that $Z\alpha \ll 1$, the dipole transition will dominate over the other decay modes. In some cases, the dipole transition is forbidden, so we must calculate the leading non-zero transition. To understand why some transitions might be forbidden, we turn to the angular integral.

The angular integral in the 2^j-pole electric transition moments contains a spherical harmonic of order j. Recall this represents a photon of total angular momentum j. If the initial system has total angular momentum j_i and final angular momentum j_f, then by vector addition of angular momentum rules, we must have

$$|j_i - j_f| \leq j \leq j_i + j_f,\ j \neq 0 \tag{1.46}$$

Furthermore, the components m_i and m_f must satisfy $m_i - m_f = m$.

Another selection rule is obtained by studying the parity of the system. Parity is conserved by EM interactions, so if the parity of the initial state is P_i and that of the final state is P_f with P_{ph} being the photon parity, we have $P_i = P_f P_{ph}$. Since parity only takes the values ±1, we can rewrite this as $P_i P_f = P_{ph}$. Recall we found that the parity of an electric photon is $P_{ph} = (-1)^j$, so we must have

$$P_i P_f = (-1)^j,\ \text{Electric } 2^j \text{ photon} \tag{1.47}$$

A similar analysis can be done for the emission of a magnetic photon. The idea is similar, using instead the magnetic photon wavefunction, but the derivation is a bit more complicated. We will postpone it until section 4.1 where we will use it. We note that the same angular momentum selection rules apply to magnetic photons, but since the parity of the magnetic photon is $P_{ph} = (-1)^{j+1}$, we have

$$P_i P_f = (-1)^{j+1},\ \text{Magnetic } 2^j \text{ photon} \tag{1.48}$$

These selection rules are very powerful, if we know the initial and final parities and angular momentum, we can immediately see that some multipole transition modes are forbidden. Consider the atomic transition $2s_{1/2} \to 1s_{1/2}$ in Hydrogen. We have $P_i = P_f = 1$, so we require $P_{ph} = 1$. Right away we can see that the electric dipole ($j = 1$) is forbidden because the E1 photon has parity -1. It turns out no electric photon can mediate the $2s_{1/2} \to 1s_{1/2}$ transition. The only way to achieve a change of angular momentum of at least 1 is if the electron spin flips, as initial and final states are both s waves. Opposite spin states are orthogonal, and the electric photon provides no operator that interacts with the electron spin. Conversely the magnetic dipole transition ($j = 1$) could mediate this transition because it has the correct parity, and contains the Pauli matrices which can mediate a spin flip. Since the M1 transition is the first term in the magnetic photon expansion, we might expect it would be the dominant transition between these electron states of hydrogen, since the other terms would be further suppressed by higher orders in $Z\alpha$. However it turns out that the radial integral in the M1 transition is strongly suppressed, and a second order perturbative approach dominates, the two photon transition (2E1) [7]. Both the magnetic and electric decays developed above are first order in the photon perturbation (they both contain a single photon matrix element). We will study both the M1 and 2E1 transitions in a similar atomic transition in chapter 4.

1.4 Describing the Nucleus

The main issue with describing the nucleus analytically is that we cannot solve quantum many body problems. There has been some recent computational advancement, but we still cannot achieve nucleon wavefunctions for higher mass nuclei ($A > 16$, [9]). For higher mass nuclei we typically describe the nucleus as if it acts as a single particle. Although this contains far less information about the nuclear structure than the nucleon wavefunctions, we will find it sufficient under certain approximations and assumptions, and it is certainly easier to work with. Along with the charge radius R_{Nuc}, total charge Z, and its spatial distribution $\rho(r)$, we will also describe the nucleus by the nuclear spin I and parity π. It is not uncommon that the charge distribution contains only a few parameters, one being the charge radius, with some only requiring the charge radius. Hence the charge radius is one of the fundamental parameters for this empirical description. If the spin and parity of the state are already known, the charge radius is the next most important parameter.

The neutrons and protons have their own respective spin, and the nuclear spin is the vector sum of the individual angular momentum of each of the nucleons. There are several forces in the empirical description of the nucleus [10], including the nuclear pairing force which causes the nucleons to couple together in spin-0 states. An important result is that nuclei with an even number of nucleons will have a spin-0 ground state. In a similar manner to spin, the total nuclear parity is determined by multiplying the parity of the individual nucleons, with + denoting even parity and - denoting odd parity. We typically use the notation I^{π} to describe the spin and parity of the nucleus. For example the notation 0^+ indicates that the nucleus is in a spin 0 state with even parity.

Just as the orbiting leptons may be excited to higher energy states, the nucleus can also be excited to a higher energy state. These excited states have been observed during a muonic cascade [11] and also by scattering charged particles on the nucleus [12, 13]. A nuclear excited state can be formed by moving an individual nucleon to a higher energy orbit, by exciting a vibrational or rotational mode of a pair of nucleons, or breaking apart a pair of nucleons. Due to this extra energy exciting some mode, the excited nuclear states will have a slightly larger charge radius.

There is a huge variation in the lifetime of excited nuclear states. We shall be interested in an excited state which has a half life of roughly 60ns. Because the lifetime is so short, we cannot use traditional techniques to determine the nuclear charge radius. The goal of this research will be to determine if atomic transitions can provide insight on the nuclear charge radius of the excited state.

Given that we are interested in quantifying nuclear and orbiting lepton states, we should pause to develop notation. In general we will use Dirac's bra-ket notation to describe both, with the usual $|nlm\rangle$ notation for the leptonic states. We will use $|N\rangle$ to describe the two nuclear states of interest, with $|0\rangle$ denoting the nuclear ground state, and $|1\rangle$ denoting the excited nuclear state. As an example, the notation for the combined system of the nuclear being in its first excited state and the orbiting lepton to be in the $2s$ state is $|200\rangle|1\rangle$. If we do not mention the nuclear state at all it is understood that the nucleus is in the ground state (e.g. muonic 2s state implies $|200\rangle|0\rangle$). Likewise if only the nuclear state is mentioned, it is assumed that the muon is in the ground state (e.g. a comment about the nuclear excited state would imply the $|100\rangle|1\rangle$ state).

1.5 The Electric Monopole Transition between Nuclear States

Since the energy gaps between nuclear states are typically much larger than the corresponding binding energies, a transition between different nuclear states can result in an electron being ejected from the atom. Such transitions are called internal conversion, and were first studied in the 1920's [14]. It was realized that internal conversion was due to the direct electromagnetic interaction between the nucleus and an electron, and was not mediated via the emission and reabsorption of an actual photon. In the early 1950's, it was realized that the internal conversion process was dependent on the finite size of the nucleus in two ways. Firstly, the electron wavefunctions are modified within the nucleus due to the difference in the potential. Furthermore, the existence of penetration matrix elements was discovered as a result of the penetration of electrons into the nucleus.

The penetration matrix elements led to new phenomena, such as the electric monopole (E0) transition. This transition, which is mediated between two nuclear states having the same spin, has no single gamma transition counterpart due to conservation of angular momentum. In particular, between two 0^+ nuclear states, single gamma transitions are forbidden, and the E0 transition can be the most dominant transition. Since E0 transitions depend solely on this penetration effect, they are sensitive to the nuclear structure, including its charge radius.

1.6 The Isotope of Interest, ^{90}Zr

We will be studying the stable ^{90}Zr isotope, often containing a muon as one of its orbiting particles. The nucleus is composed of 40 protons and 50 neutrons. The reason for the muon will become clear in the next section, but for now we focus on the nuclear properties of ^{90}Zr. The most important characteristic of interest is that both its ground state and first excited state are 0^+ states, which severely constrains its decay modes. The first excited

state sits 1760.71MeV above the ground state, and has a half life of 61.3ns [15]. With regard to the angular selection rules previously mentioned, this implies that the decay cannot proceed by any of the single photon transitions discussed above, both the initial and final states are spin 0. The most common transition is an electric monopole transition (where the nucleus interacts directly with an electron, ejecting it from the atom), followed by electron-positron pair production. Two photon nuclear de-excitation is also possible, but vastly subdominant [16].

Note that the nuclear excitation energy is far larger than the binding energy of an electron orbiting the nucleus

$$\begin{aligned} E_{b,Z=40,e} &= 0.5(Z\alpha)^2 m_e = 0.022\text{MeV} \\ a_{Z=40,e} &= \frac{1}{Z\alpha m_\mu} = 6.70\text{MeV}^{-1} \\ a_{Z=40,e} &= \frac{\hbar}{Z\alpha m_\mu c} = 1.32 \times 10^{-12}\text{m (SI)} \end{aligned} \tag{1.49}$$

The Bohr radius has been included for the purpose of comparison with a muon below. The monopole transition ejects one of the innermost bound electrons into the continuum states, with final energy much larger than the binding energy.

Suppose instead that one of the innermost electrons is replaced by a muon. Atoms with an orbiting muon are called muonic atoms and we will refer to zirconium with a bound muon as muonic zirconium. The muon has charge -1e, and is a heavier version of the electron, with mass $m_\mu = 105.658$MeV, approximately 207 times the mass of the electron. Since the muon is much heavier, it may seem like reduces mass effects may be more significant, but the zirconium nucleus is also far heavier than the hydrogen nucleus. Using Eq. 1.19, with a proton mass of 938.27MeV and a neutron mass of 939.57MeV, we see that the reduced mass of the muonic zirconium system is $m_{red} = 105.526\text{MeV} \approx m_\mu$. Therefore the reduced mass effects are not significant, and we can approximate them by using the muon mass. In order to distinguish between the two leptons, we will often use the subscript e or μ to denote quantities related to the electron or the muon, respectively. If we do not want to distinguish between the two, we will simply leave out the subscript. For example $a_{Z,e}$ refers to the Bohr radius of an electron bound to a nucleus with Z protons whereas $a_{Z,\mu}$ refers to the Bohr radius of a muon bound to a nucleus with Z protons, and lastly a_Z refers to the Bohr radius of either system. Because the muon is much heavier, it has a larger binding energy and a smaller Bohr radius

$$\begin{aligned} E_{b,Z=40,\mu} &= 0.5(Z\alpha)^2 m_\mu = 4.50\text{MeV} \\ a_{Z=40,\mu} &= \frac{1}{Z\alpha m_\mu} = 0.0324\text{MeV}^{-1} \\ a_{Z=40,\mu} &= \frac{\hbar}{Z\alpha m_\mu c} = 6.40 \times 10^{-15}\text{m (SI)} \end{aligned} \tag{1.50}$$

There are two important things to note. Firstly the binding energy of muonic zirconium is larger than the nuclear excitation energy by a factor of three. In particular, the energy different between the ground state (1s) and the next lowest state (2s) using the hydrogen-like, pointlike approximation is 3.38MeV, which is still larger than the nuclear excitation energy. This has an important implication: if the atom is in the state $|100\rangle|1\rangle$, that is, the muon is in the ground state and the nucleus is in the first excited state, it can only decay to the full ground state, $|100\rangle|0\rangle$, purely based on energy conservation. We need both the ground and nuclear excited states to be 0^+, otherwise de-excitation via a single gamma transition would likely dominate, and we also need the excited nuclear state to be the next accessible energy state in the muonic case, so that it cannot decay to the nuclear ground state and a muonic p-wave state. Zirconium is the only atom which satisfies both these considerations. Although nuclear excitations in muonic systems have been previsouly studied, no one has addressed the $0^+ \to 0^+$ transition in a muonic system. Along with probing the nuclear structure via spectroscopy of muonic atoms, we are also able to make the first predictions comparing the rates of electronic vs muonic modes for nuclear de-excitation.

The second important thing to note is that the Bohr radius of muonic zirconium is on the same scale as the nuclear radius. Because the muon and the nucleus are quantum objects, the radius is not a fixed value of their distance, simply a characteristic scale at which they are most likely to be found. In reality, they spend time at radii both smaller and larger then this characteristic scale, implying that the muon samples the Coulomb potential from the nucleus over a range of distances. Since the nuclear radius is on the same scale as the Bohr radius, the muon is significantly more likely to sample the potential within the nucleus compared to the electron. In the pointlike approximation, the probability of finding the 1s state at the origin is proportional to the cube of the Bohr radius, which means the muon is more likely to be found at the origin by a factor of

$$\left(\frac{a_{Z,e}}{a_{Z,\mu}}\right)^3 = \left(\frac{m_\mu}{m_e}\right)^3 \approx 200^3 = 8 \times 10^6 \tag{1.51}$$

Hence muonic atoms are much more sensitive to the effects of finite nuclear size since they are approximately 8 million times more likely to be found at the origin. Muonic atoms have been the subject of significant study

because they currently are the most precise source of information about the charge distribution of nuclei (see for example [17, 18]). In particular, choosing a muonic atom with a higher nuclear charge Z increases the Coulomb force and hence pulls the muon closer to the nucleus. Given that ^{90}Zr has 40 protons, it is a useful muonic atom to study, but the primary reason is that the only nuclear de-excitation mode is a $0^+ \to 0^+$ transition in the muonic system.

Because the muonic Bohr radius and the nuclear radius are on the same scale, we need to take into account the finite size effects of the nucleus. We will see in the next section that this cannot be done in a perturbative manner, and numerical methods are used to find the muon wavefunctions.

As noted above, the only kinematically available decay from the excited nuclear state is to the full ground state. Once the muon is attached to the nucleus, we can treat it as a spin 1/2 object. Then we can consider the possibility of a forbidden magnetic dipole transition as a mode of nuclear de-excitation. Although we will not analyze it here, forbidden M1 transitions in muonic atoms can be used as a first step towards experimentally constraining parity violating operators. Recall that the E0 transition and the M1 transition are very slow in comparison to other atomic transitions. It is possible that a parity violating operator arising from a neutral current could cause a transition to an intermediate state, which could then decay via a much quicker atomic transition. Measurements (or lack thereof) of this quick transitions could give information and constraints into these parity violating operators.

1.7 A Qualitative Description of the Process

Before diving into the technical details and computations, we quickly summarize the goal of the research, and the effects we expect.

From classical electrodynamics, we know that a charged particle inside a uniform sphere of charge feels no force. Given that both the ground state and first excited state of zirconium are spin zero, they will have radially symmetric charge distributions [14]. Hence the muon only feels the potential of the charge distribution within its radius. The total charge enclosed within its radius is at most the total nuclear charge Z, but will be smaller if the muon is within the nucleus. Therefore the muon feels a smaller potential on average, and is thus less bound to the nucleus. We thus expect to find a different energy spectrum than the hydrogen-like pointlike approximation, and in particular each energy should be smaller in absolute value. On a side note, since states with non-zero angular momentum are suppressed near the origin, we would expect these states to be less affected by this change.

If we consider the transition from the $|100\rangle|1\rangle$ state to the $|100\rangle|0\rangle$ state in muonic zirconium, we know that there will be a change in energy corresponding to nuclear de-excitement of 1760.71keV. This was measured using electronic zirconium (i.e. zirconium with oribiting electrons), which are far less likely to be found near the nucleus (compared to their muonic counterparts) and hence do not feel finite size effects significantly. On the other hand, muonic zirconium is sensitive to the finite size effects. In the $|100\rangle|0\rangle$ state, the muon will be bound to the nucleus with energy $E_b(R_{Nuc})$, where we are being explicit in noting that the binding energy depends on the charge radius as discussed above. On the other hand the muon in the $|100\rangle|0\rangle$ state will be bound with energy $E_b(R_{Nuc} + \Delta R) \equiv E_b(R_{Nuc}) - \Delta E$. That is, the muon is bound slightly less ($\Delta E > 0$) since the radius of the excited nuclear state is slightly larger. This means that in the muonic $|100\rangle|1\rangle \to |100\rangle|0\rangle$ transition, the actual transition energy will be $E = 1760.71\text{keV} + \Delta E$. This is schematically depicted in figure 1.2. If this transition is be observed with sufficient energy resolution to determine ΔE, then we can infer the charge radius of the excited nuclear state. Alternatively, if we can't determine ΔE, it places a constraint on the charge radius of the excited nuclear state.

Before attempting to observe this transition, we need to understand what mediates this transition, and how often this transition would occur given current experimental set-ups. In Chapter 2 we investigate the nuclear de-excitation in electronic zirconium, and develop a model to analyze the muonic system. In Chapter 3 we investigate how the excited nuclear state can be populated, and how often this occurs. In Chapter 4 we investigate the mechanism for the nuclear de-excitation of muonic zirconium and compare it to the electronic case. Lastly, in Chapter 5 we study how significant the difference in the excited nuclear charge radius has on the energy difference ΔE. In other words, if our detectors are have a certain energy resolution, what is our experimental sensitivity to the change in charge radius of the excited nuclear state.

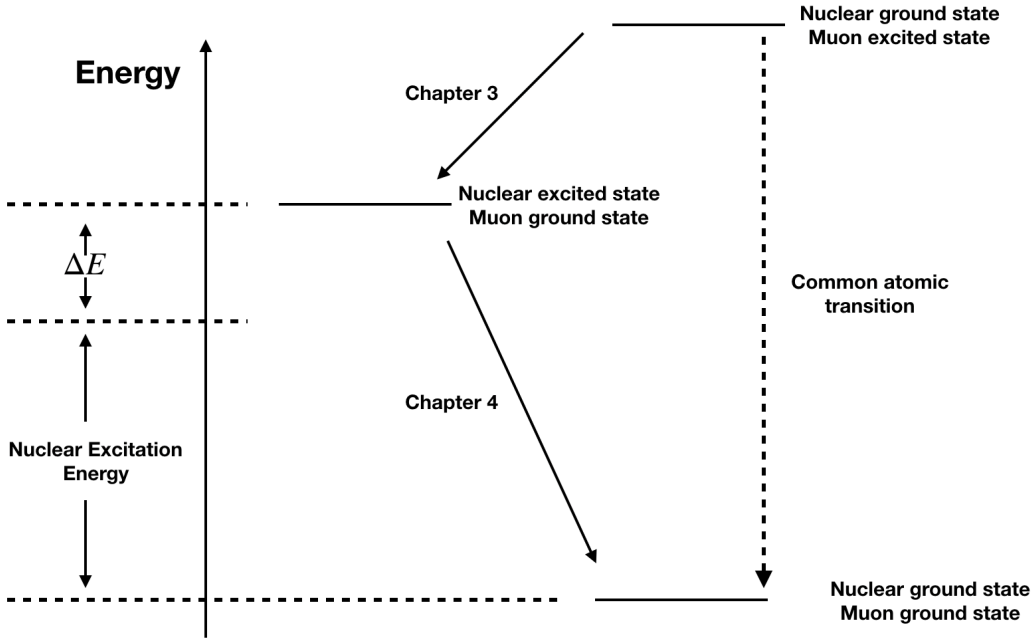

Figure 1.2: The schematic decay diagram for the muonic zirconium atom. The dotted arrow represents the most common atomic decays. The top solid arrow represents a decay that can populate the nuclear excited state, studied in chapter 3, and the bottom solid arrow represents the decays which can de-excite the nucleus, studied in chapters 2 and 4.

Chapter 2

E0 transition in Electronic Zr

2.1 The Electric Monopole (E0) Transition

The nuclear de-excitation in electronic zirconium has been previously studied, which gives us the energy of nuclear de-excitation $E_{Nuc} = 1760.71\text{keV}$ as well as the half life $T_{1/2} = 61.3\text{ns}$ [15]. We will now investigate this transition in order to understand how we can use this to model muonic zirconium later. Recall we are interested in a nuclear transition $0^+ \to 0^+$. As we just saw, it is impossible for a single photon to mediate this transition, due to the conservation of angular momentum. We first provide a review of the E0 transition, which is slightly different from our approach. There are, however, common factors in both which will allow us to compare our approach later and ensure it is consistent.

Church and Weneser [19] model the E0 transition using the Coulomb force. They write the total Hamiltonian as

$$H = H(\text{Nuclear}) + \left[H(\text{electron}) - \alpha \sum_e \int d\tau \frac{q(r)}{|\mathbf{r} - \mathbf{r}_e|}\right] + \left[\alpha \sum_e \int d\tau \frac{q(r)}{|\mathbf{r} - \mathbf{r}_e|} - \sum_{p,e} \frac{\alpha}{|\mathbf{r}_p - \mathbf{r}_e|}\right] \tag{2.1}$$

The first term represents the interactions of protons and neutrons in the nucleus. The second is the electrons' self-interaction as well as their interaction with the average charge distribution, where $q(r)$ is the average nuclear charge distribution. The third, including the individual Coulomb interactions between protons and electrons, is treated perturbatively for the E0 transition. We need an operator that can connect the otherwise orthogonal nuclear states so the only choice is the very last term, which depends on both the proton coordinates $\mathbf{r}_p$ as well as the electron coordinates $\mathbf{r}_e$. For $r_p \ll r_e$, we proceed by expanding the potential using the Laplace expansion [20]:

$$\begin{aligned} \frac{1}{|\mathbf{r}_p - \mathbf{r}_e|} &= \sum_{l=0}^{\infty} \sum_{m=-l}^{l} (-1)^m \frac{4\pi}{2l+1} \frac{r_p^l}{r_e^{l+1}} Y_{l,-m}(\theta, \phi) Y_{l,m}(\theta', \phi') \\ &\approx \frac{1}{r_e} \end{aligned} \tag{2.2}$$

Here the primes refer to angles with respect to $\mathbf{r}_e$, and the non-primes refer to angles with respect to $\mathbf{r}_p$. In the second line, we have only included the $l = 0$ term, which we will denote as V_{E0}, where $E0$ stands for electric monopole. In the opposite case where $r_e \ll r_p$, the sum can be approximated by $1/r_p$. The interaction process where the electron is ejected from the atom is referred to as internal conversion, and the $l = 0$ term corresponds to the electric monopole interaction. Using the notation discussed in the intro with $|i\rangle$ and $|f\rangle$ representing the electron initial and final state respectively, the Laplace expansion allows us to write the matrix element as

$$\langle 0|\langle i|V_{E0}|f\rangle|1\rangle = -\alpha \sum_{p,e} \left[\int d\tau_{Nuc} \int_0^{r_p} d\tau_{el} \phi_0^* \psi_f^* \frac{1}{r_p} \phi_1 \psi_i + \int d\tau_{Nuc} \int_{r_p}^{\infty} d\tau_{el} \phi_0^* \psi_f^* \frac{1}{r_e} \phi_1 \psi_i\right] \tag{2.3}$$

where ψ are the electronic wavefunctions and ϕ are the nuclear wavefunctions, which are the product of all proton wavefunctions. Consider the second term:

$$\begin{aligned} \int d\tau_{Nuc} \int_{r_p}^{\infty} d\tau_{el} \phi_0^* \psi_f^* \frac{1}{r_e} \phi_1 \psi_i &= \int d\tau_{Nuc} \int_0^{\infty} d\tau_{el} \phi_0^* \psi_f^* \frac{1}{r_e} \phi_1 \psi_i - \int d\tau_{Nuc} \int_0^{r_p} d\tau_{el} \phi_0^* \psi_f^* \frac{1}{r_e} \phi_1 \psi_i \\ &= -\int d\tau_{Nuc} \int_0^{r_p} d\tau_{el} \phi_0^* \psi_f^* \frac{1}{r_e} \phi_1 \psi_i \end{aligned} \tag{2.4}$$

The first integral on the right hand side vanishes because the nuclear wavefunctions are orthogonal, and the result of the electron wavefunction integral is independent of the any nuclear operators since the limits are

constants. Thus we can write the matrix element as

$$\begin{aligned}\langle 0|\langle i|V_{E0}|f\rangle|1\rangle &= -\alpha\sum_{p,e}\int d\tau_{Nuc}\int_0^{r_p} d\tau_{el}\phi_0^*\psi_f^*\left(\frac{1}{r_p}-\frac{1}{r_e}\right)\phi_1\psi_i \\ &= -\alpha\sum_{p,e}\int d\tau_{Nuc}\int_0^{r_p} dr_{el}\phi_0^* R_f^*\left(\frac{r_e^2}{r_p}-r_e\right)\phi_1 R_i\int d\Omega_{el}Y_{f,el}Y_{i,el} \\ &= -\alpha\sum_{p,e} R_f^*(0)R_i(0)\frac{1}{6}\int d\tau_{Nuc}\int_0^{r_p} dr_{el}\phi_0^* r_p^2\phi_1 \\ &= -\frac{\alpha}{6}R_f^*(0)R_i(0)R_N^2\rho\end{aligned} \tag{2.5}$$

where R_N is the nuclear radius, and ρ is the nuclear strength parameter, defined by

$$\rho \equiv \sum_p \int d\tau_{Nuc}\phi_0^*\left(\frac{r_p}{R_N}\right)^2\phi_1 \tag{2.6}$$

Since the electron's characteristic distance scale is much larger than the nuclear radius ($a_Z \gg r_p$), the radial wavefunctions $R_{f,i}(r)$ do not vary significantly during the integrand, so we have replaced them by their value at the origin. Later we will see that the Dirac wavefunctions are divergent at the origin, so we will modify this by evaluating the wavefunctions at the nuclear radius. In the second line, we have made it explicit that the angular integral evaluates to unity due to normalization, and only the radial wavefunction is left ($R_{i,f}$). If we were to expand our wavefunctions as a power series in the electron's radial coordinate instead of taking its constant value at the origin, we would find higher order terms of r_p/R_N appearing in the integrand of ρ [19]. This is important if one seeks to use relativistic wavefunctions found using numerical methods for a finite size nucleus, however the approximation of using the Coulomb wavefunctions evaluated at the nuclear radius is a common choice.

Church and Weneser separate the total decay rate as the product of the square of the nuclear strength parameter ρ, and the electronic factor Ω_K, which is defined as $\Omega_K \equiv \Gamma/\rho^2$. The electronic factor is independent of the spin of nuclear states, and can be calculated if the radial wavefunctions are known. Note that the nuclear charge distribution will affect the electronic radial wavefunctions, so that the electronic factor is not completely independent of the nuclear structure. The nuclear strength parameter is largely independent of the electron wavefunctions, but can be affected by higher order terms in the radial wavefunction expansion, as described above. In general the nuclear strength parameter cannot be calculated because the proton wavefunctions are unknown. Instead it is found by measuring the decay rate Γ and calculating the electronic factors as follows

$$\Omega_K = 2(2\pi)\int\frac{d^3p}{(2\pi)^3}|\langle 0|\langle i|V_{E0}|f\rangle|1\rangle|^2\delta(E-E_{Nuc}-E_i)/\rho^2 \tag{2.7}$$

The first factor of two is due to the two electrons in the $1s$ state which can be ejected from the transition. In principle any initial state can give a contribution (not just the 1s state) but the 1s states provide the dominant effect, since they have the largest overlap at the origin. The other s-wave states can also contribute a reasonable amount, but non s-wave states are very suppressed due to their r^l behaviour near the origin. The rest of the decay rate expression is an application of Fermi's golden rule, integrated over the momentum phase space as the final particle is a continuum state.

The total decay rate is given by

$$\Gamma_{E0} = 2(2\pi)\int\frac{d^3p}{(2\pi)^3}|\langle 0|\langle i|V_{E0}(L=0)|f\rangle|1\rangle|^2\delta(E-E_{Nuc}-E_i) \tag{2.8}$$

The integration measure d^3p can be converted into spherical momentum space coordinates. As there is no angular dependence in the decay rate, the angular integral gives an additional factor of 4π. We are then left with $p^2dp = pEdE$, which follows from the relativistic dispersion relation $p = \sqrt{E^2-m_e^2}$, so that

$$\frac{dp}{dE} = \frac{E}{\sqrt{E^2-m_e^2}} = \frac{E}{p} \Rightarrow pdp = EdE \tag{2.9}$$

Note that a fully non-relativistic treatment would use the dispersion relation $E = p^2/2m_e$, yielding $pdp = m_e dE$. Hence the fully non-relativistic calculation involves replacing E by the mass of the electron, and non-relativistic limits involve taking (amonst other things) the limit $E_f \to m_e$, where E_f is the final energy of the

ejected electron. The integral over the delta function is now trivial, yielding

$$\begin{aligned}\Gamma_{E0} &= \frac{(4\pi)(4\pi)}{(2\pi)^3}\left|-\frac{\alpha}{6}R_f^*(0)R_i(0)R_N^2\rho\right|^2\int dE\ pE\delta(E-E_{Nuc}-E_i)\\ &= \frac{\alpha^2}{18\pi}p_fE_f|R_f(0)R_i(0)|^2R_N^4\rho^2\\ &= \frac{8\pi\alpha^2}{9}p_fE_f|\psi_f(0)\psi_i(0)|^2R_N^4\rho^2\end{aligned} \tag{2.10}$$

where $E_f = E_{Nuc} - E_i$ and p_f are the energy and momentum of the ejected electron. The decay rate depends on the nuclear strength parameter ρ^2, which is typically on the order of 10^{-3}. For the case of ^{90}Zr, Kibédi and Spear [21] give an experimental value $\rho^2 = 3.46(14)\times10^{-3}$, with the numbers in parenthesis indicating the uncertainties in the final digits.

2.2 A Simple Interaction Model for the Electric Monopole Transition

For simplicity, we will first study our interaction model in a very simple case, and later add in more complications. In the most simple case, we will treat the nucleus as a pointlike particle, and the electron as a plane wave. Since the electron cannot interact with the nucleus via a photon, the electron must be physically present at the nucleus for the interaction to occur. We do not seek to model the nuclear wavefunctions, so our potential will only explicitly include operators which act on the electron states. The nuclear matrix element will be included via a constant strength parameter. This implies that the potential is composed of two parts, the first being the constant strength parameter, and the second must evaluate the probability for the electron to be found at the nucleus. If we treat the nucleus as point-like, the potential governing the E0 transition is a 3D delta function, $V_p(\mathbf{r}) = B\delta^3(\mathbf{r})$, where B determines the strength of the interaction, and the subscript p denotes the perturbative nature of the potential. We will later develop an expression linking B to the nuclear strength parameter of Church and Weneser. It is obvious that the matrix element picks out the values of the final and initial state wavefunctions at the origin. Because the nuclear de-excitation energy is much larger then the electron binding energy $E_f = E_{Nuc} - E_b \gg 0$, the final state can be approximated by a plane wave. Here we normalize by one particle in a box with volume V, however the volume factor from the matrix element cancels with the volume factor from the phase space, so we neglect it for now. Apart from this volume factor the plane wave evaluates to unity at the origin, so the contribution to the matrix element is solely due to the initial 1s electron state, with wavefunction

$$\psi_{100}(r,\phi,\theta) = \frac{1}{\sqrt{\pi}}\left(\frac{1}{a_{Z,e}^3}\right)^{3/2}e^{-r/a_{Z,e}} \tag{2.11}$$

Evaluating the decay rate, we obtain

$$\begin{aligned}d\Gamma_{E0} &= 2(2\pi)|\langle i|B\delta(\mathbf{r})|f\rangle|^2\frac{Vd^3p}{(2\pi)^3}\delta(E-E_{Nuc}-E_i)\\ d\Gamma_{E0} &= 4\pi B^2\left|\int d^3r\frac{1}{\sqrt{\pi}}\left(\frac{1}{a_{Z,e}^3}\right)^{3/2}e^{-r/a_{Z,e}}\delta(\mathbf{r})\frac{1}{\sqrt{V}}e^{-i\mathbf{p}\cdot\mathbf{r}}\right|^2\frac{Vd^3p}{(2\pi)^3}\delta(E-E_{Nuc}-E_i)\\ d\Gamma_{E0} &= 4|B|^2(Z\alpha m_e)^3\frac{d^3p}{(2\pi)^3}\delta(E-E_{Nuc}-E_i)\end{aligned} \tag{2.12}$$

Converting the momentum space integral into spherical coordinate, we find

$$d\Gamma_{E0} = \frac{16\pi}{8\pi^3}|B|^2(Z\alpha m_e)^3pEdE\delta(E-E_{Nuc}-E_i) \tag{2.13}$$

The final integral is now trivial, and sets the electron energy and momentum to their values as dictated by conservation laws. Thus the decay rate is

$$\Gamma_{E0} = \frac{2}{\pi^2}|B|^2(Z\alpha m_e)^3p_fE_f \tag{2.14}$$

where p_f is the momentum of the final state, determined by its energy, $E_f = E_{Nuc} + E_i$. The decay rate can be related to the half-life of the state, $T_{1/2}$ by

$$\Gamma = \frac{\ln(2)}{T_{1/2}} \tag{2.15}$$

which allows us to solve for the coefficient of the delta interaction, B,

$$|B|^2 = \frac{\pi^2}{2}\frac{ln(2)}{T_{1/2}(Z\alpha m_e)^3 p_f E_f} \tag{2.16}$$

Note the basic similarities between this approach and the one previously discussed, they both contain the square of some parameter which represents the nuclear matrix element, and they both depend on the electron's wavefunctions evaluated at the origin as well as the electrons final energy and momentum. The final energy of the ejected electron is the nuclear de-excitation energy minus the binding energy, $E_f = 1738.93$keV, which gives a momentum of $p_f = 1662.15$keV. As mentioned before, the half-life is $T_{1/2} = 61.3$ns, or $9.313 \times 10^{10}\text{keV}^{-1}$, using $\hbar = 6.582 \times 10^{-9}$keV s. This gives $|B|^2 = 2.755 \times 10^{-24}$keV.

We will soon abandon the plane wave approximation for the final state and instead use a more accurate wavefunction. Further accuracy will lead us to incorporate relativistic effects, and take both the initial and final wavefunctions to be solutions of the Dirac equation. In order to simplify notation, it will be convenient to rewrite the result above as a function of the wavefunctions, rather than the parameters upon which they depend. The delta function causes evaluation of both wavefunctions at the origin, so that the decay rate is proportional to the absolute square of both wavefunctions. In turn, the interaction strength parameter, B, is inversely proportional to the decay rate. Factoring out the appropriate constants, we find an expression for the strength parameter:

$$|B|^2 = \frac{\pi}{2}\frac{ln(2)}{T_{1/2}p_f E_f}\frac{1}{|\psi_{100}(0)\psi_f(0)|^2} \tag{2.17}$$

The effect of alterations on the wavefunctions (given that our potential remains a delta function) are now obvious. Before moving onto more precise calculations, there is a correction that needs to be made. When we related the decay rate and the half-life, we implicitly made the assumption that the only (or at least only significant) decay mode was the E0 transition, i.e. $\Gamma_T = \Gamma_{E0}$, where Γ_T is the total decay rate, related to the half-life. However there are two other potentially significant decay modes. The first is de-excitation by two photons, and the second is electron-positron pair production, since the nuclear excitation energy is greater than $2m_e$. Theoretical decay rates for pair production and the E0 transition are given by Thomas [22], whereas the two photon transition is compared to pair production by Oppenheimer [23]. Pair production is found to be significant, with a comparable decay rate to the E0 transition. Two photon emission is suppressed due to the larger energy of the intermediate virtual 1^- nuclear states compared to the energy of the first nuclear excited state, and has been experimentally measured to be very subdominant [16] so we will ignore it from now on. Denoting the E0 decay rate as Γ_{E0} and the pair production decay rate as Γ_{PP}, we have $\Gamma_{E0} \approx 2.54\Gamma_{PP}$ [24]. Incorporating this effect, we have

$$\Gamma = \Gamma_{E0} + \Gamma_{PP} = (1 + 1/2.54)\Gamma_{E0} = 1.39\Gamma_{E0} \tag{2.18}$$

Hence the decay rate of the E0 transition is related to the overall half-life via

$$\Gamma_{E0} = \frac{\ln(2)}{1.39T_{1/2}} \tag{2.19}$$

This factor of 1.39 appears in the interaction strength parameter as well, which becomes

$$|B|^2 = \frac{\pi}{2}\frac{ln(2)}{1.39T_{1/2}p_f E_f}\frac{1}{|\psi_{100}(0)\psi_f(0)|^2} \tag{2.20}$$

We will later see that the probability to populate the excited nuclear state in a muonic atom is proportional to $|B|^2$, so a decrease in B means a loss in statistics for an experimental observation. Unfortunately, most corrections will cause a decrease in this strength parameter, indicating that our simple approximation overestimates the interaction strength.

2.3 The Non-Relativistic Coulomb Wave Correction

For a more accurate result, we could abandon the approximation of using a plane wave for the final state and instead use the positive energy solution to the Schrödinger equation for a Coulomb potential. The free energy Coulomb wavefunctions with momentum $\mathbf{p}$ for this case are given by [6] (note that they use Coulomb units, so the momentum is measured in units of $a_Z^{-1} = Z\alpha m$)

$$\psi_p(\mathbf{r}) = e^{-\pi Z\alpha m_e/2p}\Gamma(1 + iZ\alpha m_e/p)e^{i\mathbf{p}\cdot\mathbf{r}}F(-iZ\alpha m_e/p, 1, ipr - i\mathbf{p}\cdot\mathbf{r}) \tag{2.21}$$

The function $F(a, b, x)$ is the confluent hypergeometric function (also called Kummer's function of the first kind) is defined via

$$F(a, b, x) = \frac{\Gamma(b)}{\Gamma(a)}\sum_{n=0}^{\infty}\frac{\Gamma(a+n)}{\Gamma(b+n)}\frac{x^n}{n!} \approx 1 + \frac{a}{b}x \tag{2.22}$$

The last approximation holds in the case where $|x| \ll 1$. One can quickly note that in the limit of a vanishing potential ($Z\alpha \to 0$), all terms except the exponential reduce to unity, and we are left with the plane wave as expected since no potential exists. With reference our last expression for B (eq. 2.20), we want to calculate the absolute square of this wavefunction, evaluated at the origin. Denoting $x = Z\alpha m_e/p$, we can rewrite this as

$$\begin{aligned}
|\psi_p(\mathbf{0})|^2 &= e^{\pi Z\alpha m_e/p}|\Gamma(1+iZ\alpha m_e/p)|^2 \\
&= e^{\pi x}|\Gamma(1+ix)|^2 \\
&= e^{\pi x}\Gamma(1+ix)\Gamma(1-ix) \\
&= e^{\pi x}(ix)(-ix)\Gamma(ix)\Gamma(-ix) \\
&= e^{\pi x}x\Big[-i(ix)\Gamma(ix)\Gamma(-ix)\Big] \\
&= e^{\pi x}x\left[\frac{\pi}{-i\sin(i\pi x)}\right] \\
&= e^{\pi x}x\left[\frac{\pi}{\sinh(\pi x)}\right] \\
&= \frac{2\pi x}{1-\exp(-2\pi x)} \\
&= \frac{2\pi Z\alpha m_e/p}{1-\exp(-2\pi Z\alpha m_e/p)}
\end{aligned} \tag{2.23}$$

where we have related the Gamma function to the sin function via the identity $sin(\pi x) = -\pi/[x\Gamma(x)\Gamma(-x)]$.

Consider a positive energy particle in a Coulomb potential with momentum much greater than the typical atomic momentum $p \gg Z\alpha m_e$. In this case, the effects of the Coulomb potential are thus negligible (except very close to the origin), and the plane wave approximation should be valid. Our expression above confirms this statement, Taylor expanding the exponential in the high energy limit, corresponding to $p \gg Z\alpha m_e$, shows this correction reduces to unity

$$\frac{2\pi Z\alpha m_e/p}{1-\exp(-2\pi Z\alpha m_e/p)} \xrightarrow{p\gg Z\alpha m_e} \frac{2\pi Z\alpha m_e/p}{1-(1-2\pi Z\alpha m_e/p)} = 1 \tag{2.24}$$

In the case of the electronic ^{90}Zr E0 transition, the final momentum is 1662keV, and the electron mass is 0.511keV, so this correction is

$$|\psi_p(\mathbf{0})|^2 = \frac{2\pi Z\alpha m_e/p_f}{1-\exp(-2\pi Z\alpha m_e/p_f)} = 1.3083 \tag{2.25}$$

Since B depends inversely on this factor, the Coloumb wave correction causes the strength parameter to decrease. This is a fairly small correction (compared to some others that we will see) because the momentum of the ejected electron is large compared to the typical atomic momentum, $Z\alpha m_e/p_f = 0.089 \ll 1$.

2.4 The Relativistic Wavefunction Correction

To go a step further we should use the wavefunctions which are solutions to the Dirac equation. The typical atomic speed is comparable to $Z\alpha = 40/137 = 0.29$, which is comparable to the speed of light ($c = 1$), so it should be no surprise that relativistic effects will be important. For motion in a spherically symmetric field, the solutions to the Dirac equation take the form [7]

$$\psi = \begin{pmatrix}\phi\\ \chi\end{pmatrix} = \begin{pmatrix} f(r)\mathbf{\Omega}_{jlm} \\ (-1)^{\frac{1}{2}(1+l-l')}g(r)\mathbf{\Omega}_{jl'm}\end{pmatrix} \tag{2.26}$$

The quantum numbers j and l' are defined by $j = 1 \pm 1/2$ and $l' = 2j - l$, where j is the total angular momentum. The 2 component spinors $\mathbf{\Omega}_{jlm}$ are the spherical harmonic spinors, defined as

$$\begin{aligned}
\mathbf{\Omega}_{1+\frac{1}{2},l,m} &= \begin{pmatrix}\sqrt{\frac{j+m}{2j}}Y_{l,m-\frac{1}{2}} \\ \sqrt{\frac{j-m}{2j}}Y_{l,m+\frac{1}{2}}\end{pmatrix} \\
\mathbf{\Omega}_{1-\frac{1}{2},l,m} &= \begin{pmatrix}-\sqrt{\frac{j-m+1}{2j+2}}Y_{l,m-\frac{1}{2}} \\ \sqrt{\frac{j+m+1}{2j+2}}Y_{l,m+\frac{1}{2}}\end{pmatrix}
\end{aligned} \tag{2.27}$$

The functions $f(r)$ and $g(r)$ are the large and small radial Dirac functions, defined by

$$\begin{aligned} f,g\ (r) = \frac{\pm(2\lambda)^{3/2}}{\Gamma(2\gamma+1)}\left[\frac{(m\pm E)\Gamma(2\gamma+n_r+1)}{4m(Z\alpha m/\lambda)(Z\alpha m/\lambda-\kappa)n_r!}\right]^{1/2}(2\lambda r)^{\gamma-1}e^{-\lambda r}\times \\ \left[(Z\alpha m/\lambda-\kappa)F(-n_r,2\gamma+1,2\lambda r)\mp n_r F(1-n_r,2\gamma+1,2\lambda r)\right] \end{aligned} \tag{2.28}$$

In the definitions above, the top sign corresponds to the function $f(r)$, and the bottom to $g(r)$. The parameters appearing in the radial Dirac functions are

$$\begin{aligned} \kappa &= \begin{cases} -(j+1/2) = -(l+1), & j = l+1/2 \\ (j+1/2) = l, & j = l-1/2 \end{cases} \\ n_r &= \begin{cases} 0,1,2,..., & \kappa < 0 \\ 1,2,3,..., & \kappa > 0 \end{cases} \\ \gamma &= \sqrt{\kappa^2-(Z\alpha)^2} \\ E &= m\left[1+\frac{(Z\alpha)^2}{[\sqrt{\kappa^2-(Z\alpha)^2}+n_r]^2}\right]^{-1/2} \\ \lambda &= \sqrt{m^2-E^2} \end{aligned} \tag{2.29}$$

The parameter n_r is the principal quantum number, E is the energy of the state, and m is the mass of the orbiting particle. Note that n_r can take the value of 0, so it differs slightly from the non-relativistic principal quantum number. Lastly, the function $F(a,b,z)$ is the confluent hypergeometric function appearing in the non-relativistic Coulomb free energy wavefunction (cf. eq. 2.22). For the ground state wavefunction we have $l=0,\ j=1/2,\ \kappa=-1,\ n_r=0$, and the energy is given by

$$\begin{aligned} E &= m\left[1+\frac{(Z\alpha)^2}{[\sqrt{\kappa^2-(Z\alpha)^2}+n_r]^2}\right]^{-1/2} \\ &= m\left[1+\frac{(Z\alpha)^2}{1-(Z\alpha)^2}\right]^{-1/2} = m\sqrt{1-(Z\alpha)^2} = m\gamma \end{aligned} \tag{2.30}$$

Hence we have $\lambda = Z\alpha m$, so we can write

$$\begin{aligned} f_{1s_{1/2}}(r) &= \frac{(2Z\alpha m)^{3/2}}{\Gamma(2\gamma+1)}\left[\frac{(1+\gamma)\Gamma(2\gamma+1)}{4\times 2}\right]^{1/2}(2Z\alpha mr)^{\gamma-1}e^{-Z\alpha mR_N}\times 2F(0,2\gamma+1,2Z\alpha mr) \\ &= \frac{2(Z\alpha m)^3}{\Gamma^{1/2}(2\gamma+1)}(1+\gamma)^{1/2}(2Z\alpha mr)^{\gamma-1}e^{-Z\alpha mR_N}F(0,2\gamma+1,2Z\alpha mr) \end{aligned} \tag{2.31}$$

It can be shown [7] that the non-relativistic limit of the Dirac functions is given by

$$f(r)\approx R(r), \qquad g(r)\approx \frac{R'(r)}{2m} \tag{2.32}$$

where $R(r)$ is the corresponding non-relativistic wavefunction (solution to the Schrödinger equation). In this limit it is easy to see why $g(r)$ are the small component wavefunctions. As we saw before, the Schrödinger radial wavefunctions can be written as $R_{nl}\propto L^{2l+1}_{n-l-1}(r/a_Z)\exp(-r/a_Z)$, where $L^{2l+1}_{n-l-1}(r/a_Z)$ are the Laguerre polynomials. Importantly, both these functions depend on the ratio r/a_Z, so that a derivative allows us to factor out an additional $a_Z^{-1}=Z\alpha m$. In the approximation above, we have $R'(r)/2m\sim(Z\alpha/2)R(r)$. Given that the non-relativistic limit is found by taking the velocities to be small ($Z\alpha<1$), we can see that this term is much smaller than the large component function $f(r)$. This can also be seen graphically in figure 2.1, where we plot the first two s-wave state solutions of the Dirac and Schrödinger equations.

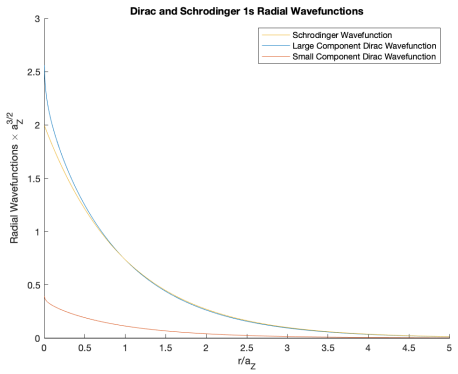

(a) Dirac and Schrödinger 1s radial wavefunctions

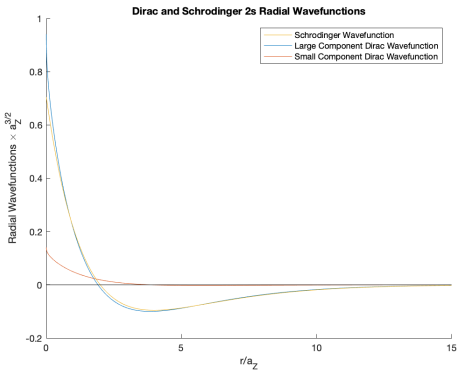

(b) Dirac and Schrödinger 2s radial wavefunctions

Figure 2.1: The first two s-wave states solutions of the Dirac and Schrödinger equations for $Z = 40$. The large component Dirac solutions, $f(r)$, are comparable to the Schrödinger solutions as suggested by Eq. 2.32, but we note that the Dirac solutions are divergent near the origin. We can also see that the small component Dirac solutions, $g(r)$ are smaller than the large component solutions by a factor of 6.5 for the case of $Z = 40$.

We will ignore the contribution from the small component wavefunctions for now, by approximating the radial matrix element integrand as $f_{1s_{1/2}}(r)f_p(r) + g_{1s_{1/2}}(r)g_p(r) \approx f_{1s_{1/2}}(r)f_p(r)$, where f_p, g_p are the positive energy Dirac radial wavefunctions with momentum p. The large component positive energy solution to the Coulomb potential is given in [7] (eq. 36.15), however we must note there is a extra factor of 2 in their expression, see pg 52 of [25].

$$\begin{aligned} f_p(r) &= 2^{1/2}\sqrt{\frac{m+E}{E}}e^{\pi Z\alpha E/2p}\frac{|\Gamma(\gamma+1+iZ\alpha E/p)|}{\Gamma(2\gamma+1)}\frac{(2pr)^\gamma}{r} \times \mathrm{Im}\{e^{i(pr+\xi)}F(\gamma - iZ\alpha E/p, 2\gamma+1, -2ipr)\} \\ &= 2^{1/2}\sqrt{\frac{m+E}{E}}e^{\pi Z\alpha E/2p}\frac{|\Gamma(\gamma+iZ\alpha E/p)|}{\Gamma(2\gamma+1)}\frac{(2pr)^\gamma}{r}|\gamma+iZ\alpha E/p|\mathrm{Im}\{e^{i(pr+\xi)}F(\gamma - iZ\alpha E/p, 2\gamma+1, -2ipr)\} \end{aligned} \tag{2.33}$$

Here $p = \sqrt{E^2 - m^2}$ is the particle's momentum. We also have

$$e^{-2i\xi} = \frac{\gamma - iZ\alpha E/p}{\kappa - iZ\alpha m/p} \tag{2.34}$$

However this isn't the correct normalization we want to use. We would like our expression to reduce to the plane wave limit when the Coulomb potential becomes negligible ($Z\alpha \to 0$) and in the non-relativistic limit (where $E \to m$). We first use the Bessel expansion to write a plane wave as

$$\begin{aligned} e^{-i\mathbf{p}\cdot\mathbf{r}} &= 4\pi\sum_{l=0}^{\infty}\sum_{m=-l}^{l} i^l j_l(pr)Y^*_{lm}(\mathbf{p}/p)Y_{lm}(\mathbf{r}/r) \\ &= \sqrt{4\pi}j_0(pr)Y_{00}(\boldsymbol{r}/r) \end{aligned} \tag{2.35}$$

In the second line we have taken only the $l = 0$ term, and we have kept the angular part of the wavefunction separate in since we want to focus on the radial wavefunction. Thus our wavefunction (which is the $l = 0$ continuous radial wavefunction with momentum p) must reduce to the first Bessel function times a factor of $\sqrt{4\pi}$. The asymptotic expression for f_p ($pr \to \infty$) is

$$f_p(r) \approx \frac{\sqrt{2}}{r}\sqrt{\frac{m+E}{E}}\sin\left(pr + \delta_k + \frac{iZ\alpha E}{p}\ln(2pr)\right) \tag{2.36}$$

where

$$\delta_k = \xi - \arg\Gamma\left(\gamma + 1 + \frac{iZ\alpha E}{p}\right) - \frac{\pi\gamma}{2} \tag{2.37}$$

We note that in the non-relativistic plane wave limit ($Z\alpha \to 0$), $\gamma \to 1$ and $E \to m$, so that

$$
\begin{aligned}
e^{-2i\xi} &= \frac{\gamma - iZ\alpha E/p}{\kappa - iZ\alpha m/p} = -1 \\
&\Rightarrow \xi = \pi/2 \\
&\Rightarrow \delta_k = \pi/2 - \arg\Gamma(2) - \frac{\pi}{2} = 0
\end{aligned}
\tag{2.38}
$$

Thus we see our wavefunction becomes

$$
f_p(r) \to \frac{2}{r}\sin(pr) \tag{2.39}
$$

Thus in order to match this to the Bessel function, $\sqrt{4\pi}j_0(pr) = \sqrt{4\pi}\sin(pr)/(pr)$, we need to multiply the wavefunction by a factor of $\sqrt{4\pi}/2p$. Modifiying the wavefunction by this factor gives

$$
\begin{aligned}
f_p(r) = \sqrt{4\pi}2^{1/2}\sqrt{\frac{m+E}{E}}e^{\pi Z\alpha E/2p}\frac{|\Gamma(\gamma + iZ\alpha E/p)|}{\Gamma(2\gamma+1)}(2pr)^{\gamma-1}|\gamma + iZ\alpha E/p|\times \\
\mathrm{Im}\{e^{i(pr+\xi)}F(\gamma - iZ\alpha E/p, 2\gamma+1, -2ipR_N)\}
\end{aligned}
\tag{2.40}
$$

We note that both the continuum and bound wavefunctions diverge at the origin due to the $r^{\gamma-1}$ term, since $\gamma < 1$. Hence we cannot simply apply our previous formula where we evaluate the wavefunctions at the origin. This divergent behaviour is caused by the divergent Coulomb potential at the origin. Although the electrons are typically far from the nucleus and the pointlike approximation is a good approximation most of the time, this is a case where it fails. A finite size nucleus would alter the potential inside the nucleus, resulting in a finite potential at the origin, eliminating the divergent behaviour of the Dirac wavefunctions. Instead of numerically solving the Dirac equation with a finite size nucleus, a good approximation in this case is to use the Coulomb wavefunctions evaluated at the nuclear radius R_N instead of the origin [19], [26].

The charge radius of ^{90}Zr has been previously determined to be $R_{Nuc} = 4.8791\text{fm}$[27]. In units of $\hbar = c = 1$, this gives $R_N = 2.4726 \times 10^{-8}\text{eV}^{-1} = 0.0126/m_e$, so that we have $2\lambda R_N = 2Z\alpha m_e R_N \approx 0.0058 \ll 1$. We also have $|\gamma + iZ\alpha E/p|\mathrm{Im}\{e^{i(pr+\xi)}F(\gamma - iZ\alpha E/p, 2\gamma+1, -2ipR_N)\} = 0.9787 \approx 1$. This allows us to make the following approximations in the wavefunction

$$
\begin{aligned}
f_{1s_{1/2}}(R_N) &\approx \frac{2(Z\alpha m_e)^(3/2)}{\Gamma^{1/2}(2\gamma+1)}(1+\gamma)^{1/2}(2Z\alpha m_e R_N)^{\gamma-1} \\
f_p(R_N) &\approx \sqrt{4\pi}2^{1/2}\sqrt{\frac{m_e+E}{E}}e^{\pi Z\alpha E/2p}\frac{|\Gamma(\gamma+iZ\alpha E/p)|}{\Gamma(2\gamma+1)}(2pR_N)^{\gamma-1}
\end{aligned}
\tag{2.41}
$$

Returning to our expression for the nuclear strength parameter B, it becomes

$$
|B|^2 = \frac{\pi}{2}\frac{ln(2)}{1.39T_{1/2}p_f E_f}\frac{16\pi^2}{|f_{1s_{1/2}}(R_N)f_p(R_N)|^2} \tag{2.42}
$$

Since we have written the expresison in terms of the radial wavefunctions instead of the full wavefunctions, we get an addition factor of $|Y_{00}^* Y_{00}|^2 = 1/16\pi^2$ (cf. eq. 2.20).

Compared to the non-relativistic Coulomb wavefunctions, the relativistic variants represent a decrease in the strength parameter of

$$
\begin{aligned}
&\frac{|Y_{00}^* Y_{00} f_{1s_{1/2}}(R_N)f_p(R_N)|^2}{|Y_{00}R_{10}(0)\psi_p(0)|^2|} = \\
&= \frac{1}{4\pi}\left[\frac{1-\exp(-2\pi Z\alpha m_e/p_f)}{2\pi Z\alpha m_e/p_f}\right]\left[\frac{1}{4(Z\alpha m_e)^3}\right]\left[\frac{4(Z\alpha m_e)^3}{\Gamma(2\gamma+1)}(1+\gamma)(2Z\alpha m_e R_N)^{2\gamma-2}\right]\times \\
&\quad \left[8\pi\frac{m_e+E}{E}e^{2\pi Z\alpha E/p}\frac{|\Gamma(\gamma+iZ\alpha E/p)|^2}{\Gamma^2(2\gamma+1)}(2pR_N)^{2\gamma-2}\right] \\
&= \frac{1-\exp(-2\pi Z\alpha m_e/p_f)}{2\pi Z\alpha m_e/p_f}\frac{2\pi Z\alpha E/p_f}{1-\exp(-2\pi Z\alpha E/p_f)}\frac{1+\gamma}{\Gamma^3(2\gamma+1)}(2Z\alpha m_e R_N)^{2\gamma-2}\times \\
&\quad 2\frac{m_e+E}{E}(2pR_N)^{2\gamma-2} \\
&= \frac{2(1+\gamma)}{\Gamma^3(2\gamma+1)}\frac{m_e+E}{m_e}\frac{1-\exp(-2\pi Z\alpha m_e/p_f)}{1-\exp(-2\pi Z\alpha E_f/p_f)}(4Z\alpha m_e p R_N^2)^{2\gamma-2} \\
&= 8.2275
\end{aligned}
\tag{2.43}
$$

Again we find a decrease in the strength parameter, with the most recent corrections yielding $|B|^2 = 2.55 \times 10^{-25}$keV. Compared to our original plane wave calculation, the use of accurate wavefunctions decreases the strength parameter by a factor of $1.3 \times 8.2 \approx 10$. Note that the non-relativistic limit corresponds to $\gamma \to 1$ and $E_f \to m_e$.

$$\frac{|Y_{00}^* Y_{00} f_{1s_{1/2}}(R_N) f_p(R_N)|^2}{|Y_{00} R_{10}(0) \psi_p(0)|^2|} \xrightarrow[E_f \to m_e]{\gamma \to 1} \frac{2(1+1)}{\Gamma^3(1+1)} \frac{m_e + m_e}{m_e} \frac{1 - \exp(-2\pi Z\alpha m_e/p_f)}{1 - \exp(-2\pi Z\alpha m_e/p_f)} (4Z\alpha m_e p R_N^2)^{2-2} = 1 \quad (2.44)$$

In this limit, there is no difference between the non-relativistic and relativistic approaches, and the correction factor reduces to 1 as expected.

2.5 Other Corrections

There are other corrections that could be incorporated into this calculation. We could numerically solve the Dirac equation using a reasonable finite size nuclear charge distribution and numerically integrate to find the matrix element. The approximation of using the Coulomb wavefunctions evaluated at the origin underestimates the decay rate by 10-20% [26].

We could also include the contribution of the small component Dirac wavefunction into the E0 matrix element. We found that the small component functions are smaller by a factor of 6.5, so this would only be a 2% contribution to the decay rate.

None of the above approaches considered screening of the electron undergoing a transition. Realistically, both electrons in the 1s states will be screened by each other, and to a certain extent by the other electrons in the atom as well. In the simplest calculation, the E0 transition depends on the cube of the total charge felt by the electron. This is not significantly altered by our more accurate wavefunctions. Hence we naively expect that screening would cause the transition to be modified by a factor of $(Z_{eff}/Z)^3$, where Z_{eff} represents an effective nuclear charge felt by the electron which undergoes the transition. As a naive estimate, we assuming an effective charge of $39 - 5/16$ due to screening from the other s-wave electrons, we find a decrease to the decay rate by approximately 2.5%. The choice of 5/16 is a rough estimate, arising from the Ritz Variational principal for modeling electron screening in Helium [5]. Since B depends inversely on Z^3, this represents an increase to the interaction strength parameter. In actuality however, because the E0 transition depends on the square modulus of the wavefunction at the nucleus, the effect of screening is not significant because there is essentially no screening extremely close to the nucleus [28].

In principle one could also discuss screening of the ejected electron, with positive energy Coulomb wavefunction. If its De Broglie wavelength is large compared to the system of interest, then it will sample the potential at various scales in the atom and could be screened by the orbiting electrons. In our case, given the final momentum is large, $p_f = 1662$keV, then the De Broglie wavelength is $\lambda = 1/p_f = 6 \times 10^{-4}\text{keV}^{-1}$. Converting to SI units via $\hbar c \approx 2 \times 10^5$keV fm gives the de Broglie wavelength on the order of 100fm. Since this roughly 500 times smaller than the Bohr radius, screening effects on the ejected electron are negligible.

We have also not included the possibility for other s-wave states to undergo the E0 transition. Any s-wave state can undergo the E0 transition, although the other s-wave states are more affected by screening and they are less likely to be found on the nucleus ($|\psi_{n00}(0)|^2 \sim n^{-3}$ in the non-relativistic case). Summing over all s-wave state electrons, this would modify the decay rate to be

$$\Gamma_{E0} = \frac{1}{\pi}|B|^2 \sum_{e^- s-wave} p_{f,n} E_{f,n} |\psi_{n00}(0)\psi_f(0)|^2 \quad (2.45)$$

The final momentum and energy depend on the principal quantum number n, although the effect is extremely weak because the nuclear excitation energy (1761keV) is much larger then the electron binding energy (22keV). Since each of these terms is positive, it will also cause a decrease to the strength parameter B. In its lowest energy state, ^{90}Zr's electron configuration is [Kr]$4d^2 5s^2$. If we assume the momentum and energy to be independent of the principal quantum number n and take the non-relativistic wavefunction scaling, we have (ignoring any screening)

$$\begin{aligned} \Gamma_{E0} &= \frac{2}{\pi}|B|^2 p_f E_f |\psi_f(0)|^2 \sum_{n=1}^{5} |\psi_{n00}(0)|^2 \\ &= \frac{2}{\pi}|B|^2 p_f E_f |\psi_{100}(0)\psi_f(0)|^2 \sum_{n=1}^{5} \frac{1}{n^3} \\ &= 1.186 \Gamma_{E0,n=1} \end{aligned} \quad (2.46)$$

where $\Gamma_{E0,n=1}$ denotes the contribution to the decay rate from the ground state electrons, on which we previously focused. We see that the E0 transition is predominantly due to transitions from the ground state electrons,

the other states giving at most a 20% difference. Screening would be more significant for excited s-wave states, causing a decrease to the total decay rate.

Although one could in principle include these extra corrections, using the relativistic wavefunctions as well as the positive energy coulomb solutions provide the largest corrections by far, and give a reasonable estimate for the decay rate.

2.6 Comparison of the Two Methods

As previously discussed, our approach differs from the general approach in the literature. However, we can express their E0 transition results in terms of our parameters. In particular, we want to derive an expression for the nuclear matrix element ρ^2 (eq. 2.6). In our approach ($V_p = B\delta(\mathbf{r})$), we found the decay rate to be

$$\Gamma_{E0} = \frac{2}{\pi}|B|^2 p_f E_f |\psi_i(0)\psi_f(0)|^2 \tag{2.47}$$

where $\psi_{i,f}$ were the initial and final wavefunctions of the electron. If we instead follow the approach of Church and Weneser (cf. eq. 2.10), the decay rate can be written as

$$\Gamma_{E0} = \frac{8\pi\alpha^2}{9} 2 p_f E_f R_N^4 \rho^2 |\psi_i(0)\psi_f(0)|^2 \tag{2.48}$$

Equating and solving for their nuclear strength parameter, we find

$$\rho^2 = \frac{9}{4\pi^2\alpha^2}\frac{|B|^2}{R_N^4} \tag{2.49}$$

Using the relativistic wavefunctions for the parameter B, we find that

$$\rho^2 = 2.92 \times 10^{-3} \tag{2.50}$$

which is comparable to $\rho^2 = 3.46(14) \times 10^{-3}$, the value reported by Kibédi and Spear [21]. The difference, a factor of roughly 1.2, is likely due to the choice of the Dirac wavefunctions evaluated at the nuclear radius, and in ignoring the other corrections discussed above.

Before moving onto our analysis of muonic zirconium, we comment on the applicability, and flaws, of our approach. In the next section, we will be interested in considering the corrections to the energy eigenstates (referred to as the perturbative mixing) due to this potential for a muon orbiting the nucleus. The muon is important, its Bohr radius is comparable to the nuclear radius and therefore it is more susceptible to the finite size nuclear effects. Due to lepton universality, the potential which affects the electron will also affect the muon. Using the electric monopole potential as a perturbation, the modified energy eigenstates for both leptonic systems will be of the form

$$|i\rangle = |i\rangle|0\rangle + \sum_k \frac{\langle 0|\langle i|V_{E0}|k\rangle|1\rangle}{E_i - E_k}|k\rangle|1\rangle \tag{2.51}$$

The ket $|i\rangle$ represents the initial lepton state, and the kets $|k\rangle$ represent the other lepton states which mix perturbatively with the initial state. Following Church and Weneser's analysis, we can write the matrix element as (r_l being the lepton radial coordinate)

$$\langle 0|\langle i|V_{E0}|k\rangle|1\rangle = -\alpha \sum_{p,e} \int d\tau_{Nuc} \int_0^{r_p} dr_l \phi_0^* R_k^*(r_l)\left(\frac{r_l^2}{r_p} - r_l\right)\phi_1 R_i(r_l) \tag{2.52}$$

In the case of the electron, we were able to perform the integral over the electron radial coordinate by noting that the wavefunctions did not change appreciably for $r_{el} \in [0, r_p]$. However, for the case of the muon, this will not be true, since the Bohr radius is comparable to the nuclear radius. Performing the integral will not lead to the simple r_p^2 behaviour discovered for the electron transition, and the nuclear matrix element will be different than the parameter ρ which we found above. As was noted earlier, zirconium's atomic number is too large to find the proton wavefunctions, so we cannot calculate the size of this mixing.

Using our approach, this perturbation can be calculated. As discussed earlier, the parameter B contains information about the matrix element between the nuclear states. Consider the operator $\mathcal{A}$, responsible for the nuclear part of the E0 transition, $\langle 0|\mathcal{A}|1\rangle$. In our approach, this matrix element is implicitly present in the parameter B. By lepton universality, the same interaction occurs between the nucleus and the electron as does between the nucleus and the muon. Hence the matrix element in the perturbative mixing behaves as

$$\langle 0|\langle i|V_{E0}|k\rangle|1\rangle = \langle i|B\delta^3(\mathbf{r})|k\rangle \tag{2.53}$$

which can be calculated. In the future when we discuss mixing in leptonic states, we will often write the perturbation matrix element as $\langle i|B\delta^3(\mathbf{r})|k\rangle$, where the nuclear matrix element is understood as sitting within B. The drawback of this approach is a potential lack of accuracy. As seen above, the nuclear matrix elements which appear when considering muonic states may not have the same form as those between the electron states. We make the implicit assumption that they do have the same form. We have mentioned several times that the finite size of the nucleus is an important consideration when discussing muonic zirconium states. In the next chapter, we will generalize our pointlike delta potential to incorporate finite size effects, and then apply it to study the muonic states.

Chapter 3

Populating the Excited Nuclear State

From hereon in, when we discuss an atom, it is assumed that we are discussing muonic zirconium unless otherwise specified. We now want to study how the muonic $|100\rangle|1\rangle$ state can be populated. That is, how can we prepare the muonic atom where the muon sits in the $1s$ state, but the nucleus is in the first excited state. Muons are typically captured in high n and high l orbitals, which subsequently decay via electric dipole transitions to lower atomic energy states. The electric dipole transition is the fastest transition which can occur (as long as selection rules allow it) so it will be the most common decay channel. Furthermore, electric dipole transitions occur between states differing by one unit of angular momentum. Since we want our muon to end up in the $1s$ state, this suggests our initial state should be an np state. Because the muons are typically captured in high n and high l orbits, and dipole transitions dominate, this suggests that np states with higher values of n are very unlikely to be populated. One might ask why wouldn't it be possible to access the spectrum of excited nuclear states from each one of the decays in the muonic cascade. That is, why not study a $|430\rangle|0\rangle \to |320\rangle|1\rangle$ transition, for example. As we we will soon see, the opportunity for a transition arises when one considers perturbative mixing of the muonic and nuclear states. The potential responsible is the one we have studied, proportional to a delta function. This implies that only mixing between s-wave states can occur, because all other states are zero at the origin. We shall study this effect when we consider the finite size nucleus, and show that the transition is still dominated by s-wave mixings. Hence we focus on populating the $|100\rangle|1\rangle$ state when the initial muonic state is either $2p$ or a $3p$. We will study the branching ratios from the initial states, that is, given we have a muon in the $|210\rangle|0\rangle$ state, what is the probability it transition to the $|100\rangle|1\rangle$ rather than a transition to a state containing the nuclear ground state.

3.1 The Pointlike Nuclear Approximation

Now that we have a model for the strength of the perturbation $V = B\delta(\mathbf{r})$ and we know the strength parameter B, we can calculate the effect of this perturbation on the muonic atom. The transition $|21m\rangle|0\rangle \to |100\rangle|1\rangle$ cannot occur without some mechanism to connect the otherwise orthogonal nuclear states. However, the perturbation will cause some slight mixing from the $|100\rangle|1\rangle$ state to the other muonic s-wave and nuclear ground states ($|n00\rangle|0\rangle$). It is these states to which the $|21m\rangle|0\rangle$ can decay to. Other orbitals (e.g. p, d, f etc.) cannot mix under this perturbation as they vanish where the perturbation is non-zero (at the origin) as we discussed above. Thus we are interested in mixing with the ns state for $n \geq 2$ and so we define the final perturbed wavefunction as ψ_f, given by

$$\begin{aligned} \psi_f &\equiv |100\rangle|1\rangle + \sum_{n=1}^{\infty} \frac{\langle 100|V|n00\rangle}{(E_1 + E_{Nuc}) - E_n} |n00\rangle|0\rangle \\ &\equiv |100\rangle|1\rangle + \sum_{n=1}^{\infty} \epsilon_{ns} |n00\rangle|0\rangle \end{aligned} \tag{3.1}$$

where we have defined ϵ_{ns} as the perturbative mixing parameters

$$\epsilon_{ns} \equiv \frac{\langle 100|V|n00\rangle}{(E_1 + E_{Nuc}) - E_n} \tag{3.2}$$

Although this is essentially the same framework we used for the E0 transition above, it is important to remember that we are now working with a muon oribiting the nucleus. We will soon see that this has important effects on our treatment.

For a muonic hydrogren-like atom, we have

$$E_1 + E_{Nuc} - E_2 = E_{Nuc} - \left(\frac{1}{2} - \frac{1}{2n^2}\right) m_\mu (Z\alpha)^2 \tag{3.3}$$

and

$$\begin{aligned}
\langle 100|V|n00\rangle &= \langle \psi_{1s,\mu}|B\delta^3(\mathbf{r})|\psi_{ns,\mu}\rangle \\
&= B\psi^*_{1s,\mu}(r)\psi_{ns,\mu}(r)|_{r=0} \\
&= B|Y_{00}|^2 R^*_{10}(r)R_{n0}(r)|_{r=0} \\
&= \frac{B}{4\pi} 2a_{Z,\mu}^{-3/2} 2(na_{Z,\mu})^{-3/2} \\
&= B\frac{(Z\alpha m_\mu)^3}{n^{3/2}\pi}
\end{aligned} \tag{3.4}$$

Hence the mixing term ϵ_{ns} is given by

$$\begin{aligned}
\epsilon_{ns} &= \frac{\langle 100|V|n00\rangle}{E_1 + E_{Nuc} - E_n} \\
&= \frac{B}{n^{3/2}\pi} \frac{2(Z\alpha m_\mu)^3}{(2E_{Nuc} - (1-1/n^2)m_\mu(Z\alpha)^2)}
\end{aligned} \tag{3.5}$$

We see the mixing is suppressed by $n^{3/2}$, so it decreases for larger n. However there is a possibility of a large mixing if the denominator is close to zero or in other words if the energies of the states are close. Recall the nuclear energy is 1761keV, so the energy of the $|100\rangle|1\rangle$ state is $E_1 + E_{Nuc} = -2740$keV. The $|200\rangle|0\rangle$ state has energy $E_2 = -1125$keV, so the energy differences appearing in the denominator in ϵ_{1s} and ϵ_{2s} are somewhat similar. Neither of these states are significantly affected by the $n^{3/2}$ suppression, so we expect similar contributions from the $|n00\rangle|0\rangle, n = 1, 2$ states. In comparison, the other s-wave states ($|n00\rangle|0\rangle$, $n \geq 3$) have energies further away from the original state, and are more significantly affected by the $n^{3/2}$ suppression. It follows that the most significant contribution come from the first two terms, and so we ignore contributions from $n \geq 3$ for now.

If we want to compute the branching ratio for the decay of the $|210\rangle|0\rangle$ state into the ψ_f state, then we have

$$\begin{aligned}
Br &= \frac{\Gamma_{|210\rangle|0\rangle \to \psi_f}}{\Gamma_T} \\
&\approx \frac{\Gamma_{|210\rangle|0\rangle \to |100\rangle|1\rangle}}{\Gamma_{|210\rangle|0\rangle \to |100\rangle|0\rangle}}
\end{aligned} \tag{3.6}$$

where we have approximated the total branching ratio to be the muonic $2p \to 1s$ transition, mainly mediated by the electric dipole transition. We first investigate the decay $|210\rangle|0\rangle \to \psi_f$. With the above argument in mind, we take our perturbed final wavefunction to be

$$\psi_f = |100\rangle|1\rangle + \epsilon_{1s}|100\rangle|0\rangle + \epsilon_{2s}|200\rangle|0\rangle \tag{3.7}$$

The dominant term in ψ_f is the unperturbed term $|100\rangle|1\rangle$, but because this nuclear state is orthogonal to the nuclear state in the initial wavefunction, the matrix element connects the initial state with the $|n00\rangle|0\rangle$ states appearing in the perturbed final wavefunction. If $\mathcal{A}$ is a purely leptonic operator which mediates the atomic transition, (i.,e. $\mathcal{A}$ does not explicitly contain any nuclear operators), we have

$$\begin{aligned}
\langle i|\mathcal{A}|f\rangle &= \langle 0|\langle 210|\mathcal{A}\Big(|100\rangle|1\rangle + \epsilon_{1s}|100\rangle|0\rangle + \epsilon_{2s}|200\rangle|0\rangle\Big) \\
&= \langle 210|\mathcal{A}|100\rangle\cancelto{0}{\langle 0|1\rangle} + \epsilon_{1s}\langle 210|\mathcal{A}|100\rangle + \epsilon_{2s}\langle 210|\mathcal{A}|200\rangle
\end{aligned} \tag{3.8}$$

The most significant contribution to the decay will thus be mediated by a transition from the 2p state to s-wave states. The strongest transition of this form is the E1 transition, with decay rate

$$\Gamma_{E1} = \frac{4}{3}\alpha\omega^3 |\langle \mathbf{r}_{fi}\rangle|^2 \tag{3.9}$$

Thus taking the radial position operator $\mathbf{r}$ as our operator $\mathcal{A}$, we have

$$\langle i|\mathbf{r}|f\rangle = \epsilon_{1s}\langle 210|\mathbf{r}|100\rangle + \epsilon_{2s}\langle 210|\mathbf{r}|200\rangle \tag{3.10}$$

The $2p_\mu \to 1s_\mu$ decay is also an E1 transition, so the ratio of the two depends only on the cube of the photon frequencies (or transition energies) as well as the matrix element $\langle i|\mathbf{r}|f\rangle$. As the 2s state and the 1s have no angular dependence, the angular integral in both decays is identical, so we have

$$\begin{aligned} Br &= \frac{E_\mu^3|\epsilon_{1s}\langle R_{21}|r|R_{10}\rangle + \epsilon_{2s}\langle R_{21}|r|R_{20}\rangle|^2}{E_{2p\to 1s}^3|\langle R_{21}|r|R_{10}\rangle|^2} \\ &= \frac{E_\mu^3}{E_{2p\to 1s}^3}\left|\epsilon_{1s} + \epsilon_{2s}\frac{\langle R_{21}|r|R_{20}\rangle}{\langle R_{21}|r|R_{10}\rangle}\right|^2 \end{aligned} \tag{3.11}$$

where we have defined $E_\mu \equiv E_2 - (E_1 + E_{Nuc})$ as the muonic transition energy in the $|210\rangle|0\rangle \to \psi_f$ decay. The transition energies are found to be

$$\begin{aligned} E_\mu &= 1615\text{keV} \\ E_{2p\to 1s} &= 3376\text{keV} \end{aligned} \tag{3.12}$$

The radial matrix elements are found to be [29]

$$\begin{aligned} \langle R_{21}|r|R_{10}\rangle &= \frac{2^{15/2}}{3^{9/2}}a_{Z,\mu} \\ \langle R_{21}|r|R_{20}\rangle &= -2(3)^{3/2}a_{Z,\mu} \\ \frac{\langle R_{21}|r|R_{20}\rangle}{\langle R_{21}|r|R_{10}\rangle} &= -\frac{3^6}{2^{15/2}} \end{aligned} \tag{3.13}$$

With reference to the branching ratio expression above, to determine how the the mixing with the 1s and 2s states compete, we must compare ϵ_{1s} and $3^6/2^{15/2}\epsilon_{2s}$. We will also include the n=3 mixing term as we will need it soon to investigate the branching ratio from the 3p state. Using eq. 3.5, we find that

$$\begin{aligned} \epsilon_{1s} &= \frac{B}{\pi}\frac{(Z\alpha m_\mu)^3}{E_{Nuc}} = 2.67\times 10^{-3} \\ \epsilon_{2s} &= \frac{B}{2^{3/2}\pi}\frac{2(Z\alpha m_\mu)^3}{(2E_{Nuc} - (1-1/4)m_\mu(Z\alpha)^2)} = -1.03\times 10^{-3} \\ \epsilon_{3s} &= \frac{B}{3^{3/2}\pi}\frac{2(Z\alpha m_\mu)^3}{(2E_{Nuc} - (1-1/9)m_\mu(Z\alpha)^2)} = -4.05\times 10^{-4} \end{aligned} \tag{3.14}$$

So that the contribution from the 1s state is $\epsilon_{1s} = 2.67\times 10^{-3}$ and the contribution from the 2s state is $-\epsilon_{2s}(3^6/2^{15/2}) = 4.16\times 10^{-3}$. Including the radial matrix element ratio, the next contribution (the $n = 3$ term) can be calculated to be 2.95×10^{-4}, which justifies ignoring the other s-wave mixings. The branching ratio is found to be

$$Br = 5.12\times 10^{-6} \tag{3.15}$$

Before moving into a more accurate approach, note that we have included perturbative mixings for the final state, but not for the initial state. Since the initial state is a p-wave state, it vanishes at the origin. Hence any effect of the delta perturbation will vanish, so in this approach the initial state remains unchanged after included effects of the perturbation. When we move forward to a more accurate approach involving a finite nuclear size perturbation, mixings with the initial state will be non-zero, and we shall investigate their significance.

As previously discussed, we could also investigate the branching ratio from the 3p state, following the same approach. We must make a slight change, reflecting that the total decay rate is no longer approximated by the $3p \to 1s$ decay, but the combination of the $3p \to 1s$ and $3p \to 2s$ decays. Again the dominant transition is the E1 transition, which leads to a branching ratio

$$Br_{3p} = \frac{(E_3 - (E_1 + E_{Nuc}))^3|\epsilon_{1s}\langle R_{31}|r|R_{10}\rangle + \epsilon_{2s}\langle R_{31}|r|R_{20}\rangle + \epsilon_{3s}\langle R_{31}|r|R_{30}\rangle|^2}{E_{3p\to 1s}^3|\langle R_{31}|r|R_{10}\rangle|^2 + E_{3p\to 2s}^3|\langle R_{31}|r|R_{20}\rangle|^2} \tag{3.16}$$

The transition energies as well as the radial matrix elements are changed to reflect the initial state being the 3p state, but the mixing parameters ϵ_{ns} are left unchanged since they only depend on the s-wave states and the perturbation. We must include terms up to the 3s mixings, because there is significant overlap in 3s and 3p states in the matrix element. The 4s term mixing is roughly an order of magnitude smaller than the 3s term, so we ignore it. The transition energies are found to be

$$\begin{aligned} E_3 - (E_1 + E_{Nuc}) &= 2240\text{keV} \\ E_{3p\to 1s} &= 4001\text{keV} \\ E_{3p\to 2s} &= 625\text{keV} \end{aligned} \tag{3.17}$$

The radial matrix elements are

$$\begin{aligned}\langle R_{31}|r|R_{10}\rangle &= \frac{3^{7/2}}{2^{13/2}}a_{Z,\mu}\\ \langle R_{31}|r|R_{20}\rangle &= \frac{2^{10}3^{7/2}}{5^6}a_{Z,\mu}\\ \langle R_{31}|r|R_{30}\rangle &= -3^2 2^{1/2}a_{Z,\mu}\end{aligned} \tag{3.18}$$

Hence the branching ratio from the 3p state is found to be

$$Br_{3p} = 6.61\times 10^{-6} \tag{3.19}$$

In a similar manner to the E0 transition, we will now make the branching ratio more accurate by including more realistic effects. In the E0 transition, we used more accurate wavefucntions by including free energy Coulomb waves and relativistic effects. For the muonic states, it turns out that the effects of the finite nuclear size are the most important correction. The Hydrogen point-like wavefunctions are convenient to work with due to their simple nature, but they fail to be a good approximation in this case.

Given that the proton (i.e. Hydrogen nucleus) has a finite size [30] [31], why are these effects not important for an electron oribiting Hydrogen? The answer lies in the characteristic orbital scale of the two scenarios. We have already seen that the electron in hydrogen has a Bohr radius 5 orders of magnitude smaller than the proton radius, where as muonic zirconium's Bohr radius is comparable to the nuclear radius.

In a perturbative approach for the point-like nucleus, the result of including the finite nuclear size as a perturbation leads to an energy shift for the s wave states [7]

$$\begin{aligned}\Delta E_{\text{Finite Size}} &= \frac{2\pi}{3}Z\alpha r_c^2|\psi_{n00}(0)|\\ &= \frac{2\pi}{3}\frac{Z^4\alpha^4}{n^3}r_c^2\frac{m^3}{\hbar^3}\\ &= \frac{2\pi}{3}\frac{Z^4\alpha^4}{n^3}\left(\frac{r_c}{1\text{fm}}\right)^2\left(\frac{1\text{fm }m}{197.3\text{MeV fm}}\right)^2\left(\frac{m}{\text{eV}}\right)\text{eV}\end{aligned} \tag{3.20}$$

To understand the size of this effect, an empirical estimate gives the nuclear radius as $r_c \approx 1.3\text{fm}A^{1/3}$, where A is the atomic number. For hydrogen this yields $r_c = 1.3$fm, and for zirconium this gives $r_c = 4.5$fm. Although the proton is know to have a radius closer to 0.83fm, the order of magnitude will be the same. For hydrogen, the energy shift of the ground state is

$$\begin{aligned}\Delta E_{\text{Finite Size, Hydrogen}} &= \frac{2\pi}{3}\frac{1}{137^4}\left(\frac{r_c}{1\text{fm}}\right)^2\left(\frac{1\text{fm }0.511\text{MeV}}{197.3\text{MeV fm}}\right)^2\left(\frac{511000\text{eV}}{\text{eV}}\right)\text{eV}\\ &\approx 2\times 10^{-8}\left(\frac{r_c}{1\text{fm}}\right)^2\text{eV}\\ &\approx 10^{-8}\text{ev}\\ E_{b,\text{Hydrogen}} &= 13.6\text{eV}\end{aligned} \tag{3.21}$$

For electronic zirconium, it is

$$\begin{aligned}\Delta E_{\text{Finite Size},^{90}Zr,e} &= \frac{2\pi}{3}\frac{40^4}{137^4}\left(\frac{r_c}{1\text{fm}}\right)^2\left(\frac{1\text{fm }0.511\text{MeV}}{197.3\text{MeV fm}}\right)^2\left(\frac{511000\text{eV}}{\text{eV}}\right)\text{eV}\\ &\approx 0.0512\left(\frac{r_c}{1\text{fm}}\right)^2\text{eV}\\ &= 1.04\text{eV}\\ E_{b,^{90}Zr,e} &= 21800\text{eV}\end{aligned} \tag{3.22}$$

and for the ground state of muonic zirconium, we find

$$\begin{aligned}\Delta E_{\text{Finite Size},^{90}Zr,\mu} &= \frac{2\pi}{3}\frac{40^4}{137^4}\left(\frac{r_c}{1\text{fm}}\right)^2\left(\frac{1\text{fm }105.5\text{MeV}}{197.3\text{MeV fm}}\right)^2\left(\frac{1.055\times 10^8\text{eV}}{\text{eV}}\right)\text{eV}\\ &\approx 5\times 10^5\left(\frac{r_c}{1\text{fm}}\right)^2\text{eV}\\ &= 15.6\text{MeV}\\ E_{b,^{90}Zr,\mu} &= 4.5\text{MeV}\end{aligned} \tag{3.23}$$

To determine which scenarios can be treated perturbatively, we need to compare these energy shifts to the binding energies $E_b = 0.5(Z\alpha)^2 m$, listed in the last line of each calculation. Wee see the finite size is relatively unimportant for hydrogen (as expected) and even electronic zirconium. However, the energy shift of muonic zirconium is larger than the binding energy implying the finite size of the nucleus can not be treated in a perturbative manner for muonic zirconium. In the next section, we will see include the finite size of the nucleus by numerically solving the Schrödinger equation.

3.2 The Finite Nuclear Charge Distribution

We must solve the Schrodiner equation with a potential that takes into account the finite size of the nucleus. This is done by modifying the nuclear charge distribution from a delta function (point-like), to a smooth distribution extending radially outward with some characteristic size before it quickly falls off. Typical choices involve a uniform charge distribution, modeled by a Heaviside function, or the Fermi distribution. We will use the Fermi distribution [32], where the nuclear charge distribution $\rho(r)$ is modeled by

$$\rho(r) = \frac{\rho_0}{1 + \exp(\frac{r-c}{a})} \tag{3.24}$$

The parameter c is the half-density radius, where the charge distribution drops to one half its value at the origin. The diffuseness parameter, a, is a measure of how quickly the charge distribution falls off near the nuclear radius. It is related to the skin thickness, t, which measures how quickly the charge distribution drops from 90% to 10% of its maximum value by $t = (4 \ln 3)a$. These parameters have been previously determined to be [27] (and references within)

$$\begin{aligned} c &= 4.8791\text{fm} \\ a &= 0.5367\text{fm} \end{aligned} \tag{3.25}$$

The half-density radius was determined using muonic transition energies, whereas the diffuseness parameter was determined using elastic electron scattering data. They also briefly discuss some of the differences between charge radius definitions in the context of muonic atoms. The last parameter in the Fermi distribution, ρ_0, is a normalization constant that ensures

$$\int d^3r \rho(r) = Ze \tag{3.26}$$

Using the parameters above, the charge distribution has been plotted in blue, in figure 3.1, taking $\rho_0 = 1$ for simplicity. The red curve represents a charge distribution with a diffuseness parameter a twice as large, creating a longer charge fall-off region. The yellow curve features a diffuseness parameter half as large as Zirconium, implying a quicker fall-off region. The green curve represents a sphere with a uniform charge density.

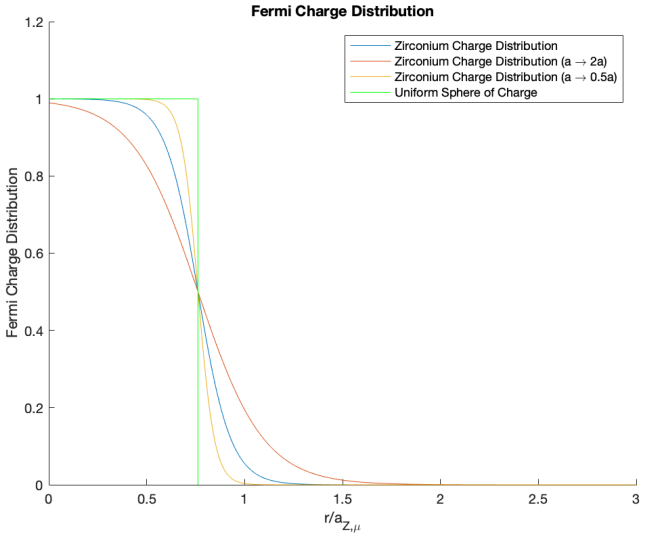

Figure 3.1: The Fermi charge distribution for the nucleus of Zirconium. The diffuseness parameter of red and yellow curves has been doubled and halved, for comparison. The normalization of the distribution has been taken to be $\rho = 1$ for simplicity, since it does not affect the curve shape.

As we pass from the red to blue to yellow curve, we can see the charge distribution becomes more similar to the spherical uniform charge distribution in green, whose parametrization is given by

$$\rho(r) = \begin{cases} \rho_0, & r \ll c \\ 0, & r \gg c \end{cases} \tag{3.27}$$

where c represents the nuclear charge radius. Indeed, if we take the limit as the diffuseness parameter becomes small $a \to 0$, then we have

$$\lim_{a\to 0} \exp\left(\frac{r-c}{a}\right) = \begin{cases} 0, & r \ll c \\ \infty, & r \gg c \end{cases} \tag{3.28}$$

Hence the charge distribution vanishes outside the charge radius, and is constant in the interior, that is

$$\lim_{a\to 0} \frac{\rho_0}{1+\exp(\frac{r-c}{a})} = \begin{cases} \rho_0, & r \ll c \\ 0, & r \gg c \end{cases} \tag{3.29}$$

As the E0 transition is due to EM interaction, it can only happen due to an interaction between the electron and a proton. Hence we want to model the proton distribution in the nucleus. The protons are the only charged nucleons, so their distribution must be identical the charge distribution. We thus model the average proton density by

$$N_{Nuc}(r) = \frac{b}{1+\exp(\frac{r-c}{a})} \tag{3.30}$$

where b is a normalization parameter which ensures

$$\int d^3 r N_{Nuc}(r) = 1 \tag{3.31}$$

Before using this charge distribution to solve the Schrödinger equation and solve the wavefunctions and energies, we should investigate if this new interaction affects the E0 transition. As before, we model the interaction potential being proportional to the electron being found on the nucleus. Therefore our perturbation is proportional to the charge distribution

$$V(r) = BN_{Nuc}(r) \tag{3.32}$$

Here B is a constant that represents the strength of the interaction. The usefulness of the normalization of $N_{Nuc}(r)$ in Eq. 3.31 is that the strength parameter B retains the same formula as it did in the pointlike nuclear case. To see this, note that we have the same equation as before for the decay rate

$$d\Gamma = (2)2\pi |\langle f|V|i\rangle|^2 \frac{d^3p}{(2\pi)^3} \delta(E - E_{Nuc} - E_i) \tag{3.33}$$

Since the potential is no longer a delta function, it seems like we must actually perform an integral in the matrix element. Since we can treat the finite size pertubatively for electronic zirconium, the initial and final state wavefunctions correspond to the pointlike nuclear wavefunctions. We first look at the matrix element

$$\langle f|V|i\rangle = \int d^3 r \psi_f(r) B N_{Nuc}(r) \psi_i(r) \tag{3.34}$$

Note that the Fermi distribution (and hence $N_{Nuc}(r)$) is only significant for $r \lesssim 2c \approx 10$fm. Because we are still considering a decay involving an electron, the 1s wavefunction has a characteristic scale of the Bohr radius, and is essentially constant in the region where the nuclear distribution is non-zero. A similar analysis applies to the final state particle, with momentum $p_f = 1662$keV. Taylor expanding the wavefunction, the positive energy electron's wavefunction does not change significantly given that $pr \ll 1$. Converting using $\hbar c \approx 2 \times 10^5$keV fm, distances smaller than 10fm correspond to distances smaller than $5 \times 10^{-5}\text{keV}^{-1}$. Hence when the integrand is significant (i.e. when $N_{Nuc}(r)$ is significant), we have $pr \leq (1662\text{keV})(5 \times 10^{-5}\text{keV}^{-1}) = 0.08 \ll 1$. Thus we may approximate both the electron wavefunctions by their value at the origin, which is essentially the same approach as using the delta function. The differences between the two potentials will be much more significant when using the muon wavefunctions, whose characteristic scale is the same order of magnitude as the nuclear radius.

As mentioned before, our normalization of the nuclear distribution yields the same expression for the interaction strength parameter

$$|B|^2 = \frac{\pi}{2} \frac{ln(2)}{1.39 T_{1/2} p_f E_f} \frac{16\pi^2}{|f_{1s_{1/2}}(R_N) f_p(R_N)|^2} \tag{3.35}$$

3.3 Numerical Solutions

3.3.1 The Numerov Method

Unlike the pointlike nucleus discussed earlier, there are no closed form solutions for the potential or the radial wavefunctions found by using the Fermi charge distribution. The potential however, does have a series expansion, with different expressions inside and outside the charge radius [33] although we will proceed via numerical integration. We will discretize our radial coordinate and employ numerical integration techniques to find our wavefunctions. We first pause to discuss the Numerov method [34] (following the presentation in [35]), which we will apply to the Schrödinger equation in order to find the radial wavefunctions.

As we discussed in the introduction, the radial part of the Schrödinger equation can be written in the form

$$\frac{d^2u(r)}{dr^2} + \frac{2m}{\hbar^2}\left(E - V(r) - \frac{\hbar^2}{2m}\frac{l(l+1)}{r^2}\right)u(r) = 0 \tag{3.36}$$

where $u(r) = rR(r)$. If we define

$$k^2(r) \equiv \frac{2m}{\hbar^2}\left(E - V(r) - \frac{\hbar^2}{2m}\frac{l(l+1)}{r^2}\right) \tag{3.37}$$

then Schrödinger's equation becomes

$$\frac{d^2u(r)}{dr^2} + k^2(r)u(r) = 0 \tag{3.38}$$

All we have done so far is simplified the equation by redefining parameters. We will now take advantage of its form, in particular it is linear in the function $u(r)$ and has no term involving the first derivative, $du(r)/dr$.

Now consider performing a Talyor expansion of the function $u(r)$ about the point $r+h$ and $r-h$, where h is some small parameter. Denoting the n^{th} derivative of the function $u(r)$ by $u^{(n)}(r)$, we have

$$\begin{aligned} u(r+h) &= u(r) + hu^{(1)}(r) + \frac{h^2}{2}u^{(2)}(r) + \frac{h^3}{6}u^{(3)}(r) + \frac{h^4}{24}u^{(4)}(r) + \mathcal{O}(h^5) \\ u(r-h) &= u(r) - hu^{(1)}(r) + \frac{h^2}{2}u^{(2)}(r) - \frac{h^3}{6}u^{(3)}(r) + \frac{h^4}{24}u^{(4)}(r) + \mathcal{O}(h^5) \end{aligned} \tag{3.39}$$

If we add these two terms together, the odd terms cancel, yielding

$$u(r+h) + u(r-h) = 2u(r) + h^2u^{(2)}(r) + \frac{h^4}{12}u^{(4)}(r) + \mathcal{O}(h^6) \tag{3.40}$$

Rearranging this gives an expression for the second derivative

$$\begin{aligned} u^{(2)}(r) &= \frac{u(r+h) + u(r-h) - 2u(r)}{h^2} - \frac{h^2}{2}u^{(4)}(r) + \mathcal{O}(h^4) \\ 0 &= \frac{u(r+h) + u(r-h) - 2u(r)}{h^2} - \left(u^{(2)}(r) + \frac{h^2}{2}u^{(4)}(r)\right) + \mathcal{O}(h^4) \end{aligned} \tag{3.41}$$

In the second line, we have reordered the expression, as we will soon make a substitution in order to eliminate the term in parenthesis. To do this, we apply the differential operator $1 + (h^2/12)d^2/dr^2$ to eq. 3.38, yielding

$$\begin{aligned} u^{(2)}(r) + \frac{h^2}{12}u^{(4)}(r) + k^2(r)u(r) + \frac{h^2}{12}\frac{d^2}{dr^2}[k^2(r)u(r)] &= 0 \\ \Rightarrow u^{(2)}(r) + \frac{h^2}{12}u^{(4)}(r) &= -k^2(r)u(r) - \frac{h^2}{12}\frac{d^2}{dr^2}[k^2(r)u(r)] \end{aligned} \tag{3.42}$$

If we now substitute eq. 3.42 into eq. 3.41, we find

$$\begin{aligned} 0 &= \frac{u(r+h) + u(r-h) - 2u(r)}{h^2} - \left(-k^2(r)u(r) - \frac{h^2}{12}\frac{d^2}{dr^2}[k^2(r)u(r)]\right) + \mathcal{O}(h^4) \\ \Rightarrow 0 &= u(r+h) + u(r-h) - 2u(r) + h^2k^2(r)u(r) + \frac{h^4}{12}\frac{d^2}{dr^2}[k^2(r)u(r)] + \mathcal{O}(h^6) \end{aligned} \tag{3.43}$$

We use an elementary difference formula to evaluate the last term

$$\frac{d^2}{dr^2}[k^2(r)u(r)] \approx \frac{k^2(r+h)u(r+h) + k^2(r-h)u(r-h) - 2k^2(r)u(r)}{h^2} \tag{3.44}$$

This approximation has an error $\mathcal{O}(h^2)$, but it is multipled by a factor of h^4, preserving the $\mathcal{O}(h^6)$ accuracy. Making this substitution into eq. 3.43, we find

$$\begin{aligned} 0 &= u(r+h) + u(r-h) - 2u(r) + h^2k^2(r)u(r) + \\ &+ \frac{h^4}{12}\frac{k^2(r+h)u(r+h) + k^2(r-h)u(r-h) - 2k^2(r)u(r)}{h^2} + \mathcal{O}(h^6) \end{aligned} \tag{3.45}$$

We will be interested in solving for the function $u(r+h)$, as this will allow us to work outward from the origin recursively, given that $u(0)$ and $u(h)$ are known. Gathering like terms, we have

$$\begin{aligned} -u(r+h)\Big(1 + \frac{h^2}{12}k^2(r+h)\Big) &= u(r)\Big(-2 - \frac{2h^2k^2(r)}{12} + h^2k^2(r)\Big) + u(r-h)\Big(1 + \frac{h^2}{12}k^2(r-h)\Big) \\ \Rightarrow u(r+h) &= \frac{2(1 - \frac{5}{12}h^2k^2(r))u(r) - (1 + \frac{1}{12}h^2k^2(r-h))u(r-h)}{1 + \frac{1}{12}h^2k^2(x+h)} + \mathcal{O}(h^6) \end{aligned} \tag{3.46}$$

To clean up notation, let the n-th step be $r_n \equiv nh$, where we start from the origin, $r = 0$, let $k_n \equiv k(r_n)$, and $u_n \equiv u(r_n)$. This allows us to write the recursive solution

$$u_{n+1} = \frac{2(1 - \frac{5}{12}h^2k_n^2)u_n - (1 + \frac{1}{12}h^2k_{n-1}^2)u_{n-1}}{1 + \frac{1}{12}h^2k_{n+1}^2} \tag{3.47}$$

with an error of $\mathcal{O}(h^6)$. If we know suitable boundary condditions for the Radial wavefunctions around the origin, we can use this equation to find the Radial wavefunctions, since all the parameters on the right hand side are known. Specifically we need the boundary conditions $u(r = 0) = u_0$ and $u(r = h) = u_1$. It is no surprise that we require two boundary conditions, since the Schrödinger equation is a second order differential equation.

Note that the 1-dimensional Numerov method takes a very similar form:

$$\psi_{n+1} = \frac{2(1 - \frac{5}{12}h^2k_n^2)\psi_n - (1 + \frac{1}{12}h^2k_{n-1}^2)\psi_{n-1}}{1 + \frac{1}{12}h^2k_{n+1}^2} \tag{3.48}$$

however care must be taken to distinguish the two cases. In the 1-dimensional case, $\psi_n \equiv \psi(x_n)$ is the actual wavefunction, whereas in the 3-dimensional case, we are solving for the re-scaled radial wavefunction $u(r) = rR(r)$

3.3.2 Boundary Conditions for the Wavefunctions

Before moving onto to the numerical calculation of the finite size potential, we need to address the boundary conditions of the wavefunction, u_0 and u_1. Here we follow the presentation of Landau and Lifshitz [6], assuming that the potential has the property that it is not too singular, in particular it satisfies $V(r)r^2 \xrightarrow{r\to 0} 0$. This is valid for the Coulomb potential, and will certainly be valid for the finite-size nuclear potential. Taking the small r limit of the radial Schrödinger equation, we find

$$\frac{d}{dr}\Big(r^2\frac{dR}{dr}\Big) - \frac{2mr^2}{\hbar^2}\Big(V(r) - E\Big)R - l(l+1)R \xrightarrow{r\to 0} \frac{d}{dr}\Big(r^2\frac{dR}{dr}\Big) - -l(l+1)R = 0 \tag{3.49}$$

If we want the behaviour of the radial solutions near the origin, we can perform a Talyor expansion, and retain only the first term, that is $R(r) \approx Cr^s$, where C is some normalization constant. Making this substitution above yields

$$\begin{aligned} 0 &= \frac{d}{dr}\Big(r^2\frac{dR}{dr}\Big) - -l(l+1)R \\ &= C\frac{d}{dr}\Big(r^2\frac{dr^s}{dr}\Big) - -Cl(l+1)r^s \\ &= C\Big(s(s+1) - l(l+1)\Big)r^s \end{aligned} \tag{3.50}$$

Because this must hold for all values of r near the origin, we must have $s(s+1) = l(l+1)$, which gives two possible solutions:

$$s = 1, \text{ or } s = -(l+1) \tag{3.51}$$

Recall l is the orbital angular momentum associated with the spherical harmonics, so we have $l \geq 0$. If $s = -(l+1) < 0$, then our wavefunction will blow up near the origin. Landau and Lifshitz show that for a potential which becomes infinite near the origin more slowly than $1/r^2$, the wavefunction must remain finite, which applies to both the Coulomb and finite size potentials. This is apparent in the finite size case, which is

our current interest. If the potential $V(r)$ is finite everywhere in space, then the wavefunction $R(r)$ must also be finite everywhere in space. Therefore the appropriate solution is to take $s = l \geq 0$. To be clear, this argument is only valid for the Schrödinger wavefunctions. As we have already seen, the s-wave Dirac wavefunctions are divergent at the origin.

Since the Numerov method involves boundary conditions on the function $u(r) = rR(r)$, this implies that near the origin, the behaviour of the function is given by $u(r) \sim r^{l+1}$. Furthermore, the coefficient of proportionality is unimportant, since it will be fixed by overall normalization of the wavefunction. Hence we take the boundary conditions as

$$\begin{aligned} u_0 &= 0 \\ u_1 &= h^{l+1} \end{aligned} \tag{3.52}$$

We have emphasized that the s-waves solutions will feel finite size effects most significantly because they are finite at the origin. Although it may seem like the first boundary condition $u_0 = 0$ does not allow for this, it is important to remember that the function $u(r) = rR(r)$ is not the radial wavefunction. Given that the radial wavefunction $R(r)$ is finite at the origin, the function $u(r)$ must vanish at the origin.

3.3.3 Calculating the Potential

Before applying the numerov method to find the wavefunctions, we discuss how the potential is obtained from the nuclear charge distribution. A particle with charge e orbiting a nucleus with a symmetric charge distribution $\rho(r)$ feels a potential

$$V(r) = -e\left[\frac{4\pi}{r}\int_0^r \rho(r')(r')^2 dr' - 4\pi\int_r^\infty \frac{1}{r'}\rho(r')(r')^2 dr'\right] \tag{3.53}$$

To see how the Coulomb potential is obtained from this expression, assume for now that the orbiting particle is suitably outside the nucleus. Mathemtically, it is at some radial distance $r \geq r_c$, where r_c is some "critical" radius value outside which the charge distribution vanishes. The second term vanishes, so the potential becomes

$$\begin{aligned} V(r) &= -e\left[\frac{4\pi}{r}\int_0^{r_c} \rho(r')(r')^2 dr' - 4\pi\int_{r_c}^\infty \frac{1}{r'}\cancelto{0}{\rho(r')}(r')^2 dr'\right] \\ &= -\frac{4\pi e}{r}\int_0^{r_c} \rho(r')(r')^2 dr' \\ &= -\frac{Ze^2}{r} = -\frac{Z\alpha}{r} \end{aligned} \tag{3.54}$$

We have normalized the nuclear charge distribution so that the total nuclear charge is Ze, hence the radial charge integral evaluates to $\int_0^{r_c} \rho(r')(r')^2 dr' = Ze/4\pi$.

Recall the Numerov method requires knownledge of the function $k^2(r)$, which depends on the potential $V(r)$, at a discrete grid of points r_n. To evaluate the potential at these points, and hence find k_n, we use the Fermi charge distribution given in Eq. 3.24, with parameters a and c given in Eq. 3.25

$$V(r_n) = -e\left[\frac{4\pi}{r_n}\int_0^{r_n} \frac{\rho_0}{1+\exp(\frac{r'-c}{a})}(r')^2 dr' - 4\pi\int_{r_n}^\infty \frac{\rho_0}{1+\exp(\frac{r'-c}{a})} r' dr'\right] \tag{3.55}$$

We will perform these integrals numerically using MATLAB, but because we are dealing with femtometer distances, it will be useful to perform a change of variable for computational ease. Specifically, let $R = r'/D$, so that if D is on the order of the nuclear radius, then during the period where small changes in r' cause relatively large changes in the charge distribution (characterized by the parameter c in the Fermi distribution), the variable R will be order one and numerical integration will yield accurate results. Effectively, we are zooming in by a factor of D, in order for the integration bins to be small compared to the scale of change in the charge distribution. We note that the argument of the exponential can be written

$$\frac{r'-c}{a} = \frac{r'/D - c/D}{a/D} = \frac{R'-C}{A} \tag{3.56}$$

where we have denoted the scaled variables will capital letters (we will use $R_n \equiv r_n/D$ later). With reference to Eq. 3.25, both Fermi parameters a and c are on the femtometer scale, a natural choice for the scaling parameter D is the nuclear charge radius c. In principal any choice of D on the femtometer scale will give good results, the choice $D = c$ is by no means unique, the muonic Bohr radius would also be a good choice. Recall that the

normalization constant ρ_0 is calculated by normalization of nuclear charge, which transforms as

$$\begin{aligned}\rho_0 &= \frac{1}{Ze}\left[\int_0^\infty \frac{1}{1+\exp(\frac{r-c}{a})} r^2 dr\right]^{-1} \\ &= \frac{1}{Ze}\left[\int_0^\infty \frac{1}{1+\exp(\frac{R-C}{A})} (DR)^2 d(DR)\right]^{-1} \\ &= \frac{D^{-3}}{Ze}\left[\int_0^\infty \frac{1}{1+\exp(\frac{R-C}{A})} R^2 dR\right]^{-1}\end{aligned} \tag{3.57}$$

With this scaling in mind, the calculation for the potential becomes

$$\begin{aligned}V(r_n) &= -e\left[\frac{4\pi}{r_n}\int_0^{r_n} \frac{\rho_0}{1+\exp(\frac{r'-c}{a})}(r')^2 dr' - 4\pi\int_{r_n}^\infty \frac{\rho_0}{1+\exp(\frac{r'-c}{a})} r' dr'\right] \\ &= -e\left[\frac{4\pi}{r_n}\int_0^{R_n} \frac{D^{-3}\rho_0}{1+\exp(\frac{R'-C}{A})}(DR')^2 d(DR') - 4\pi\int_{R_n}^\infty \frac{D^{-3}\rho_0}{1+\exp(\frac{R'-C}{A})} DR' d(DR')\right] \\ &= -e\left[\frac{4\pi}{r_n}\int_0^{R_n} \frac{\rho_0}{1+\exp(\frac{R'-C}{A})}(R')^2 dR' - \frac{4\pi}{D}\int_{R_n}^\infty \frac{\rho_0}{1+\exp(\frac{R'-C}{A})} R' dR'\right]\end{aligned} \tag{3.58}$$

Because ρ_0 has units of charge per unit volume, it scales as $1/\text{Volume} = 1/D^3$ when we zoom in by a factor of D. In the first term of the potential, this is cancelled by the Jacobian $r^2 dr$. However due to the extra factor of $1/r'$ originally appearing in the second term (Eq. 3.24), we end up with an overall factor of $1/D$. The resulting potential is plotted with a solid blue curve in figure 3.2, with scale in MeV given by the left y-axis. The Fermi charge distribution has been overlaid in orange, with scale given by the right y-axis, to show that the Fermi potential and the Coulomb potential (plotted as a blue dotted curve) coincide for distances larger than the charge radius, where the Fermi charge distribution is exponentially suppressed.

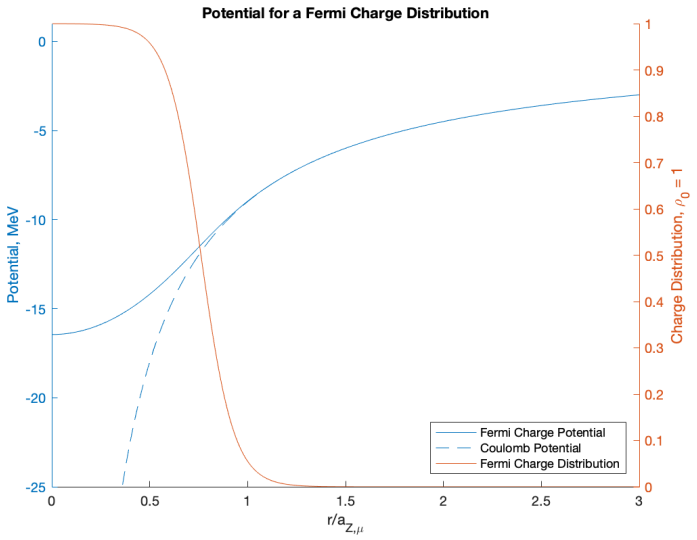

Figure 3.2: The potential found from the Fermi charge distribution is nearly identical to the Coulomb potential outside the nuclear charge radius, but differs significantly as we move towards the origin.

3.3.4 Finding The Energy Eigenstates

So far, with reference to Eq. 3.37, for a particular orbital angular momentum value l, everything is known except for the energy eigenvalue E. We can attempt to find the energy eigenvalues by guessing the value of E, and then determining the wavefunction via repeated application of the Numerov recursive relation given in Eq. 3.47. If we dont have the correct value of E, the wavefunction will quickly shoot off to $\pm\infty$, giving wavefunctions that are not square integrable, and hence not normalizable. Even with energy values extremely close, although the wavefunctions will give the correct shape near the origin, they will exponentially increase not too far from the origin, so the proper wavefunctions require a very accurate guess of the energy eigenvalue. To demonstrate this, the Numerov method was used to find the ground state energy and wavefunction of the Coulomb potential

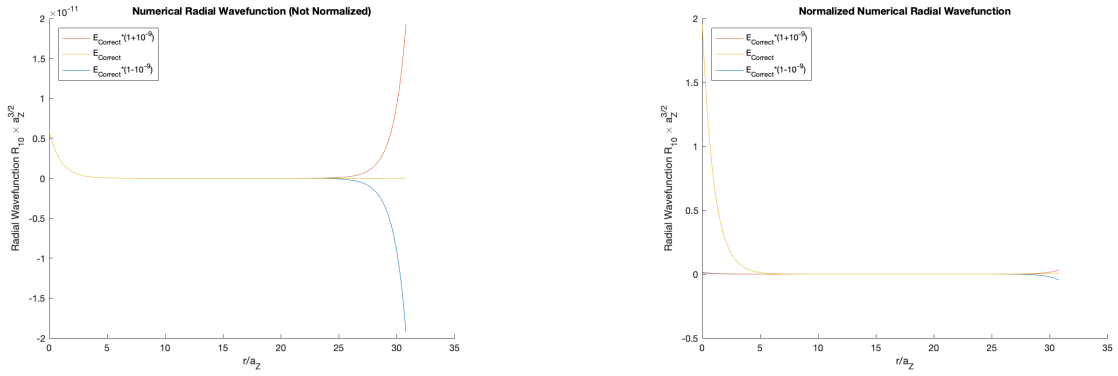

(a) Numerical Solutions, not normalized.

(b) Numerical solutions, normalized.

Figure 3.3: The ground state radial wavefunction for the Coulomb potential ($Z = 40$), and the numerical solutions found by altering the energy guess very slightly. The blue curve represents an energy guess too large by $10^{-7}\%$, and the red curve represents an energy guess too small by the same amount.

for Zirconium ($Z = 40$). We then altered the energy guess by one part in a billion, and plotted the results in figure 3.3.

The plot on the left displays the numerical solutions before normalization, whereas the right plot displays the numerical solutions once they have been normalized. The yellow curve represents the most accurate numerical solution for the ground state radial wavefunction. The blue curve is found by increasing the energy guess (recall the correct energy is negative) by one part in a billion, and the red curve is found by decreasing the energy guess by the same amount. Although their behaviour near the origin seems to be correct, they clearly deviate siginficantly further out. Note that these wavefunctions have not been normalized, and once this is taken into account the difference also becomes apparent near the origin, where the incorrect guesses lead to normalized wavefunctions that appear to vanish. Since the incorrect guesses feature a growing wavefunction far from the origin, this will have a greater effect on the norm due to the $r^2 dr$ volume element. The result, displayed on the right shows that the form of the normalized wavefunctions is very different once the normalization has been taken into account.

At first this seems hopeless, if we need accuracy better than 10^{-9}, then we would have to guess potentially tens or even hundreds of billions of energy eigenvalues, before hoping to get the correct one. Although one could be smart and have some form of detecting when the energy values are close, by measuring if they are near zero for a while (as in the above plots), there is an easier method, called the Wag-the-Dog Method.

The idea behind the Wag-the-Dog method is to pick a starting energy, $E_0^{(1)}$, and compute the wavefunction using a recursion relation, such as the Numerov method. In the vast majority of cases, the wavefunction will shoot off to infinity. One then increases (or decreases) by some chosen amount, $\Delta E^{(1)} = \Delta E$, and uses the same recursion relation to compute the wavefunction. If the asymptotic behaviour is the same, the process is continued, and we attempt again after adding another energy step ΔE. Suppose that this process continues up to (and including) the energy value $E_m^{(1)} \equiv E_0^{(1)} + m\Delta E$, and then when we try it with energy $E_{m+1}^{(1)} = E_m^{(1)} + \Delta E$, the asymptotic behaviour flips. That is, the wavefunction with energy parameter $E_m^{(1)}$ asymptotes to infinity whereas the wavefunction with energy $E_{m+1}^{(1)}$ asymptotes to negative infinity. This means that in adding ΔE to $E_m^{(1)}$, we have skipped over an energy eigenvalue, where the wavefunction will asmpytote to zero. The case where its behaviour switches from negative infinity to infinity is treated in a similar manner. In other words, there exists an energy eigenvalue in the interval $(E_m^{(1)}, E_m^{(1)} + \Delta E)$. This is shown above in figure 3.3. In jumping from the red to blue curve (or vice versa), we have crossed over an yellow curve representting an energy eigvenvalue, so we know that the correct value is somewhere between our two previous guesses. This example was chosen to display the senstitivity of the asymptotic behaviour on the energy guess. In practice one should start with a much larger energy step ΔE, so that the search is more efficient.

We can now proceed in the same manner starting from energy $E_0^{(1)} \equiv E_m^{(1)}$ with energy step size $\Delta E^{(2)} = \Delta E/2$, until we find the value where its asymptotic behaviour flips sign. Because our energy step is half as large, this second iteration of scanning energies and studying asymptotic behaviour will allow us to constrain the energy eigenvalue within an energy interval which is twice as small. In general, the n-th repetition of this procedure will involve energy steps of size $E^{(n)} = \Delta E/(2n)$. Repeating this behaviour by keeping track of the previously tested energy guesses and the corresponding asymptotic behaviour of the wavefunction allows one to determine the energy eigenvalue to arbitrary precision, within computational limits. The method gets its name due to the fact that making a jump over an energy eigenvalue cause the wavefunction to switch the sign of its asymptotic behaviour, as if the tail of the wavefunction is "wagging" back and forth.

Using the notation developed in the Numerov method, we are computing the wavefunction on a discrete radial grid with points $r_n = n \times h$, where $n = 0, 1, \ldots, n_{max}$ indexes the grid position. In this notation the furthest radial distance is given by hn_{max}. In principle, we could take n_{max} to be arbitrarily large, but this increases computation time for no gain in precision. When we discuss aymptotic behaviour in the previous paragraph, we mean the behaviour at distance hn_{max}, and our condition to have an energy eigenvalue implies that we require the radial wavefunction to be suitably small at this point. This maximum distance must be chosen so that the wavefunctions are expected to be small in this area, otherwise we could claim a false energy eigenvalue if this happened to be a node of another the radial wavefunction. An energy eigenvalue that was somewhat accurate may produce the correct node coinciding with our maximum radial grid position, but fail to display the correct behaviour further out.

There are a couple potential issues with this method. To reduce computation time, one should choose a reasonable guess for the starting energy $E_0^{(1)}$, and an intial energy step large enough to scan a wide variety of energies. If the energy step is too small, time will be lost while the program evaluates the Numerov method for a large part of the parameter space where there are no energy eigenvalues. If the step is chose too large however, there may be issues by skipping over two energy eigenvalues at once. Neither of these are issues in the case of interest as the pointlike nuclear energies are a good approximation to start. In particular, we have seen that the finite size potential is not as deep near the origin (c.f. figure 3.2), so the particles will be less tightly bound to the nucleus. With this in mind, the pointlike energy eigenvalues will give a lower bound for the finite size eigenvalues. Alternatively one could avoid skipping mulitple energy eigenvalues by counting the number of nodes the wavefunctions has between successive attempts, which increase with the principle quantum number.

Once the energy eigenvalues are determined to suitable precision, the resulting wavefunction can be normalized. The integral to calculate the norm of the wavefunction may be approximated by

$$\int_0^\infty |R_{nl}(r)|^2 r^2 dr \approx \sum_{n=0}^{n_{max}} |R_{nl}(r_n)|^2 \times (r_n)^2 \times h \tag{3.59}$$

where h is the step size of the radial grid, which takes the place of the integral bin width dr. As before, a smaller step size will yield more accurate numerical wavefunctions as well as more accurate numerical integrals. Note that we have approximated the integral by a sum of bins, with bin width h and height equal to the integrand value at the left-hand side of the numerical bin. We could have also chosen to take the value in the middle of the bin or the value on the right-hand side. In principle these will produce slightly different results, but given that the step size (and hence bin width) is small, these effects are negligible. This method will also be used to calculate numerical integrals resulting from radial matrix elements.

3.3.5 Numerical Solutions for the Fermi Charge Distribution

In our implementation of the Numerov method, we chose a radial grid length of $h = 0.02$fm, with 10 000 total steps, for a maximum radial distance of r_{max} =200fm. In terms of the muonic Bohr radius, $a_{Z,\mu} = 6.40$fm, the grid length is $h = a_{Z,\mu}/320$, with maximum distance $r_{max} = 31.25 a_{Z,\mu}$. The Fermi charge distribution changes on scales comparable to the muonic Bohr radius, so that our choice of grid length is small enough to ensure that no significant changes happen in either the radial wavefunction or the potential between two consecutive radial bins. The energy search loop was terminated once an accuracy of 0.001eV was reached (i.e. $\Delta^{(n)} < 0.001$eV).

The muonic Zirconium energies are found from the numerical solutions to Schrödinger's equation, afterwards including the fine structure perturbations (relativistic kinematic, spin-orbit, and Darwin term), see Table 3.1. These are very close to energies given by Phan et al. [27] achieved by solving the Dirac equation numerically with a Fermi distribution for the nuclear charge, which are given in the third column (entries left blank were not given).

The relativistic kinematic perturbation is found by expanding the kinetic energy of the muon in a Taylor expansion with $m \gg p \equiv |\mathbf{p}|$, and taking the leading term not captured by Newtonian kinetic energy. We find

$$E_{Kin} = \sqrt{\mathbf{p}^2 + m^2} - m \approx \frac{p^2}{2m} - \frac{p^4}{8m^3} + \cdots \tag{3.60}$$

This second term gives rise to the relativistic perturbation, which we can rewrite as

$$H_{Rel.Kin.} = -\frac{1}{2m}\left(\frac{p^2}{2m}\right)^2 = -\frac{1}{2m}\Big(H_0 + V(r)\Big)^2 \tag{3.61}$$

In the last line we have related the kinetic energy term and the Coulomb term in the original Hamiltonian $H_0 = p^2/2m - V(r)$, where $V(r)$ is the potential the muon feels due to the finite size nucleus. When we take expectation values to find the energy shifts, the operator H_0 yields the energy of the state, and we are left with

Table 3.1: Numerical Energies for the Muonic Nuclear Ground State

Muonic State	Numerical Energy (keV)	Dirac Numerical Energies (keV) [27]
$1s_{1/2}$	-3644.6	-3642.965
$2s_{1/2}$	-1021.6	-1021.254
$2p_{1/2}$	-1134.8	-1147.770
$2p_{3/2}$	-1111.7	-1126.996
$3s_{1/2}$	-468.5	
$3p_{1/2}$	-503.9	-507.998
$3p_{3/2}$	-495.5	-502.049
$4s_{1/2}$	-268.7	
E_{Nuc}	1760.7	

finding $\langle 1/r \rangle$

$$\begin{aligned} \langle nlm|H_{Rel.Kin.}|nlm\rangle &= -\frac{1}{2m}\left\langle nlm\left|\left(H_0+V(r)\right)^2\right|nlm\right\rangle \\ &= -\frac{1}{2m}\left[E_{nl}^2+2E_{nl}\langle nlm|V(r)|nlm\rangle+\langle nlm|V^2(r)|nlm\rangle\right] \end{aligned} \tag{3.62}$$

Unlike the Hydrogen-like atoms, we do not have an analytic expression for the wavefunctions, so the remaining expectation values are calculated numerically. The integrals found in the expectation values were computing using numerical sums, using a rectangular bins with the same width as the step size used to determine the wavefunctions. We also note that our (non-perturbed) energies depend on the orbital angular momentum l as well as the principal radial quantum number n, unlike the Hydrogen atom.

The spin-orbit perturbation arises from the interaction of the spin of the muon and a magnetic field

$$H_{S.O.} = -\boldsymbol{\mu}\cdot\mathbf{B} \tag{3.63}$$

where $\boldsymbol{\mu} = -e/m\mathbf{S}$, and $\mathbf{S}$ is the spin operator of the muon. The magnetic field arises from the uniform velocity of the muon moving through the electric field of the proton. Mathematically

$$\mathbf{B} = -\mathbf{v}\times\mathbf{E} = \mathbf{v}\times\boldsymbol{\nabla}\phi(r) = \mathbf{v}\times\frac{\mathbf{r}}{r}\frac{d\phi(r)}{dr} \tag{3.64}$$

where $\phi(r) = V(r)/e$. Hence the spin orbit interaction is

$$\begin{aligned} H_{S.O.} &= \frac{e}{m}\mathbf{S}\cdot\mathbf{v}\times\mathbf{r}\frac{1}{r}\frac{d\phi(r)}{dr} \\ &= \frac{1}{m^2}\mathbf{S}\cdot\mathbf{p}\times\mathbf{r}\frac{1}{r}\frac{dV(r)}{dr} \\ &= \frac{1}{m^2}\mathbf{S}\cdot\mathbf{L}\frac{1}{r}\frac{dV(r)}{dr} \\ \text{(Thomas precession)} &= \frac{1}{2m^2}\mathbf{S}\cdot\mathbf{L}\frac{1}{r}\frac{dV(r)}{dr} \end{aligned} \tag{3.65}$$

In reality, there is an extra factor of 2, arising from Thomas precession [7] which we have included in the last line. To evaluate $\langle\mathbf{S}\cdot\mathbf{L}\rangle$, we note that the total angular momentum $\mathbf{J}$ is defined via $\mathbf{J}\equiv\mathbf{L}+\mathbf{S}$, so that

$$\begin{aligned} \mathbf{J}^2 = (\mathbf{S}+\mathbf{L})^2 &= \mathbf{S}^2+\mathbf{L}^2+2\mathbf{S}\cdot\mathbf{L} \\ \mathbf{S}\cdot\mathbf{L} &= 1/2(\mathbf{J}^2-\mathbf{L}^2-\mathbf{S}^2) \end{aligned} \tag{3.66}$$

If we diagonalize our spin states in terms of eigenvalues of $\mathbf{J}^2$ and J_z (instead of $\mathbf{L}^2$ and L_z), then we find [5]

$$\begin{aligned} \mathbf{S}\cdot\mathbf{L}|l+1/2,s+1/2\rangle &= l/2|l+1/2,s+1/2\rangle \\ \mathbf{S}\cdot\mathbf{L}|l-1/2,s+1/2\rangle &= -(l+1)/2|l-1/2,s+1/2\rangle \end{aligned} \tag{3.67}$$

Again we turn to numerical methods to evaluate the remaining expectation value, $\langle r^{-1}V'_{f.s}\rangle$.

Lastly the Darwin perturbation can be schematically interpreted as the smearing out of the potential. Due to the uncertainty principle, the muon's position can only be known to a certain degree. Hence it feels a potential

not from a single point, but rather an average over a volume with characteristic scale of its compton wavelength $\lambda_c = 1/m$. Taylor expanding about the center $\mathbf{r_0}$ for $|\mathbf{r}| \leq \lambda_c$

$$V(\mathbf{r_0} + \mathbf{r}) = V(\mathbf{r_0}) + \mathbf{r} \cdot \boldsymbol{\nabla} V(\mathbf{r_0}) + \frac{1}{2} \sum_{i,j} r_i r_j \nabla_i \nabla_j V(\mathbf{r_0}) \tag{3.68}$$

We now average each term over the uncertain volume, which is the sphere with radius equal to the compton wavelength. The linear term vanishes due to spherical symmetry $\int \mathbf{r} d^3 r = 0$. We evaluate the quadratic term

$$\begin{aligned}
\frac{1}{V_{sphere}} \frac{1}{2} \sum_{i,j} \int r_i r_j d^3 r \nabla_i \nabla_j V(\mathbf{r_0}) &= \frac{3}{4\pi\lambda_c^3} \frac{1}{2} \sum_{i,j} \int r_i r_j d^3 r \nabla_i \nabla_j V(\mathbf{r_0}) \\
&= \frac{3}{4\pi\lambda_c^3} \frac{1}{2} \sum_{i,j} \int n_i n_j d\Omega \int_0^{\lambda_c} r^4 dr \nabla_i \nabla_j V(\mathbf{r_0}) \\
&= \frac{3}{4\pi\lambda_c^3} \frac{1}{2} \frac{4\pi}{3} \delta_{ij} \frac{\lambda_c^5}{5} \nabla_i \nabla_j V(\mathbf{r_0}) \\
&= \frac{\lambda_c^2}{10} \sum_i \nabla_i \nabla_i V(\mathbf{r_0}) \\
&= \frac{1}{10m^2} \boldsymbol{\nabla}^2 V(r)
\end{aligned} \tag{3.69}$$

The correct numerical factor is found by expanding the Dirac equation for $p \ll m$ yielding (along with the Spin Orbit and Relativistic Kinetic terms already discussed) [7]

$$H_{Darwin} = \frac{1}{8m^2} \boldsymbol{\nabla}^2 V(r) \tag{3.70}$$

One can then use Poisson's equation $\boldsymbol{\nabla}^2 V(r) = 4\pi\rho(r)$ write

$$H_{Darwin} = \frac{\pi}{2m^2} \rho(r) \tag{3.71}$$

Although the first expression can be used to compute the expectation value, one needs to use numerical integration to find the potential, and then finite difference methods to find its Laplacian. To reduce potential numerical errors, it is simpler and more accurate to use the second expression since the analytic charge distribution is known. However one must still use numerical sums to evaluate the expectation value since we only have the numerical wavefunctions.

Here we only include the effect of the perturbations on the energy levels, not on the wavefunctions. The numerical solutions to the first few s-wave states are given below in figure 3.4 and the first two p-wave solutions are given in figure 3.5

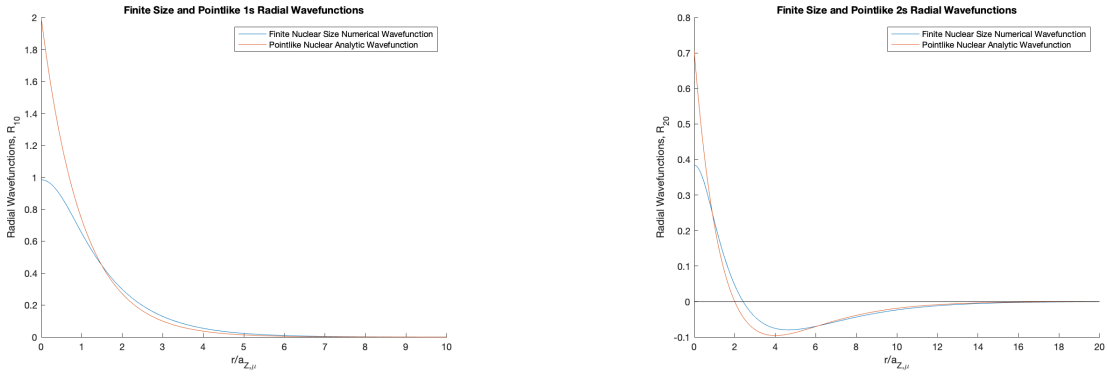

(a) The 1s radial wavefunction

(b) The 2s radial wavefunction

Figure 3.4: Numerical and pointlike radial wavefunctions for the first two s-wave states of ^{90}Zr.

It is evident that the s-waves states are significantly affected by the finite nuclear size, whereas the p-wave states are barely affected. This is easy to understand by looking at the potential in figure 3.2. Inside the nucleus, the Fermi potential forms a much more shallow well compared to the Coulomb potential. Out of all equally spaced radial intervals, the s-wave states are most likely to be found at (or nearby) the origin, and feel the effects of this shallower potential, resulting in a radial wavefunction that is smaller inside the nucleus, and hence more

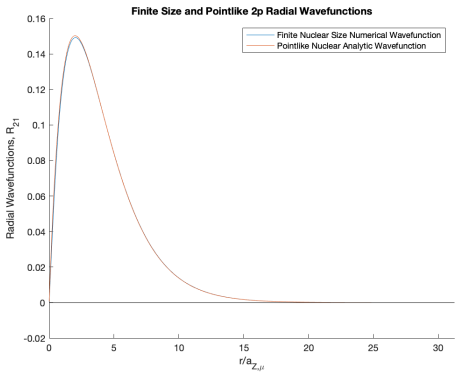

(a) The 2p radial wavefunction

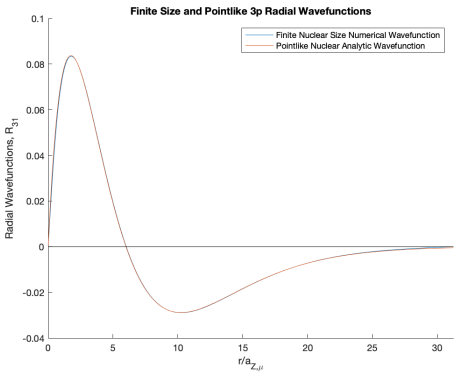

(b) The 3p radial wavefunction

Figure 3.5: Numerical and pointlike radial wavefunctions for the first two p-wave states of ^{90}Zr.

spread out in space. The p-waves are much less likely to be found near the origin due to the boundary condition $R_{np} \sim r^l$ near the origin. Hence they are less affected by this shallow well. They spend more time in the areas where the Fermi potential is comparable to the Coulomb potential, which is why their finite-size wavefunctions are nearly identical to the pointlike solutions. By the same logic, we expect that other oribtals (d,f, etc.) will not be significantly affected by the finite size potentials.

To ensure that is nothing special about the parameters we have used to compute the wavefunctions, we have also tested the program using a different total number of steps and step size, with the requirement that $r_{max} = 200$fm is fixed. We parametrized the number of steps as $1000j$ and a step size of $h = 0.2/j$fm, with the parameter j taking values between 5 to 14 (10 total variations). The s-wave energy variations are very small, within $5 \times 10^{-4}\%$, where as the p-wave variations are larger, but still within 0.02%. Note the in both cases, the rate of change increases as we go to smaller values of j. Small values of j correspond to less total steps, and a large step size, which we would expect to give less accurate results. The change in energy variations starts to flatten out as we go to higher values of j, corresponding to more steps and a smaller step size, which we would expect as numerical finite differences become a better approximation to derivatives. The radial wavefunctions displayed above are calculated using the parameter $j = 10$, which we use for the rest of the calculations.

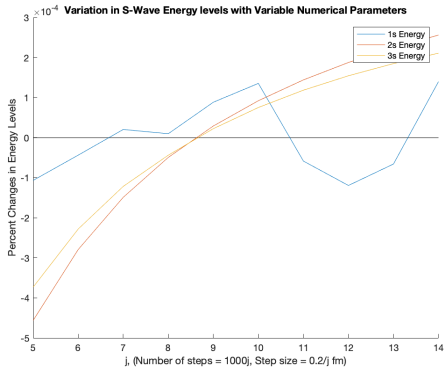

(a) S-wave energy variations

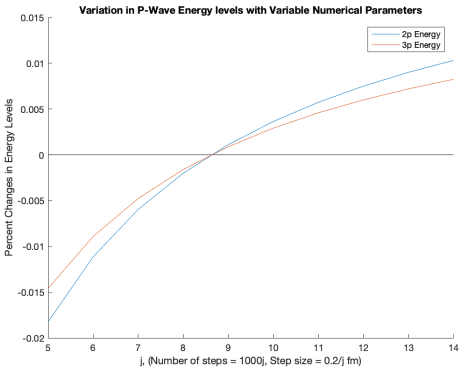

(b) P-wave energy variations

Figure 3.6: Percent variations in energy eigenvalues when altering the number of steps and step size in the Numerov method. The deviations are calculated with respect to the average over all trials.

The branching ratios do depend on the energy eigenvalues, as a ratio of energy cubed. Because the variations displayed above are so small, the results are not significantly affected by our choice of parameters.

As another check, we can modify the parameters in the Fermi distribution to mimick a pointlike nucleus, and we should recover our pointlike branching ratio results. To do this, we take the nuclear charge radius to be $c = 0.01$fm, and the diffuseness parameter to be $c = 0.001fm$, representing a very small concentrated charge that falls off quickly. In particular the charge radius is half as large as our grid size ($h = 0.02$fm), so all the charge is distributed within the first radial bin. In this case we find the branching ratios are

$$\begin{aligned} Br_{2p} &= 4.48 \times 10^{-6} \quad \text{vs. } 5.12 \times 10^{-6} \text{ (Analytic Pointlike)} \\ Br_{3p} &= 5.88 \times 10^{-6} \quad \text{vs. } 6.61 \times 10^{-6} \text{ (Analytic Pointlike)} \end{aligned} \tag{3.72}$$

Although the results are not exactly the same, they are very close to their corresponding analytic pointlike results

previously calculated, and they are significantly different from the full finite size results we shall find below. The details of the finite size computation are discussed in the next section.

3.4 Finite Size Branching Ratios

Now that we have expressions for the finite size radial wavefunctions, we can repeat our calculations for the branching ratios to populate the nuclear excited state. Recall our previous calculation, we needed the perturbative mixing parameters ϵ_{ns}, and the radial matrix elements $\langle R_{n0}|r|R_{21}\rangle$. We first study the mixings of the final state with the other s-wave states. Although the potential is non-zero for $r \neq 0$, there is still zero mixing with the other orbital states (i.e. p,d,f etc.) due to spherical symmetry of the potential and orthogonality of the spherical harmonics. In the pointlike nuclear case, the significant contributions to the branching ratio were from the mixing with the $|n00\rangle|0\rangle, n = 1, 2$ states. For now, we will include states up to $n = 4$ to ensure the contributions from the $n \geq 3$ terms are still negligible. Thus our perturbed final wavefunctions is

$$\begin{aligned}\psi_f &= |100\rangle|1\rangle + \sum_{nlm} \frac{B\langle nlm|N_{nuc}(r)|100\rangle}{E_{1s} + E_{Nuc} - E_{ns}}|nlm\rangle|0\rangle \\ &\approx |100\rangle|1\rangle + \sum_{n=1}^{4} \epsilon_{ns}|n00\rangle|0\rangle\end{aligned} \tag{3.73}$$

where the mixing coefficients and matrix elements are given by

$$\epsilon_{ns} \equiv \frac{B\langle n00|N_{nuc}(r)|100\rangle}{E_{1s} + E_{Nuc} - E_{ns}} \tag{3.74}$$

Note that we can no longer ignore the orbital type (i.e. s,p,d,etc.) when describing the energy eigenvalues because they are no longer degenerate. The results of the mixing coefficients as well as the E1 transition matrix element are given in Table 3.2, with the total branching ratio at the bottom.

As before we want to study how this excited nuclear state ($|100\rangle|1\rangle$) is populated in this approach. Due to the mixing of the s-wave nuclear ground states, $|n00\rangle|0\rangle$, it can be populated via E1 transitions. If we start with a muonic 2p state, the ratio of decays to the nuclear excited state compared to the nuclear ground state is given by the branching ratio

$$Br_{2\mathrm{p}} = \frac{\Gamma_{|210\rangle|0\rangle\to|100\rangle|1\rangle}}{\Gamma_{|210\rangle|0\rangle\to|100\rangle|0\rangle}} \tag{3.75}$$

Given that both transitions are E1 transitions, whose transition probability is given by $\Gamma = 4/3\omega^3\alpha|\mathbf{r}|^2$, the branching ratio is given by

$$\begin{aligned}Br_{2\mathrm{p}} &= \frac{E_\mu^3}{E_{2p\to1s}^3}\left|\sum_{n=1}^{4}\epsilon_{ns}\frac{\langle R_{n0}|r|R_{21}\rangle}{\langle R_{10}|r|R_{21}\rangle}\right|^2 \\ &= \frac{E_\mu^3}{E_{2p\to1s}^3}\left|\sum_{n=1}^{4}\frac{B\langle R_{n0}|N_{Nuc}(r)|R_{10}\rangle}{E_{1s} + E_{Nuc} - E_{ns}}\frac{\langle R_{n0}|r|R_{21}\rangle}{\langle R_{10}|r|R_{21}\rangle}\right|^2\end{aligned} \tag{3.76}$$

As before, $E_\mu = E_{2s} - (E_{1s} + E_{Nuc})$. We now return to the question of perturbative mixing in the initial state. In the point-like case, the internal conversion perturbation was a delta function, reflecting the pointlike charge distribution. We considered mixing of the final state due to this perturbation. There was no mixing of the initial state because the p-wave states are zero-valued at the origin where the perturbation acts. Since we now have a finite size nuclear charge distribution, the perturbation will generate non-zero mixing between the p-wave states of the initial state. We expect this effect to be small as the p-wave states are still suppressed near the origin compared to the s-wave states, but as the Bohr radius is comparable to the nuclear charge radius, we should calculate the size

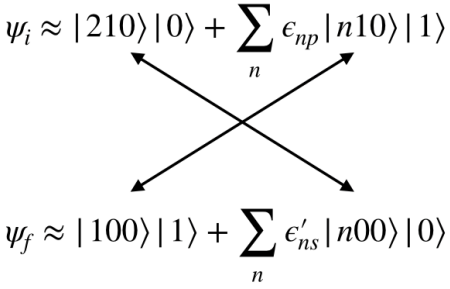

Figure 3.7: Perturbed initial and final wavefunctions are shown above. The solid lines connect the states with non-zero E1 matrix elements

of this effect. A visual interpretation of the process
is shown in figure 3.7, with the different involving the extra terms added onto the initial state. Including the perturbative effects on the initial state, we have

$$\begin{aligned} |i\rangle &= |210\rangle|0\rangle + \sum_{n10} \frac{B\langle n10|N_{nuc}(r)|210\rangle}{E_{2p} - (E_{n10} + E_{Nuc})}|n10\rangle|1\rangle \\ &\approx |100\rangle|1\rangle + \sum_{n=2}^{3} \epsilon_{np}|n10\rangle|1\rangle \end{aligned} \tag{3.77}$$

where the mixing coefficients and matrix elements are given by

$$\epsilon_{np} \equiv \frac{B\langle n10|N_{nuc}(r)|210\rangle}{E_{2p} - (E_{np} + E_{Nuc})} \tag{3.78}$$

We ignore the fine structure splitting between the $p_{1/2}$ and $p_{3/2}$ for simplicity, since the energy differences are not significant. We have only included the first two p-wave mixings because we will find they are much smaller than the s-wave mixings, in principle both of these sums involve an infinite number of terms. The inclusion of initial state mixing modifies the branching ratio to be

$$Br_{2\mathrm{p}} = \frac{E_\mu^3}{E_{2p\to 1s}^3}\left| \sum_{n=1}^{4} \epsilon_{ns} \frac{\langle R_{n0}|r|R_{21}\rangle}{\langle R_{10}|r|R_{21}\rangle} + \sum_{n=2}^{3} \epsilon_{np} \frac{\langle R_{n1}|r|R_{10}\rangle}{\langle R_{21}|r|R_{10}\rangle} \right|^2 \tag{3.79}$$

Each term that contributes to the decay rate contains a mixing factor (ϵ), as well as a radial matrix element ($\langle R_{n1}|r|R_{j0}\rangle$) resulting from the dipole operator. To get a feeling of the size of the effects discussed above, the numerical results for these terms are given below in table 3.2, normalized to the contribution of the 2s state (which has the largest contribution to the overall transition rate). The total branching ratio is found to be

$$Br_{2p} = 5.35 \times 10^{-8} \tag{3.80}$$

Table 3.2: Contributions to the 2p→1s Transition Rate due to Mixing with Various States

Initial/Final State	Contribution to Transition Rate (Normalized to 2s Contribution)
Mixing of Final States (s-waves)	$\epsilon_{ns}\langle n00|r|210\rangle/\epsilon_{2s}\langle 200|r|210\rangle$
1s	0.45
2s	1
3s	-0.025
4s	-6.5×10^{-3}
Mixing of Initial States (p-waves)	$\epsilon_{np}\langle 100|r|n10\rangle/\epsilon_{2s}\langle 200|r|210\rangle$
2p	2.2×10^{-3}
3p	4.0×10^{-4}
Total Branching Ratio	5.35×10^{-8}

There are 2 important effects to notice in this table. The largest contribution to the sum

$$\sum_{n=1}^{4} \epsilon_{ns}\langle R_{n0}|r|R_{21}\rangle \tag{3.81}$$

appearing in the 2p transition comes from the 2s term. This result is true in general: if we now think of a transition from an np state to the 1s excited nuclear state, the most significant contribution comes from the mixing of the 1s nuclear excited state with the ns nuclear ground state. Furthermore, terms in the sum with $j > n$ decrease very quickly, so we are justified in terminating the sum at $j = n$. The second important effect is the size of the contributions due to the initial state mixing, with parameter ϵ_{np}. As seen above, these effects are small compared to those introduced by the final state mixings, so we will also ignore them.

A similar analysis can be done if the initial muon is in the 3p state, corresponding to $|310\rangle|1\rangle$. In this case, the 3p state can transition to both the 2s and 1s states, so the total decay rate is given by

$$\Gamma_T \approx \Gamma_{3p\to 1s} + \Gamma_{3p\to 2s} \tag{3.82}$$

Because of these two terms, the branching ratio can't be put into the same form as is done for the 2p branching ratio (eq. 3.11), where the result is a combination of ratios comparing the transition to the 1s nuclear excited state and 1s nuclear ground state. Instead we have

$$Br_{3p} = \frac{(E_{3p} - E_{1s} - E_{Nuc})^3 \left| \sum_{n=1}^{3} \epsilon_{ns} \langle R_{3p}|r|R_{ns}\rangle \right|^2}{\sum_{n=1}^{2}((E_{3p} - E_{ns})^3 |\langle R_{3p}|r|R_{ns}\rangle|^2} \tag{3.83}$$

Upon performing the calculation, we find the branching ratio to be

$$Br_{3p} = 1.60 \times 10^{-8} \tag{3.84}$$

In both cases, including the finite size effects caused our branching ratio to decrease by a factor of approximately 90 (Br_{2p}) and 420 (Br_{3p}).

3.4.1 A Closer Look at the Finite Size Effects

Because the finite size corrections are so large, we will study the decays in more detail to understand what is causing the suppression. We need to investigate three calculations

1. The energy ratio, $(E_{2p \text{ g.s.}\to 1s \text{ exc.}}/E_{2p \text{ g.s.}\to 1s \text{ g.s.}})^3$
2. The radial matrix elements, $\langle R_{21}|r|R_{20}\rangle$, $\langle R_{21}|r|R_{10}\rangle$
3. The mixing parameters, $|\epsilon_{ns}|^2 = |\langle 100|V|n00\rangle/(E_1 + E_{Nuc} - E_n)|^2$

The finite nuclear size effects are felt most by the s-wave states, since they have a large (compared to other states) probability of being near the origin. Using the numerical solutions, we find the relevant energies are

$$\begin{aligned} E_1 + E_{Nuc} - E_2 &= -866\text{keV} \\ E_{2p \text{ g.s.}\to 1s \text{ exc.}} &= 749\text{keV} \\ E_{2p \text{ g.s.}\to 1s \text{ g.s.}} &= 2510\text{keV} \end{aligned} \tag{3.85}$$

The finite nuclear size shrinks the binding energy, causing the energy spectrum to be denser. This results in

$$\left(\frac{E_{2p \text{ g.s.}\to 1s \text{ exc.}}}{E_{2p \text{ g.s.}\to 1s \text{ g.s.}}}\right)^3 = \left(\frac{749\text{keV}}{2510\text{keV}}\right)^3 = 0.0266 \tag{3.86}$$

In the pointlike case this factor was 0.1096, so we have a decrease by a factor of approximately 4.1.

For the radial matrix elements, the effect of the finite size on the s-wave states is to push the wavefunction away from the origin. For the 1s and 2s states, this causes a supression in the wavefunction inside the nucleus. Outside the nucleus, the wavefunctions are larger (compared to their pointlike counterparts). The shift happens on the order of the nuclear radius ($R_N = 0.76a_{Z,\mu}$), and differs slightly for the 1s and 2s states. Plots of the finite size and pointlike wavefunctions are shown below in figure 3.8.

This effect is minor on the radial matrix element between the 2p and the 2s states, but more signficant for the matrix element between the 2p and 1s state, because the 1s wavefunction is pushed away from the origin, where the 2p wavefunction is larger. Although the 2s wavefunction is also pushed away from the origin, it is already comparable to the 2p wavefunction, so the effect is less noticeable. The integrands in the matrix elements $\langle R_{21}|r|R_{n0}\rangle$ are plotted in figure 3.9 below, and one can see the effect of the finite size nucleus on the 2p-1s matrix element. Evaluating these matrix elements gives

$$\begin{aligned} \langle R_{21}|r|R_{20}\rangle &= -5.180a_{Z,\mu} \text{ (vs Pointlike } = -5.196a_{Z,\mu}) \\ \langle R_{21}|r|R_{10}\rangle &= 1.763a_{Z,\mu} \text{ (vs Pointlike } = 1.290a_{Z,\mu}) \end{aligned} \tag{3.87}$$

Lastly we need to compute the change to the mixing parameters for $n = 1, 2$,

$$\epsilon_{ns} = \frac{\langle 100|V|n00\rangle}{E_1 + E_{Nuc} - E_n} \tag{3.88}$$

We already know the energy from above, $E_1 + E_{Nuc} - E_2 = -0.866$MeV, so we must compute the matrix element $\langle 100|V|n00\rangle = \langle 100|BN_{Nuc}(r)|n00\rangle$. Recall we normalized the nuclear distribution to ensure the constant B was identical in both the pointlike case and the finite size case. This implies we can focus on comparing $\langle 100|N_{Nuc}(r)|n00\rangle|_{FS}$ to $\langle 100|\delta^3(\mathbf{r})|n00\rangle|_{PL}$, where the subscript FS indicates we should use the numerical muonic wavefunctions corresponding to the finite size nucleus, and PL indicates we should use the analytic muonic wavefunctions corresponding to a pointlike nucleus. The results are given in table 3.3

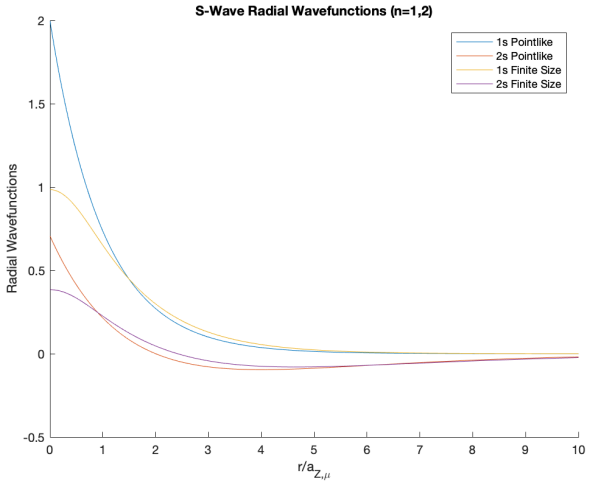

Figure 3.8: The first two s-wave states for pointlike and finite size nuclear distributions. The radial coordinate is scaled by $a_{Z,\mu}^{-1}$ and the radial wavefunctions are scaled by $a_{Z,\mu}^{-3/2}$.

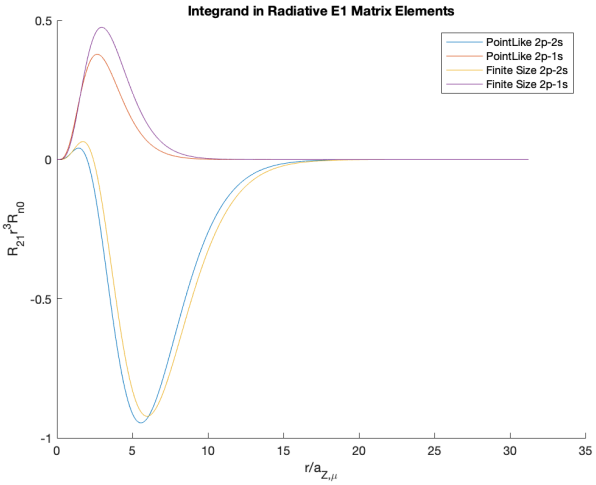

Figure 3.9: The integrands appearing in the radial matrix elements for pointlike and finite size nuclear distributions. Note that the 2p-1s radial matrix element is more significantly affected by the finite size nuclear effects. The radial coordinate is scaled $a_{Z,\mu}^{-1}$ and the radial wavefunctions are scaled by $a_{Z,\mu}^{-3/2}$.

Hence we find

$$\left|\epsilon_{1s} + \epsilon_{2s}\frac{\langle R_{21}|r|R_{20}\rangle}{\langle R_{21}|r|R_{10}\rangle}\right|^2 = 2.10 \times 10^{-6} \tag{3.89}$$

In this pointlike case this factor was 4.63×10^{-5}, so we find a decrease of a factor of 22. Combining this with the suppression of 4.12 from the energy ratio, we find the Branching Ratio should decrease by approximately 90, as we had previously calculated.

Note that in the 2s mixing parameter, the smaller energy gap causes the pertubative mixing to be higher,

$$|E_1 + E_{Nuc} - E_2|_{PL}^2 \approx 0.3|E_1 + E_{Nuc} - E_2|_{FS}^2 \tag{3.90}$$

However the matrix element is much smaller in the finite size case

$$|\langle 100|\delta^3(\mathbf{r})|200\rangle|_{PL}|^2 \approx 32|\langle 100|N_{Nuc}(r)|200\rangle|_{FS}|^2 \tag{3.91}$$

The matrix element in the pointlike nucleus case evaluates the wavefunctions at the origin. A convenient way to view this (in comparison to the finite size case) is to imagine the integrand as a rectangular function, with unit width, and height equal to the wavefunctions evaluated at the origin. The matrix element is just the area of the rectangle, equal to the height since it has unit width. In contrast, the integrand in the matrix element of the finite size nucleus must be numerically integrated. These two integrands are shown below in figure 3.10. There are a few things to note. Firstly, its is obvious that the pointlike case dominates because of two effect. The

Table 3.3: Comparison of the Pointlike and Finite Size Effects in the Branching Ratios to Populate the Excited Nuclear State

Transition Parameter	Pointlike	Finite Size
ϵ_{1s}	2.67×10^{-3}	4.47×10^{-4}
ϵ_{2s}	1.03×10^{-3}	-3.41×10^{-4}
$\langle R_{21}\|r\|R_{10}\rangle$	$1.290 a_{Z,\mu}$	$1.763 a_{Z,\mu}$
$\langle R_{21}\|r\|R_{20}\rangle$	-5.196$a_{Z,\mu}$	-5.180$a_{Z,\mu}$

delta function potential picks out the s-wave wavefunction values at the origin, where they are largest, and in this view, extends them uniformly to $r = 1$. Furthermore, these are the pointlike wavefunctions, which we have already noted are larger then their finite size counterparts for distances $r \lesssim R_N$, see figure 3.8. Secondly, the delta function does not feel the "suppression" of the r^2 term in the volume element of spherical coordinates. In contrast, we see that the finite size nuclear distribution is suppressed near the origin due to this r^2 term, exactly where the wavefunctions are largest. This allows us to understand why this matrix element is much larger for the finite size case, the delta potential largely overestimates the size of this mixing.

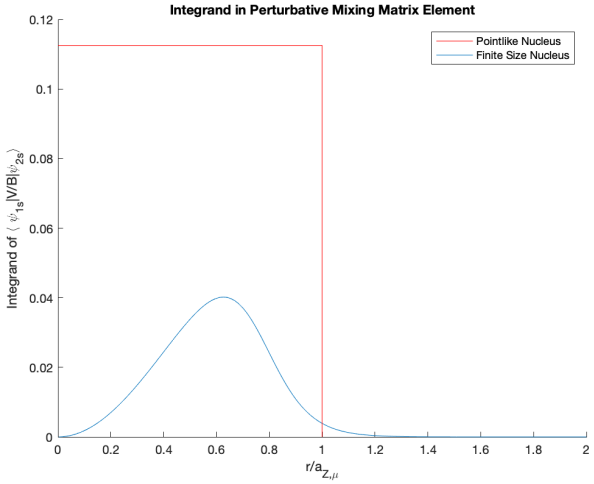

Figure 3.10: The integrands appearing in the perturbative mixing matrix elements for pointlike and finite size nuclear distributions. Note that we have scaled the potential by its strength parameter B. The suppression of the finite size nuclear integrand near the origin is due to the factor of r^2 appearing in the spherical volume element.

Lastly, why is the mixing suppressed by 420 times in the case of the 3p branching ratio, compared to only 90 times in the 2p branching ratio? Recall the 2p branching ratio contains the term

$$|\epsilon_{1s}\langle R_{21}|r|R_{10}\rangle + \epsilon_{2s}\langle R_{21}|r|R_{20}\rangle| \tag{3.92}$$

where as the 3p branching ratio contains

$$|\epsilon_{1s}\langle R_{31}|r|R_{10}\rangle + \epsilon_{2s}\langle R_{31}|r|R_{20}\rangle + \epsilon_{3s}\langle R_{31}|r|R_{30}\rangle| \tag{3.93}$$

In the 2p case, the two terms constructively interfere, where as in the 3p case, there is a fine cancellation caused by destructive interference between the contribution from the $n = 2, 3$ terms. This destructive interference is not as significant in the pointlike case. The numerical results, which have been scaled by $10^3/a_{Z,\mu}$ to make this cancellation more clear, are summarized below in table 3.4.

We can see the fine cancellation between the terms due to mixing from the 2s and 3s wavefunctions in the finite size case. Nearly all the final sum comes from the 1s mixing term. Each finite size term is smaller than its pointlike counterpart due to the delta function overestimating the mixing, as discussed above (see figure 3.10 and preceding discussion).

Summarizing, we find that there is a very small chance to populate the excited nuclear state with a muon. Although a quick calculation gives a braching ratio on the order of one in a million atoms, we find that finite size effects are extremely important. These effects decrease the branching ratio by nearly a two orders of magnitude, significantly lowering the rate at which the excited nuclear state can be populated.

Table 3.4: Comparing the Pointlike and Finite Size Effects

Transition Parameter$\times 10^3/a_{Z,\mu}$	Pointlike	Finite Size
$\epsilon_{1s}\langle R_{31}\|r\|R_{10}\rangle$	1.38	0.276
$\epsilon_{2s}\langle R_{31}\|r\|R_{20}\rangle$	-3.15	-1.48
$\epsilon_{3s}\langle R_{31}\|r\|R_{30}\rangle$	5.14	1.47
Sum of 3 terms	3.36	0.27

Chapter 4

Decay Modes for Muonic Nuclear De-excitation

Now that we have studied how to populate the excited nuclear state of muonic zirconium, we must investigate how it can decay. As we previously saw (cf. Table 3.1), the energy gap between the muonic ground state and the excited state is larger than the nuclear excitation energy, which implies that the excited state must decay into the full ground state. Also recall that a muon that makes the transition into the nuclear excited state ($|100\rangle|1\rangle$) has perturbed wavefunction

$$\begin{aligned} \psi_i &= |100\rangle|1\rangle + \epsilon_{i,1s}|100\rangle|0\rangle + \epsilon_{i,2s}|200\rangle|0\rangle + \cdots \\ \epsilon_{i,ns} &\equiv \frac{\langle 100|V|n00\rangle}{E_1 + E_{Nuc} - E_n} \end{aligned} \tag{4.1}$$

The full ground state will also include some perturbative mixing, given by

$$\begin{aligned} \psi_f &= |100\rangle|0\rangle + \sum_{n=1}^{\infty} \frac{\langle 100|V|n00\rangle}{E_1 - (E_{Nuc} + E_n)}|n00\rangle|1\rangle \\ \psi_f &\equiv |100\rangle|0\rangle + \epsilon_{f,1s}|100\rangle|1\rangle + \epsilon_{f,2s}|200\rangle|1\rangle + \cdots \end{aligned} \tag{4.2}$$

The mixing parameter $\epsilon_{i,ns}$ in the initial are identical to the parameters ϵ_{ns} used in the previous chapter, with the slight change of notation now necessary to distinguish between final and initial state mixing. The parameters $\epsilon_{f,ns}$ only differ by a change of E_{Nuc} in the denominator, implying that $\epsilon_{i,1s} = -\epsilon_{f,1s}$. The subscripts i and f serve to distinguish the mixing effects in the initial and final states, respectively. As before, we ignore terms with $n \geq 3$ because they are smaller by a factor of approximately 10. If this decay will be mediated by an operator $\mathcal{A}$ which does not contain any nuclear operators, the matrix element will go as

$$\begin{aligned} \langle f|\mathcal{A}|i\rangle &= \Big(\langle 0|\langle 100| + \epsilon_{f,1s}\langle 1|\langle 100| + \epsilon_{f,2s}\langle 1|\langle 200|\Big)\mathcal{A}\Big(|100\rangle|1\rangle + \epsilon_{i,1s}|100\rangle|0\rangle + \epsilon_{i,2s}|200\rangle|0\rangle\Big) \\ &= \langle 100|\mathcal{A}|100\rangle\cancelto{0}{\langle 1|0\rangle} + \cancelto{0}{(\epsilon_{i,1s} + \epsilon_{f,1s})}\langle 100|\mathcal{A}|100\rangle + (\epsilon_{i,2s} + \epsilon_{f,2s})\langle 100|\mathcal{A}|200\rangle + \mathcal{O}(\epsilon^2) \end{aligned} \tag{4.3}$$

The first term is zero because of the nuclear orthogonality, and the second is zero because $\epsilon_{i,1s} = -\epsilon_{f,1s}$. To lowest order, our transition would involve the matrix element between the $2s$ and $1s$ states. This is depicted in figure 4.1 below, with the dotted lines representing the matrix element connecting the 1s states, which cancel as argued above. The solid black lines represent the the non-zero matrix elements which we shall focus on.

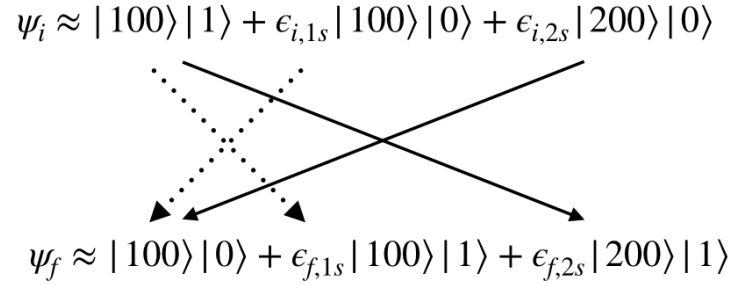

Figure 4.1: Perturbed initial and final wavefunctions

Hence this decay would be mediated by the operator responsible for $2s \to 1s$ transitions in hydrogen-like atoms. In a similar manner to the E0 transition, this transition involves a matrix element between states of equal spin and parity. There are two different decay modes which might be significant

1. The magnetic dipole (M1) transition
2. The two photon (2E1) transition

We begin comparing these transitions with some order of magnitude estimates. In hydrogen, the $2s \to 1s$ transition is completely dominated by the two-photon decay, with the magnetic dipole decay rate being 6 orders smaller [36]. However, the two photon decay scales with the nuclear charge as $\Gamma_{2E1} \sim Z^6$, whereas the magnetic dipole transition scales as $\Gamma_{M1} \sim Z^{10}$. Hence for hydrogen-like zirconium (i.e. a one-electron zirconium atom), we have

$$\begin{aligned} \frac{\Gamma_{M1}}{\Gamma_{2E1}} &= Z^4 \left(\frac{\Gamma_{M1}}{\Gamma_{2E1}}\bigg|_{\text{Hydrogen},Z=1} \right) \\ &= 40^4 (10^{-6}) \\ &= 2.56 \end{aligned} \tag{4.4}$$

Hence for a single electron orbiting zirconium, the magnetic dipole rates catches up to the photon rate, and they are on the same order of magnitude. Obviously our case of interest is not a one-electron zirconium, it is zirconium with one muon and 39 electrons. Since the muonic Bohr radius is 200 times smaller than the electronic Bohr radius, the muon feels essentially no screening from the electrons. To prove this, we note that the ground state is the most likely state to be found near the nucleus. The probability, P, for a ground state electron to be found within the muonic Bohr radius (using the pointlike wavefucntions) is given by

$$\begin{aligned} P &= \int_0^{a_{Z,\mu}} |R_{10,e}(r)|^2 r^2 dr \\ &= \frac{4}{a_{Z,e}} \int_0^{a_{Z,\mu}} r^2 \exp(-2r/a_{Z,e}) dr \\ &= 1 - e^{-2m_e/m_\mu} \left[1 + 2\frac{m_e}{m_\mu} + 2\frac{m_e^2}{m_\mu^2} \right] \\ &= 1.5 \times 10^{-7} \end{aligned} \tag{4.5}$$

So the one-electron approximation is a good approximation for this order of magnitude comparison. This is only an estimate however, since the M1 and 2E1 decay rates also depend on the transition energy, which is altered because of the involvement of the nuclear excitation energy. The decay rates may also be modified by the change in the muon wavefunctions due to the finite size potential. We proceed with a general investigation of the M1 transition, and subsequently apply it to our decay scenario.

4.1 The Magnetic Dipole Transition

We will first develop the theory for a relativistic M1 transition, following the presentation in Landau and Lifschitz [7]. For simplicity, we will then calculate the transition for a pure $2s \to 1s$ transition and later look at the application to our scenario.

The EM interaction term between a Dirac fermion ψ and a photon is given by $e j^\mu_{fi} A_\mu$, where e is the electromagnetic charge, $j_{fi} \equiv \psi_f \boldsymbol{\alpha} \psi_i$ is the current, and A_μ is the photon wavefunction. Recall that the matrix element for the EM interaction between a Dirac fermion ψ with current $j_{fi} = \psi_f \boldsymbol{\alpha} \psi_i$ and a photon with wavefunction $A_\mu(\mathbf{r})$ is given by

$$\begin{aligned} V_{fi} &= e \int j^\mu_{fi}(\boldsymbol{r}) A^*_\mu(\boldsymbol{r}) d^3x \\ &= e \int d^3x \; j^\mu_{fi}(\boldsymbol{r}) \int \frac{d^3k}{(2\pi)^3} A^*_\mu(\boldsymbol{k}) e^{-i\boldsymbol{k}\cdot\boldsymbol{r}} \end{aligned} \tag{4.6}$$

We have omitted the subscripts (ωjm) from the photon wavefunction for simplicity. The wavefunction of a magnetic photon with angular momentum j and energy ω has the form $A^\mu = (0, \boldsymbol{A})$, with

$$\boldsymbol{A}_{\omega jm} = \frac{4\pi^2}{\omega^{3/2}} \delta(|\boldsymbol{k}| - \omega) \boldsymbol{Y}^{(m)*}_{jm}(\mathbf{n}_r) \tag{4.7}$$

Substituting this expression into the matrix element above gives

$$
\begin{aligned}
V_{fi} &= e\int d^3x\ \boldsymbol{j}_{fi}(\boldsymbol{r})\cdot\int\frac{k^2dkd\Omega_k}{(2\pi)^3}\frac{4\pi^2}{\omega^{3/2}}\delta(|\boldsymbol{k}|-\omega)\boldsymbol{Y}^{(m)*}_{jm}(\mathbf{n}_r)e^{-i\boldsymbol{k}\cdot\boldsymbol{r}}\\
&= -e\frac{\sqrt{\omega}}{2\pi}\int d^3x\ \boldsymbol{j}_{fi}(\boldsymbol{r})\cdot\int d\Omega_k\boldsymbol{Y}^{(m)*}_{jm}(\mathbf{n}_r)e^{-i\boldsymbol{k}\cdot\boldsymbol{r}}
\end{aligned}
\tag{4.8}
$$

The factor of $e^{-i\boldsymbol{k}\boldsymbol{r}}$ can be expanded in terms of spherical Bessel functions and the spherical harmonics by use of

$$
e^{-i\boldsymbol{\omega}\boldsymbol{r}} = 4\pi\sum_{l=0}^{\infty}\sum_{m=-l}^{l} i^{-l}g_l(\omega r)Y_{lm}(\mathbf{n}_k)Y^*_{lm}(\mathbf{n}_r) \tag{4.9}
$$

here $g_j(\rho)$ is the j-th order spherical Bessel function. Rayleigh's formula allows us to express the bessel function as

$$
g_l(\rho) = (-\rho)^l\left(\frac{1}{\rho}\frac{d}{d\rho}\right)^l\frac{sin\rho}{\rho} \tag{4.10}
$$

Writing the spherical harmonic vector in terms of its components and using the orthogonality properties results in

$$
\int d\Omega_k e^{-i\boldsymbol{k}\boldsymbol{r}}\boldsymbol{Y}^{(m)*}_{jm}(\mathbf{n}_r) = 4\pi i^{-j}g_j(\omega r)\boldsymbol{Y}^{(m)*}_{jm}(\mathbf{n}_r) \tag{4.11}
$$

Thus the matrix element becomes

$$
V_{fi} = -ei^{-j}2\sqrt{\omega}\int d^3x\ g_j(\omega r)\boldsymbol{j}_{fi}(\boldsymbol{r})\cdot\boldsymbol{Y}^{(m)*}_{jm}(\mathbf{n}_r) \tag{4.12}
$$

We now perform a Taylor expansion of the Bessel functions near the origin, and use the definition of the spherical harmonic vector corresponding to the magnetic photon

$$
g_l(\omega r) = \sum_{n=j}^{\infty}\frac{g^{(n)}_j(0)}{n!}(\omega r)^n \equiv \sum_{n=j}^{\infty}\beta_n r^n \tag{4.13}
$$

$$
\boldsymbol{Y}^{(m)*}_{jm}(\mathbf{n}_r) = \frac{1}{\sqrt{j(j+1)}}\boldsymbol{r}\times\nabla Y^*_{jm} \tag{4.14}
$$

Note that our sum begins with the $n=j$ term because this is the first non-zero term of the Taylor expansion of the Bessel functions of order j. This allows us to rewrite the matrix element as

$$
\begin{aligned}
V_{fi} &= -\frac{ei^{-j}2\sqrt{\omega}}{\sqrt{j(j+1)}}\int d^3x\ \sum_{n=j}^{\infty}\beta_n r^{n-j}r^j\boldsymbol{j}_{fi}(\boldsymbol{r})\cdot\boldsymbol{r}\times\nabla Y^*_{jm}\\
&= \frac{ei^{-j}2\sqrt{\omega}}{\sqrt{j(j+1)}}\int d^3x\ \sum_{n=j}^{\infty}\beta_n r^{n-j}\boldsymbol{r}\times\boldsymbol{j}_{fi}\cdot\nabla(r^jY^*_{jm})\\
&= ei^{-1}\sqrt{2\omega}\int d^3x\ \sum_{n=1}^{\infty}\beta_n r^{n-1}\boldsymbol{r}\times\boldsymbol{j}_{fi}\cdot\nabla(rY^*_{1m})
\end{aligned}
\tag{4.15}
$$

In the last line we have written the result for the $j=1$ case, corresponding to the magnetic dipole transition (M1), which is the form we will use later. The relation used in the second last line in the derivation above is best seen from writing the vectors in component form

$$
\begin{aligned}
-(\boldsymbol{r}\times\boldsymbol{j}_{fi})\cdot\nabla(r^jY^*_{jm}) &= -\varepsilon_{pqr}r_p(j_{fi})_q[\nabla(r^jY^*_{jm})]_r\\
&= (j_{fi})_q\varepsilon_{prq}r_p[\nabla(r^jY^*_{jm})]_r\\
&= (j_{fi})_q\varepsilon_{prq}r_pr^j[\nabla Y^*_{jm}]_r + (j_{fi})_q\varepsilon_{prq}r_p[\nabla r^j]_rY^*_{jm}\\
&= r^j(j_{fi})_q\varepsilon_{prq}r_p[\nabla Y^*_{jm}]_r\\
&= r^j\boldsymbol{j}_{fi}\cdot(\boldsymbol{r}\times\nabla Y^*_{jm})
\end{aligned}
\tag{4.16}
$$

The second term in the third line vanishes as it contains $\varepsilon_{prq}r_p[\nabla r^j]_r = \boldsymbol{r}\times\nabla r^j \propto \boldsymbol{r}\times\boldsymbol{r} = 0$.

The usefulness of splitting up $r^n = r^{n-j}r^j$ in the Taylor expansion now becomes clear in the $j=1$ case, as

$$
\sqrt{\frac{4\pi}{3}}rY_{10} = iz, \qquad \sqrt{\frac{4\pi}{3}}rY_{1\pm1} = \pm\frac{i}{\sqrt{2}}(x\pm iy) \tag{4.17}
$$

and hence the gradients appearing above are simply the spherical units vectors for $j = 1$. Thus the components of

$$\sqrt{\frac{3}{4\pi}} e i^{-1} \sqrt{2\omega} \int d^3x \sum_{n=1}^{\infty} \beta_n r^{n-1} \boldsymbol{r} \times \boldsymbol{j}_{fi} \tag{4.18}$$

are the spherical components of the vector

$$\boldsymbol{M}_{fi} = e i^{-1} \sqrt{\frac{3\omega}{2\pi}} \int d^3x \sum_{n=1}^{\infty} \beta_n r^{n-1} \boldsymbol{r} \times \boldsymbol{j}_{fi} \tag{4.19}$$

so that the decay rate is given by

$$\Gamma_{M1} = 2\pi |V_{fi}|^2 = 2\pi |\boldsymbol{M}_{fi}|^2 \tag{4.20}$$

We now turn to solutions of the Dirac equation, which will allow us to calculate $\boldsymbol{r} \times \boldsymbol{j}_{fi}$. Recall that the solutions to the Dirac equation for a particle in a spherically potential take the form

$$\psi = \begin{pmatrix} \phi \\ \chi \end{pmatrix} = \begin{pmatrix} f(r)\boldsymbol{\Omega}_{jlm} \\ (-1)^{\frac{1}{2}(1+l-l')} g(r) \boldsymbol{\Omega}_{jl'm} \end{pmatrix} \tag{4.21}$$

Here $\boldsymbol{\Omega}_{jlm}$ are the spherical harmonic spinors, defined in eq. 2.27. The quantum numbers l and l' are defined by $j = 1 \pm 1/2$ and $l' = 2j - l$ (j being the total angular momentum). The functions $f(r)$ and $g(r)$ are the large and small radial Dirac functions, given in eq. 2.28. We will make use of the non-relativistic limit of the Dirac functions is given by

$$f(r) \approx R(r), \qquad g(r) \approx \frac{R'}{2m} \tag{4.22}$$

where $R(r)$ is the non-relativistic wavefunction.

Finally, we will rewrite the second spinor via $(\boldsymbol{n}_r \cdot \boldsymbol{\sigma})\boldsymbol{\Omega}_{jlm} = i^{l'-1}\boldsymbol{\Omega}_{jl'm}$. We first focus on the form of the matrix element, and return later to evaluate the radial integral. As we are interested in the $2s \to 1s$ transition, we have $l = 0$ and $j = l + 1/2$. Using the above relation, the components of the spherical harmonic spinors reduce to $Y_{00} = 1/\sqrt{4\pi}$ (up to a phase), so we can write the initial and final spinors as

$$\begin{aligned} \psi_i &= \frac{1}{\sqrt{4\pi}} \begin{pmatrix} f_i(r) w_i \\ -i g_i(r) (\boldsymbol{n} \cdot \boldsymbol{\sigma}) w_i \end{pmatrix} \\ \psi_f &= \frac{1}{\sqrt{4\pi}} \begin{pmatrix} f_f(r) w_f \\ -i g_f(r) (\boldsymbol{n} \cdot \boldsymbol{\sigma}) w_f \end{pmatrix} \end{aligned} \tag{4.23}$$

here $w_i = w_i(m_i)$ and $w_f = w_f(m_f)$ are real unit spinors corresponding to the spin projection value m_i and m_j.

4.1.1 Computing the Matrix Element

Simplifying the Matrix Element

We first work on simplyfying $\mathbf{r} \times \boldsymbol{j}_{fi}$. Using our expressions for the Dirac wavefunctions, the EM current is

$$\begin{aligned} \boldsymbol{j}_{fi} &= \psi_f \boldsymbol{\alpha} \psi_i = \phi_f^\dagger \boldsymbol{\sigma} \chi_i + \chi_f^\dagger \boldsymbol{\sigma} \phi_i \\ &= \frac{1}{4\pi} \left[f_f(r) w_f^T \boldsymbol{\sigma} (-i) g_i(r) (\boldsymbol{n} \cdot \boldsymbol{\sigma}) w_i + (i) g_f(r) [(\boldsymbol{n} \cdot \boldsymbol{\sigma}) w_f]^\dagger \boldsymbol{\sigma} f_i(r) w_i \right] \\ &= \frac{1}{4\pi i} \left[f_f(r) g_i(r) w_f^T \boldsymbol{\sigma} (\boldsymbol{n} \cdot \boldsymbol{\sigma}) w_i - g_f(r) f_i(r) w_f^T (\boldsymbol{n} \cdot \boldsymbol{\sigma}) \boldsymbol{\sigma} w_i \right] \end{aligned} \tag{4.24}$$

We now need to compute $\boldsymbol{r} \times \boldsymbol{j}_{fi}$. We can simplify the result by working on the vector components, ignoring the radial functions, scalar factors, and spinors for now. The first term goes as

$$\begin{aligned} \boldsymbol{r} \times \boldsymbol{\sigma} (\boldsymbol{n} \cdot \boldsymbol{\sigma}) &= r \boldsymbol{n} \times \boldsymbol{\sigma} (\boldsymbol{n} \cdot \boldsymbol{\sigma}) \\ &= r \varepsilon_{ijk} n_j \sigma_k \sigma_p n_p \end{aligned} \tag{4.25}$$

Hence the matrix element (cf. 4.19) goes as

$$\begin{aligned}\int d\Omega\ \boldsymbol{r}\times\boldsymbol{\sigma}(\boldsymbol{n}\cdot\boldsymbol{\sigma}) &= r\varepsilon_{ijk}\sigma_k\sigma_p\int d\Omega\ n_j n_p \\ &= \frac{4\pi}{3}r\varepsilon_{ijk}\sigma_k\sigma_p\delta_{jp} \\ &= -\frac{4\pi}{3}r\varepsilon_{ikj}\sigma_k\sigma_j \\ &= -\frac{4\pi}{3}r\boldsymbol{\sigma}\times\boldsymbol{\sigma} \\ &= -\frac{8\pi i}{3}r\boldsymbol{\sigma}\end{aligned} \tag{4.26}$$

The final line follows from the identities $\sigma_a\sigma_b = \delta_{ab}I + i\varepsilon_{abc}\sigma_c$ and $\varepsilon_{abc}\varepsilon_{def} = 2\delta_{ad}$. The second term in the matrix element is nearly identical, except that there is no need to permute the indices of the levi-civita symbol in order to make the cross product apparent. Hence we arrive at the same result, with a negative sign,

$$\int d\Omega\ \boldsymbol{r}\times(\boldsymbol{n}\cdot\boldsymbol{\sigma})\boldsymbol{\sigma} = \frac{8\pi i}{3}r\boldsymbol{\sigma} \tag{4.27}$$

Putting this together gives

$$\boldsymbol{r}\times\boldsymbol{j}_{fi} = \frac{-2}{3}rw_f^T\boldsymbol{\sigma}w_i(f_i(r)g_f(r)+f_f(r)g_i(r)) \tag{4.28}$$

Now that we have computed $\boldsymbol{r}\times\boldsymbol{j}_{fi}$, we can return to our expression for the matrix element (Eq. 4.19)

$$\begin{aligned}\boldsymbol{M}_{fi} &= ei^{-1}\sqrt{\frac{3\omega}{2\pi}}\int d^3x\ \sum_{n=1}^{\infty}\beta_n r^{n-1}\boldsymbol{r}\times\boldsymbol{j}_{fi} \\ &= ei^{-1}\sqrt{\frac{3\omega}{2\pi}}\int dr\ r^2\sum_{n=1}^{\infty}\beta_n r^{n-1}\left(\frac{-2r}{3}w_f^T\boldsymbol{\sigma}w_i(f_i(r)g_f(r)+f_f(r)g_i(r))\right) \\ &= -ei^{-1}\sqrt{\frac{2\omega}{3\pi}}(w_f^T\boldsymbol{\sigma}w_i)\int dr\ r^2 g_1(\omega r)(f_i(r)g_f(r)+f_f(r)g_i(r))\end{aligned} \tag{4.29}$$

In the last line, we have recombined the factor of r arising from $\boldsymbol{r}\times\boldsymbol{j}_{fi}$ with the remaining powers of r and r^{n-1}, giving our original Bessel function. We can rewrite the integral as an inner product for clarity

$$\begin{aligned}\boldsymbol{M}_{fi} &= -ei^{-1}\omega^{3/2}\sqrt{\frac{2}{3\pi}}(w_f^T\boldsymbol{\sigma}w_i)\Big[\langle g_f|g_1(\omega r)/\omega|f_i\rangle + \langle f_f|g_1(\omega r)/\omega|g_i\rangle\Big] \\ &= -ei^{-1}\omega^{3/2}\sqrt{\frac{2}{3\pi}}(w_f^T\boldsymbol{\sigma}w_i)I_R\end{aligned} \tag{4.30}$$

where we have defined $I_R \equiv \langle g_f|g_1(\omega r)/\omega|f_i\rangle + \langle f_f|g_1(\omega r)/\omega|g_i\rangle$, which we will refer to as the radial integral. We have also introduced a factor of $1/\omega$ into the radial integral to match the traditional expression for the M1 rate. The decay rate is given by

$$\begin{aligned}\Gamma_{M1} &= 2\pi|\boldsymbol{M}_f i|^2 \\ &= 2\pi\frac{2\omega^3e^2}{3\pi}|I_R|^2|w_f^T\boldsymbol{\sigma}w_i|^2 \\ &= \frac{4\omega^3e^2}{3}|I_R|^2|w_f^T\boldsymbol{\sigma}w_i|^2\end{aligned} \tag{4.31}$$

Before calculating the radial integral, we turn to the spin dependent portion of the decay rate $|w_f^T\boldsymbol{\sigma}w_i|^2$. As the final spin state of the muon is free to be either up or down, and as we assume the initial state to be unpolarized, we average over initial states and sum over final states. If the final state is the same as the initial state, we get a contribution from the z-component of $\boldsymbol{\sigma}$, otherwise we get a contribution from both the x and y components. The result is

$$w_f^T\boldsymbol{\sigma}w_i = \begin{cases}(0,0,\pm1), & m_i = m_f \\ (1,\pm i,0), & m_i \neq m_f\end{cases} \tag{4.32}$$

The signs above depend on the spin of the initial state, but since we square and sum over final states it doesn't affect the final result. Squaring and summing gives a factor of 3, hence the decay rate becomes

$$\Gamma_{M1} = 4\omega^3 e^2 |I_R|^2 \tag{4.33}$$

This is the general form of the M1 decay rate, although the Radial integral is sometimes redefined with a factor of three, as is done in Landau and Lifshitz as well as Johnson (1972) [36]. The factor of three they include into the radial integral is to cancel a factor of one third appearing as the first coefficient in the Bessel function Taylor expansion.

We now turn to the evaluation of the radial Dirac functions and the radial integral, I_R. Recall the form of the Dirac radial wavefunction, given in chapter 2

$$\begin{aligned} f,g\ (r) = \frac{\pm(2\lambda)^{3/2}}{\Gamma(2\gamma+1)}\left[\frac{(m\pm E)\Gamma(2\gamma+n_r+1)}{4m(Z\alpha m/\lambda)(Z\alpha m/\lambda-\kappa)n_r!}\right]^{1/2}(2\lambda r)^{\gamma-1}e^{-\lambda r}\times \\ \left[(Z\alpha m/\lambda-\kappa)F(-n_r,2\gamma+1,2\lambda r)\mp n_r F(1-n_r,2\gamma+1,2\lambda r)\right] \end{aligned} \tag{4.34}$$

The initial state has $n_{r_i} = 1$, and the final state has $n_{r_f} = 0$. As both states are $l = 0$ states, $\kappa_i = \kappa_f = -1$, so that $\gamma_i = \gamma_f$, hence we relabel $\kappa = \kappa_i = \kappa_f$ and $\gamma = \gamma_i = \gamma_f$ for simplicity. We first look at the hypergeometric functions. With reference to Eq. 2.28, we see that both $f_i(r)$ and $g_i(r)$ contain $F(-n_{r_i}, 2\gamma+1, 2\lambda_i r)$. As $n_{r_i} = -1$, the series terminates after n = 1, giving $F(-1, 2\gamma+1, 2\lambda_i r) = 1 - 2\lambda_i r/(2\gamma+1)$. The second hypergeometric function reduces to $F(0, 2\gamma+1, 2\lambda_i r) = 1$. The final radial Dirac functions (for $n_{r_f} = 0$) also contain the same terms, with the substitutions $\lambda_i \to \lambda_f$.

In order to better appreciate the radial dependance of the wavefunctions, we will first define some notation to reduce the clutter of the constants. We define

$$\begin{aligned} \beta_{f_i} &= \frac{(2\lambda_i)^{\gamma+1/2}}{\Gamma(2\gamma+1)}\left[\frac{(m+E_i)\Gamma(2\gamma+n_r+1)}{4m(Z\alpha m/\lambda_i)(Z\alpha m/\lambda_i-\kappa)n_{r_i}!}\right]^{1/2} \\ \beta_{g_i} &= \frac{-(2\lambda_i)^{\gamma+1/2}}{\Gamma(2\gamma+1)}\left[\frac{(m-E_i)\Gamma(2\gamma+n_r+1)}{4m(Z\alpha m/\lambda_i)(Z\alpha m/\lambda_i-\kappa)n_{r_i}!}\right]^{1/2} \end{aligned} \tag{4.35}$$

so that the radial Dirac functions can be written as

$$\begin{aligned} f_i(r) &= \beta_{f_i} r^{\gamma-1} e^{-\lambda_i r}\left[\left(\frac{Z\alpha m}{\lambda_i}-\kappa\right)\left(1-\frac{2\lambda_i r}{2\gamma+1}\right)-1\right] \\ g_i(r) &= \beta_{g_i} r^{\gamma-1} e^{-\lambda_i r}\left[\left(\frac{Z\alpha m}{\lambda_i}-\kappa\right)\left(1-\frac{2\lambda_i r}{2\gamma+1}\right)+1\right] \end{aligned} \tag{4.36}$$

Analogous to the constants defined above in Eq. 4.35 for the initial wavefunctions, we can do the same for the final wavefunctions, replacing the initial parameters with the final parameters (e.g. $\lambda_i \to \lambda_f$) to find the radial Dirac functions of the final state

$$\begin{aligned} f_f(r) &= \beta_{f_f} r^{\gamma-1} e^{-\lambda_f r}\left(\frac{Z\alpha m}{\lambda_f}-\kappa\right) \\ g_f(r) &= \beta_{g_f} r^{\gamma-1} e^{-\lambda_f r}\left(\frac{Z\alpha m}{\lambda_f}-\kappa\right) \end{aligned} \tag{4.37}$$

The simplicity of the final state functions is due to $n_{r_f} = 0$, which causes the second term in the square brackets to vanish, and also the first hypergeometric function to be unity.

The First Term in the Bessel Expansion

Recall the matrix element involves the inner product with the operator $g_1(\omega r)/\omega$. Note that as ω is the photon energy, we have $\omega r \approx m(Z\alpha)^2 a_0 = Z\alpha < 1$. With reference to Eq. 4.10, we can approximate the Bessel function as

$$g_1(\omega r) = \frac{\sin(\omega r)}{(\omega r)^2} - \frac{\cos(\omega r)}{\omega r} \approx \frac{\omega r}{3} - \frac{(\omega r)^3}{30} \tag{4.38}$$

In this section, we will just retain the first term, but later we will be interested in evaluating the second one. Thus there are two terms we need to evaluate in the radial integral (cf. 4.30). Let

$$\begin{aligned} I_a &= \int dr\ \frac{1}{3} r^3 f_i(r) g_f(r) \\ I_b &= \int dr\ \frac{1}{3} r^3 f_f(r) g_i(r) \end{aligned} \tag{4.39}$$

We first study I_a

$$I_a = \frac{\beta_{f_i}\beta_{g_f}}{3}\left(\frac{Z\alpha m}{\lambda_f} - \kappa\right)\int dr\ r^3 r^{2\gamma-2} e^{-(\lambda_i+\lambda_f)r}\left[\left(\frac{Z\alpha m}{\lambda_i} - \kappa\right)\left(1 - \frac{2\lambda_i r}{2\gamma+1}\right) - 1\right] \tag{4.40}$$

Let $a = 2\gamma + 1,\ b = \lambda_i + \lambda_f,\ c = Z\alpha m/\lambda_i - \kappa,$ and $d = 2\lambda_i/(2\gamma+1)$, so that we can write

$$\begin{aligned} I_a &= \frac{\beta_{f_i}\beta_{g_f}}{3}\left(\frac{Z\alpha m}{\lambda_f} - \kappa\right)\int_0^\infty dr\ r^a e^{-br}[c(1-dr) - 1] \\ &= \frac{\beta_{f_i}\beta_{g_f}}{3}\left(\frac{Z\alpha m}{\lambda_f} - \kappa\right)\left[\frac{1}{b^{a+2}}[cd\Gamma(a+2, br) + b(1-c)\Gamma(a+1, br)]\right]_0^\infty \\ &= -\frac{\beta_{f_i}\beta_{g_f}}{3}\left(\frac{Z\alpha m}{\lambda_f} - \kappa\right)\frac{1}{b^{a+2}}\left(cd\Gamma(a+2) + b(1-c)\Gamma(a+1)\right) \end{aligned} \tag{4.41}$$

where $\Gamma(a,x) = \int_x^\infty t^{a-1}e^{-t}dt$ is the upper incomplete gamma function, satisfying the following relations

$$\begin{aligned} &\Gamma(a,0) = \Gamma(a), \quad (\mathrm{Re}(a) > 0) \\ &\lim_{x\to\infty}\Gamma(a,x) = 0 \end{aligned} \tag{4.42}$$

Having evaluated the radial integral, we can simplify the result

$$I_a = -\frac{\beta_{f_i}\beta_{g_f}}{3(\lambda_i+\lambda_f)^{2\gamma+3}}\left(\frac{Z\alpha m}{\lambda_f} - \kappa\right)\left[\left(\frac{Z\alpha m}{\lambda_i} - \kappa\right)\frac{2\lambda_i}{2\gamma+1}\Gamma(2\gamma+3) + (\lambda_i+\lambda_f)\left(1 - \frac{Z\alpha m}{\lambda_i} + \kappa\right)\Gamma(2\gamma+2)\right] \tag{4.43}$$

Its important to note that the β parameters have dimension $\mathrm{eV}^{2\gamma+1}$, so that the radial integral has dimension eV^{-1}. Given that the only other dimensional parameter in the decay rate is the transition energy, ω[3], we see the dimension of the decay rate is indeed eV (or s^{-1} in SI units) as expected.

We now turn to the second integral

$$I_b = \int dr\ \frac{1}{3} r^3 f_f(r) g_i(r) = \frac{\beta_{g_i}\beta_{f_f}}{3}\left(\frac{Z\alpha m}{\lambda_f} - \kappa\right)\int dr\ r^3 r^{2\gamma-2} e^{-(\lambda_i+\lambda_f)r}\left[\left(\frac{Z\alpha m}{\lambda_i} - \kappa\right)\left(1 - \frac{2\lambda_i r}{2\gamma+1}\right) + 1\right] \tag{4.44}$$

Comparing I_b to our expression for I_a, we see the only diffference in the radial integrand is the $+1$ instead of -1 in the last factor. The computation is very similar, with some sign differences in the last term in the final line. The only difference from the β constants is the appearance of $(m - E_i)(m + E_f)$ instead of $(m + E_i)(m - E_f)$. Making these replacements gives the second integral as

$$I_b = -\frac{\beta_{g_i}\beta_{f_f}}{3(\lambda_i+\lambda_f)^{2\gamma+3}}\left(\frac{Z\alpha m}{\lambda_f} - \kappa\right)\left[\left(\frac{Z\alpha m}{\lambda_i} - \kappa\right)\frac{2\lambda_i}{2\gamma+1}\Gamma(2\gamma+3) - (\lambda_i+\lambda_f)\left(1 + \frac{Z\alpha m}{\lambda_i} - \kappa\right)\Gamma(2\gamma+2)\right] \tag{4.45}$$

The radial integral is thus approximated by the integral $I_1 \equiv I_a + I_b$. Using the definitions appearing in Eq. 2.29, as well as the results of Eqs. 4.43 and 4.45, one can compute the radial integral I_1. Before we compute this, it is worthwhile to study the second term in the Bessel expansion as well.

The Second Term in the Bessel Expansion

As discussed above, our previous expression only took into account the first non-zero term of the Bessel expansion. Before evaluating the second term, it will prove useful to study the structure of the first term to understand any cancellations that appear. Recall that the Bessel function can be written as

$$g_1(\rho) = \frac{\sin(\omega r)}{(\omega r)^2} - \frac{\cos(\omega r)}{\omega r} \approx \frac{\omega r}{3} - \frac{(\omega r)^3}{30} \tag{4.46}$$

In the non-relativistic limit, we have

$$f(r) \approx R(r), \qquad g(r) \approx \frac{R'(r)}{2m}, \qquad g_1(\omega r)/\omega \approx \frac{r}{3} \tag{4.47}$$

In the previous section, we computed the matrix element using the full radial Dirac functions, but only the first term of the Bessel function. Normally, we would expect the second term to be much smaller than the first by a factor of $(Z\alpha)^2$, but there is relativistic suppression in the first term that arises due to orthogonality of the non-relativistic radial wavefunctions. To see this, suppose the the non-relativistic wavefunctions were used together with the lowest order Bessel expansion. Using integration by parts, we see that the first term of the radial integral would be proportional to

$$\begin{aligned}
\left\langle \frac{R'_f}{2m} \middle| r \middle| R_i \right\rangle &= \int dr\ r^3 \frac{R'_f(r)}{2m} R_i(r) \\
&= \cancelto{0}{\left[r^3 \frac{R_f(r)}{2m} \right]_0^\infty} - 3 \int dr\ r^2 \frac{R_f(r)}{2m} R_i(r) - \int dr\ r^3 \frac{R_f(r)}{2m} R'_i(r) \\
&= -\cancelto{0}{\left\langle R_f \middle| R_i \right\rangle} - \left\langle R_f \middle| r \middle| \frac{R'_i}{2m} \right\rangle
\end{aligned} \tag{4.48}$$

In the last line, the first term is zero because the radial wavefunctions are orthogonal as $R_f = R_{10}$ and $R_i = R_{20}$. We immediately see the radial integral for the transition vanishes

$$\left\langle \frac{R'_f}{2m} \middle| r \middle| R_i \right\rangle + \left\langle R_f \middle| r \middle| \frac{R'_i}{2m} \right\rangle = -\left\langle R_f \middle| r \middle| \frac{R'_i}{2m} \right\rangle + \left\langle R_f \middle| r \middle| \frac{R'_i}{2m} \right\rangle = 0 \tag{4.49}$$

Hence the first term in the Bessel expansion is suppressed by relativistic corrections to the radial wavefunctions (i.e. higher powers of $Z\alpha$). Conversely, the second term contains the operator r^3 instead of r, so that the integral (denoted I_2), after integration by parts in a similar manner (see below), becomes proportional to $\langle R_f | r^2 | R_i \rangle$ which is non zero. Importantly, this term is non-vanishing even when the non-relativistic wavefunctions are used. It is not suppressed by relativistic corrections to the radial function, instead it is suppressed by the additional factor of $(\omega r)^2$ in the Bessel expansion. Hence we cannot ignore the second term in the Bessel expansion by a power counting argument, we must also evaluate this term to understand the strengths of the different suppressions.

We now seek to evaluate the contribution from the second term in the Bessel function expansion, using the non-relativistic expansion of the Dirac functions above.

Using the approximate Dirac functions and substituting the second term into the matrix element above yields

$$I_2 = \left[\left\langle \frac{R'_f}{2m} \middle| - \frac{\omega^2 r^3}{30} \middle| R_i \right\rangle + \left\langle R_f(r) \middle| - \frac{\omega^2 r^3}{30} \middle| \frac{R'_i}{2m} \right\rangle \right] \tag{4.50}$$

Integrating the first term by parts gives

$$\begin{aligned}
\left\langle \frac{R'_f}{2m} \middle| - \frac{\omega^2 r^3}{30} \middle| R_i \right\rangle &= -\frac{\omega^2}{30} \int dr\ r^5 \frac{R'_f(r)}{2m} R_i(r) \\
&= -\frac{\omega^2}{30} \cancelto{0}{\left[r^5 \frac{R_f(r)}{2m} \right]_0^\infty} + \frac{\omega^2}{6} \int dr\ r^4 \frac{R_f(r)}{2m} R_i(r) + \frac{\omega^2}{30} \int dr\ r^5 \frac{R_f(r)}{2m} R'_i(r) \\
&= \left\langle R_f \middle| \frac{\omega^2 r^2}{12m} \middle| R_i \right\rangle + \left\langle R_f \middle| - \frac{\omega^2 r^3}{30} \middle| \frac{R'_i}{2m} \right\rangle
\end{aligned} \tag{4.51}$$

Importantly, the second non-zero term appearing from integration by parts cancels with the second term in the matrix element. The correction to matrix element reduces to one term

$$I_2 = \frac{\omega^2}{12m} \langle R_f | r^2 | R_i \rangle \tag{4.52}$$

Putting both terms together yields the decay rate as

$$\Gamma_{M1} = 4\alpha\omega^3 |I_1 + I_2|^2 \tag{4.53}$$

4.1.2 The Muonic Zirconium Transition

The result derived above will be modified in our case as discussed earlier. The initial and final perturbed wavefunctions are given by

$$\begin{aligned}\psi_i &\approx |100\rangle|1\rangle + \epsilon_{i,1s}|100\rangle|0\rangle + \epsilon_{i,2s}|200\rangle|0\rangle \\ \psi_f &\approx |100\rangle|1\rangle + \epsilon_{f,1s}|100\rangle|0\rangle + \epsilon_{f,2s}|200\rangle|0\rangle\end{aligned} \tag{4.54}$$

In order to include this mixing in our M1 transition expression above, the matrix element is modified as

$$\begin{aligned}\langle 100|\hat{M}|200\rangle \rightarrow &\left(\langle 0|\langle 100| + \epsilon_{f,1s}\langle 1|\langle 100| + \epsilon_{f,2s}\langle 1|\langle 200|\right)\hat{M}\left(|100\rangle|1\rangle + \epsilon_{i,1s}|100\rangle|0\rangle + \epsilon_{i,2s}|200\rangle|0\rangle\right) \\ &= \epsilon_{f,2s}\langle 1|\langle 200|\hat{M}|100\rangle|1\rangle + \epsilon_{i,2s}\langle 0|\langle 100|\hat{M}|200\rangle|0\rangle \\ &= (\epsilon_{f,2s} + \epsilon_{i,2s})\langle 100|\hat{M}|200\rangle\end{aligned} \tag{4.55}$$

Here the operator $\hat{M}$ represents the operator repsonsible for the M1 transition. Although the calculation above is written using notation from the Schrödinger bound states, the same result holds for the Dirac bound states we used above (as the perturbation is spherically symmetric). Hence the modification to the decay rate is simply a multiplication by $|\epsilon_{f,2s} + \epsilon_{i,2s}|^2$. Thus the decay rate of the relevant muonic zirconium M1 transition is given by

$$\Gamma_{M1} = 4\omega^3\alpha|I_1 + I_2|^2|\epsilon_{i,2s} + \epsilon_{f,2s}|^2 \tag{4.56}$$

4.1.3 Calculating the Decay Rate

To determine the transition energy ω as well as the energy values found in ϵ_{2s} and $\epsilon_{f,2s}$, we use the energies found from numerical solutions to the Schrödinger equation. Although it may seem inconsistent to use the Schrödinger energies with the Dirac wavefunctions, the energies found from the numerical solutions are much more accurate than the analytic Dirac energies. The Dirac energies will be used everywhere else (e.g. in the Dirac wavefunctions to compute the radial integral), and the difference between the perturbed Schrödinger energies and the Dirac energies are small (see table 3.1). The biggest approximation is the use of the pointlike Dirac wavefunctions in the radial integral I_1. Since we obtained the wavefunctions via the Schrödinger equation, our numerical wavefunctions cannot be applied here as the matrix element vanishes when non-relativistic wavefunctions are used. Therefore we must use the pointlike Dirac wavefunctions. Our numerical Schrödinger solutions are used in computing the radial integral I_2, cf. Eq. 4.52. The relevant Schrödinger energies are given below in table 4.1.

Table 4.1: Numerical energies for the M1 transition

Quantum Number n (State: $\|n00\rangle\|0\rangle$)	Numerical Energy (keV)
1	-3598.4
2	-1000.6
E_{Nuc}	1760.7

The transition energy ω is determined from the unperturbed energies between the $|100\rangle|1\rangle$ state and the $|100\rangle|0\rangle$ state, which is just the difference in energy between the nuclear excited state and nuclear ground state, $E_{Nuc} = 1760.7$keV. The mixing part of the decay rate is given by

$$\begin{aligned}|\epsilon_{f,2s} + \epsilon_{i,2s}|^2 &= \left|\frac{B \times \langle 200|N_{Nuc}(r)|100\rangle}{E_1 - E_{Nuc} - E_2} + \frac{B \times \langle 200|N_{Nuc}(r)|100\rangle}{E_1 + E_{Nuc} - E_2}\right|^2 \\ &= |B|^2 \times |\langle 200|N_{Nuc}(r)|100\rangle|^2\left(\frac{1}{E_1 - E_{Nuc} - E_2} + \frac{1}{E_1 + E_{Nuc} - E_2}\right)^2\end{aligned} \tag{4.57}$$

Using our previous results for B and $\langle 200|N_{Nuc}(r)|100\rangle$, we find that

$$|\epsilon_{f,2s} + \epsilon_{i,2s}|^2 = 1.67 \times 10^{-7} \tag{4.58}$$

The last thing we need is to compute the radial integral I. The parameters as well as final result are given below in table 4.2. Note that the first section of the table gives the parameters relevant to the Dirac wavefunctions,

Table 4.2: Numerical Values for Radial Integral

Quantity	Initial State Value	Final State Value
κ	-1	
γ	0.9564	
n_r	1	0
E	1.0450×10^5keV	1.0105×10^5keV
λ	1.5595×10^4keV	3.0849×10^4keV
Radial Integral, I_1	$8.6012 \times 10^{-8}\text{keV}^{-1}$	
Radial Integral, I_2	$-1.0935 \times 10^{-8}\text{keV}^{-1}$	
Radial Integral, I	$7.5077 \times 10^{-8}\text{keV}^{-1}$	

only used in the integral I_1. In particular the energies include the rest mass of the muon, in contrast to the Schrödinger energies.

We see that the second non-zero term in the Bessel function expansion is comparable to the first term. Combining all of our previous results, the M1 transition is

$$\begin{aligned}\Gamma_{M1} &= 4\alpha\omega^3|I_1 + I_2|^2|\epsilon_{f,2s} + \epsilon_{i,2s}|^2 \\ &= \frac{4(1760.71\text{keV})^3}{137}(7.5077 \times 10^{-8}\text{keV}^{-1})^2(1.67 \times 10^{-7}) \\ &= 1.48 \times 10^{-13}\text{keV}\end{aligned} \tag{4.59}$$

Converting this via $\hbar = 6.582 \times 10^{-16}$eV·s gives the decay rate as

$$\Gamma_{M1} = 2.28 \times 10^5\text{s}^{-1} \tag{4.60}$$

Once we have also calculated the rate of the two photon transition, we shall compare the muonic nuclear de-excitation methods to the electronic nuclear de-excitation method (the E0 transition).

4.2 The Two Photon Transition

Recall that photon transitions arise from the modification of the momentum $\boldsymbol{p} \to \boldsymbol{p} + e\boldsymbol{A}$ [4], so that the Schrödinger equation contains a term proportional to $(\boldsymbol{p} + e\boldsymbol{A})^2$. In order to incorporate two photons, we can either include a term of the form $(e\boldsymbol{A})^2$ from the expansion $(\boldsymbol{p} + e\boldsymbol{A})^2$ or we could include 2 terms of the form $e\boldsymbol{p}\cdot\boldsymbol{A}$. The $(e\boldsymbol{A})^2$ term cannot yield this decay in non-relativistic QM (with the approximation $e^{i\boldsymbol{k}\cdot\boldsymbol{r}} = 1$), as we will end up with the inner product $\langle R_{1s}|R_{2s}\rangle = 0$. In principle, we could use the Dirac functions to get a non-zero result, or expand the photon wavefunction to higher order in ωr as done in the M1 transition. However as in the M1 transition, both approaches will be suppressed by extra factors of $Z\alpha$. Conversely the approach of using two factors of $e\boldsymbol{p}\cdot\boldsymbol{A}$ can yield a non-zero result with the non-relativistic wavefunctions and with the lowest order expansion of the photon wavefunction. Thus we will work with the perturbation $e\boldsymbol{p}\cdot\boldsymbol{A}$. As each photon carries a unit of angular momentum, it is obvious that we need a second order perturbative approach, as the first order approximation will yield a vanishing decay rate. The transition can occur via the Feynman diagrams depicted in figure 4.2 below.

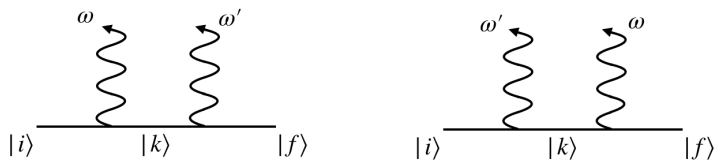

Figure 4.2: Feynman diagrams for the 2E1 matrix element. ω and ω' represent the energies of the two emitted photons.

The middle line in both diagrams represents an arbitrary virtual atomic state, and to compute the matrix element we must sum over all possible states (both bound states and continuum states), as expected from our

discussion of second order perturbation theory above. Following Fermi's golden rule, the differential transition probability is given by

$$d\Gamma = 2\pi |V_{21}|^2 \frac{d^3k}{(2\pi)^3}\frac{d^3k'}{(2\pi)^3}\delta(E_f + \omega + \omega' - E_i) \tag{4.61}$$

The two phase space factors correspond to the photons with wave vectors $\boldsymbol{k}$ and $\boldsymbol{k}'$. Applying second order perturbation theory to the two diagrams above yields the matrix element

$$V_{21} = \left(\sum_{k'} \frac{V'_{2k}V_{k1}}{E_i - E_k - \omega} + \int \frac{V'_{2\nu}V_{\nu 1}}{E_i - E_\nu - \omega}d\nu\right) + \left(\sum_{k'} \frac{V_{2k}V'_{k1}}{E_i - E_k - \omega'} + \int \frac{V_{2\nu}V'_{\nu 1}}{E_i - E_\nu - \omega'}d\nu\right) \tag{4.62}$$

In the first parenthesis (corresponding to the first diagram above) the first terms involves summing over all intermediate atomic bound states (except for $k = 2s$), whereas the second term involves the integral over all the continuum atomic states. The second set of parenthesis in the matrix element is the term from the second diagram above, where the photon with energy ω' is emitted second. The primes on the matrix element indicate the interaction occurs with the photon with energy ω'. Conservation of energy dictates that the energies of the two photon must sum to the total transition energy $\omega + \omega' = \omega_0$, where $\omega_0 \equiv E_{2s} - E_{1s}$ is the total energy available from the transition. In the following we will suppress the continuum expressions, and work with the sums for simplicity, although the same derivations will apply to both terms.

Each individual interaction involves a photon and two atomic states, the most dominant being the dipole interaction since the virtual intermediate states are arbitrary. Hence we approximate the potential by the dipole interaction potential

$$V = -\boldsymbol{d}\cdot\boldsymbol{E} = \boldsymbol{d}\cdot\dot{\boldsymbol{A}} \tag{4.63}$$

Both photon energies are bounded above by the total transition energy, and hence their wavelengths are bounded below by the wavelength corresponding to the transition energy. As before, the wavelength of the transition energy is larger than the scale of the system by $1/(Z\alpha) > 1$. Hence we can approximate the plane wave in the photon wavefunction as unity $e^{-i\boldsymbol{k}\cdot\boldsymbol{r}} \approx 1$. Thus the photon wavefunctions are (in the three dimensionally transverse gauge)

$$\boldsymbol{A}_{e,\omega} = \sqrt{4\pi}\frac{\boldsymbol{e}^*}{\sqrt{2\omega}}e^{-i\omega t}, \qquad \boldsymbol{A}'_{e',\omega'} = \sqrt{4\pi}\frac{\boldsymbol{e}'^*}{\sqrt{2\omega'}}e^{-i\omega' t} \tag{4.64}$$

and the dipole interactions takes the form

$$V_{2k} = i\sqrt{2\pi\omega}(\boldsymbol{e}^*\cdot\boldsymbol{d}_{2k}), \qquad V'_{k1} = i\sqrt{2\pi\omega}(\boldsymbol{e}'^*\cdot\boldsymbol{d}_{k1}) \tag{4.65}$$

Substituting Eqs. 4.62 and 4.65 into the differential decay rate gives

$$\begin{aligned} d\Gamma &= 2\pi\left|2\pi\sqrt{\omega\omega'}\left(\sum_{k'}\frac{(\boldsymbol{e}'^*\cdot\boldsymbol{d}_{2k})(\boldsymbol{e}^*\cdot\boldsymbol{d}_{k1})}{E_i - E_k - \omega} + \sum_{k'}\frac{(\boldsymbol{e}^*\cdot\boldsymbol{d}_{2k})(\boldsymbol{e}'^*\cdot\boldsymbol{d}_{k1})}{E_i - E_k - \omega'}\right)\right|^2 \frac{d^3k}{(2\pi)^3}\frac{d^3k'}{(2\pi)^3}\delta(E_f + \omega + \omega' - E_i) \\ &= \frac{\omega^3\omega'^3}{(2\pi)^3}\left|\left(\sum_{k'}\frac{(\boldsymbol{e}'^*\cdot\boldsymbol{d}_{2k})(\boldsymbol{e}^*\cdot\boldsymbol{d}_{k1})}{E_i - E_k - \omega} + \sum_{k'}\frac{(\boldsymbol{e}^*\cdot\boldsymbol{d}_{2k})(\boldsymbol{e}'^*\cdot\boldsymbol{d}_{k1})}{E_i - E_k - \omega'}\right)\right|^2 d\omega d\omega' d\Omega_\omega d\Omega_{\omega'}\delta(E_f + \omega + \omega' - E_i) \\ &= \frac{\omega^3(\omega_0 - \omega)^3}{(2\pi)^3}\left|\left(\sum_{k'}\frac{(\boldsymbol{e}'^*\cdot\boldsymbol{d}_{2k})(\boldsymbol{e}^*\cdot\boldsymbol{d}_{k1})}{E_i - E_k - \omega} + \sum_{k'}\frac{(\boldsymbol{e}^*\cdot\boldsymbol{d}_{2k})(\boldsymbol{e}'^*\cdot\boldsymbol{d}_{k1})}{E_i - E_k - (\omega_0 - \omega)}\right)\right|^2 d\omega d\Omega_\omega d\Omega_{\omega'} \end{aligned} \tag{4.66}$$

In the last line we have integrated over ω', effectively setting $\omega' = \omega_0 - \omega$. In a similar manner to the E1 transition, we can simplify the result by summing over photon polarizations and integrating over photon directions. For simplicity, define

$$(D_{21})_{pq} \equiv \sum_{k'}\frac{(d_{2k})_p(d_{k1})_q}{E_i - E_k - \omega} + \sum_{k'}\frac{(d_{2k})_q(d_{k1})_p}{E_i - E_k - (\omega_0 - \omega)} \tag{4.67}$$

where $p, q = 1, 2, 3$ label the cartesian coordinate components of the dipole vectors. This allows us to write the transition rate in a much more convenient manner

$$d\Gamma = \frac{\omega^3(\omega_0 - \omega)^3}{(2\pi)^3}|e^*_p e'^*_q (D_{21})_{pq}|^2 d\omega d\Omega_\omega d\Omega_{\omega'} \tag{4.68}$$

Summing over the photon polarisations and evaluating the square yields

$$\sum_{Polarizations} |e_p^* e_q'^* (D_{21})_{pq}|^2 = \sum_{Pol.} e_p^* e_q'^* e_r e_s' (D_{21})_{pq} (D_{21})_{rs}^* \\ = (\delta_{pr} - n_p n_r)(\delta_{qs} - n_q' n_s')(D_{21})_{pq}(D_{21})_{rs}^* \tag{4.69}$$

Integrating over the photon directions $d\Omega_\omega d\Omega_{\omega'}$ via use of

$$\int (\delta_{ij} - n_i n_j) d\Omega = 4\pi\delta_{ij} - \frac{4\pi}{3}\delta_{ij} = \frac{8\pi}{3}\delta_{ij} \tag{4.70}$$

allows us to write

$$\int d\Omega_\omega d\Omega_{\omega'} \sum_{Polarizations} |e_p^* e_q'^* (D_{21})_{pq}|^2 = \left(\frac{8\pi}{3}\right)^2 \delta_{pr}\delta_{qs}(D_{21})_{pq}(D_{21})_{rs}^* \\ = \left(\frac{8\pi}{3}\right)^2 (D_{21})_{pq}(D_{21})_{pq}^* \tag{4.71}$$

Hence the transition rate is

$$d\Gamma = \frac{8\omega^3(\omega_0 - \omega)^3\alpha^2}{9\pi}(D_{21})_{pq}(D_{21})_{pq}^* d\omega \tag{4.72}$$

In order to simplify the expression, define the z-axis to be aligned with the particle (where the nucleus is at the origin). Thus the dipole operator is just $\boldsymbol{d} = e(0, 0, z)$. We can bring out the resulting factors of e, giving an overall factor of α^2. We are left with matrix elements of the form $\langle\psi_{js}|z|\psi_k\rangle = \langle\psi_{js}|z|\psi_{nlm}\rangle$, where $j = 1, 2$, and we have replaced the sum over all states labeled by k to the usual labeling (of bound states) by nlm. We can again simplify by considering the angular integral, with the use of $z = \sqrt{4\pi/3}rY_{10}$, so that

$$\langle\psi_{js}|z|\psi_{nlm}\rangle = \sqrt{\frac{4\pi}{3}}\langle R_{js}|r|R_{nl}\rangle \int d\Omega Y_{00}Y_{10}Y_{lm} \\ = \frac{1}{\sqrt{3}}\langle R_{js}|r|R_{nl}\rangle \int d\Omega Y_{10}Y_{lm} \\ = \frac{1}{\sqrt{3}}\langle R_{js}|r|R_{n1}\rangle \delta_{1l}\delta_{m0} \tag{4.73}$$

The idea is essentially the same as the E1 transition, where we discover the angular selection rules for electric dipole transitions. The computation goes through in a very similar manner for the continuum spectrum, although the radial wavefunctions are indexed by the momentum instead of quantum number n. When we sum over all possible intermediate states, the angular selections rules imply that only the $|n10\rangle$ states will give a contribution. Hence the transition rate can be written as

$$d\Gamma(\omega) = \frac{8\omega^3(\omega_0 - \omega)^3\alpha^2}{27\pi}|F_{2s,1s}(\omega) + F_{2s,1s}(\omega_0 - \omega)|^2 d\omega \tag{4.74}$$

where

$$F_{2s,1s}(\omega) = \sum_{n=2}^{\infty} \frac{\langle R_{1s}|r|R_{n1}\rangle\langle R_{n1}|r|R_{2s}\rangle}{E_n - E_2 + \omega} + \int \frac{\langle R_{1s}|r|R_{q1}\rangle\langle R_{q1}|r|R_{2s}\rangle}{E_q - E_2 + \omega} dq \tag{4.75}$$

In this last expression, we have re-introduced the continuum states, characterized by the momentum $q = \sqrt{2mE}$. Although the final appearance of the continuum contribution is similar to the discrete case, there are some differences, which we shall quickly highlight. As per the E0 transition, we can expand the continuum states as

$$\psi_q = \frac{4\pi}{2q}\sum_{l=0}^{\infty}\sum_{m=-l}^{l} i^l e^{i\delta_l} R_{ql}(r) Y_{lm}^*(\mathbf{q}/q) Y_{lm}^*(\mathbf{r}/r) \\ \psi_q|_{l=1,m=0} = \frac{4\pi}{2q} i e^{i\delta_1} R_{ql}(r) Y_{10}^*(\mathbf{k}/k) Y_{10}^*(\mathbf{r}/r) \tag{4.76}$$

where $R_{ql}(r)$ are the positive energy radial Coulomb wavefunctions [6], normalized on the $2\pi/q$ scale so that $\langle R_{ql}|R_{q'l}\rangle = 2\pi\delta(q - q')$. The parameter δ_l is the phase shift due to the Coulomb potential. The overall phase $ie^{i\delta_l}$ will cancel out due to contribution from the two matrix elements, one of which will give the phase shift, and

the other its complex conjugate. In the second line we have take only the terms with orbital angular momentum $l = 1$ and z component $m = 0$, as per the selection rule above. Since we are dealing with a continuum state, we need to integrate over all momenta $\mathbf{q}$. The contribution from the continuum states is thus

$$\begin{aligned}
&\int \frac{d^3q}{(2\pi)^3} \frac{\langle R_{1s}|r|R_{q1}\rangle\langle R_{q1}|r|R_{2s}\rangle}{E_q - E_2 + \omega} \frac{(4\pi)^2}{4q^2} |Y_{10}(\mathbf{q}/q)|^2 \\
&= \int \frac{q^2 dq d\Omega_q}{8\pi^3} \frac{16\pi^2}{4q^2} |Y_{10}(\mathbf{q}/q)|^2 \frac{\langle R_{1s}|r|R_{x1}\rangle\langle R_{x1}|r|R_{2s}\rangle}{E_q - E_2 + \omega} \\
&= \frac{1}{2\pi} \int \frac{\langle R_{1s}|r|R_{q1}\rangle\langle R_{q1}|r|R_{2s}\rangle}{E_q - E_2 + \omega} dq
\end{aligned} \tag{4.77}$$

Thus if we instead define the positive energy solutions R_{q1} with an extra factor of $1/\sqrt{2\pi}$, they take the same form as the discrete sum. This change corresponds to the normalization condition $\langle R_{ql}|R_{q'l}\rangle = \delta(q - q')$.

Proceeding with the calculation, it is convenient to choose units of distance such that $a_Z = 1$ as it allows us to apply some of our intermediate steps from the hydrogen-like transition (with an electron) to the muonic transition. It also allows us to develop some intution on significant effects in both cases. Note that the transition energies and momenta are now measured in units of the inverse Bohr radius. In the case of the hydrogen decay, this implies the energy of both photon is $\omega_0 = 3/8Z\alpha$. The bound-bound inner products have a simple closed form for any p-wave state [29] (appendix A.1)

$$\begin{aligned}
\langle R_{1s}|r|R_{n1}\rangle &= 2^4 n^{7/2} \frac{(n-1)^{n-5/2}}{(n+1)^{(n+5/2)}} \\
\langle R_{n1}|r|R_{2s}\rangle &= 2^{17/2} n^{7/2} (n^2-1)^{1/2} \frac{(n-2)^{n-3}}{(n+2)^{(n+3)}}, \quad (n \neq 2) \\
\langle R_{nl}|r|R_{nl-1}\rangle &= -\frac{3}{2} n \sqrt{n^2 - l^2}
\end{aligned} \tag{4.78}$$

Analytic expressions for the continuum inner products are given in appendix A.2. Note that the inner products below are evaluated for the positive energy solutions including the factor of $1/\sqrt{2\pi}$ as discussed above.

$$\begin{aligned}
\langle R_{1s}|r|R_{q1}\rangle &= 2^4 \frac{q^{1/2}}{(1+q^2)^{3/2}} \frac{e^{-2\mathrm{arctan}(q)/q}}{\sqrt{1 - e^{-2\pi/q}}} \\
\langle R_{q1}|r|R_{2s}\rangle &= 2^{17/2} \frac{q^{1/2}(1+q^2)^{1/2}}{(1+4q^2)^3} \frac{e^{-2\mathrm{arctan}(2q)/q}}{\sqrt{1 - e^{-2\pi/q}}}
\end{aligned} \tag{4.79}$$

In contrast to the one-photon decays we previously studied, the photons in a two-photon decay are not mono-energetic, the only constraint being the sum of their energies is the transition energy. In order to find the total decay rate, we must integrate the differential cross section over the range of possible photon energies, with a factor of 1/2 to avoid double counting the photons.

$$\Gamma_{2E1} = \frac{1}{2} \int_0^{\omega_0} d\Gamma(\omega) = \frac{4}{27\pi} \int_0^{\omega_0} \omega^3 (\omega_0 - \omega)^3 \alpha^2 |F_{2s,1s}(\omega) + F_{2s,1s}(\omega_0 - \omega)|^2 d\omega \tag{4.80}$$

To evaluate the resulting integral, it is convenient to perform a change of variable of the form $y = \omega/\omega_0 = \omega/(3/8Z\alpha)$. The variable y is the fractional energy carried off by one of the photons, which allows us to write the integral in a cleaner form. Under this change of variables we have

$$\begin{aligned}
dy &= \frac{d\omega}{\omega_0} \\
\Rightarrow d\omega &= \omega_0 dy \\
\omega^3(\omega_0 - \omega)^3 &= \omega_0^6 y^3 (1-y)^3
\end{aligned} \tag{4.81}$$

We also bring a factor of ω out of the energies in the denominator, writing

$$\begin{aligned}
E_n - E_2 + \omega &= -\frac{1}{2n^2} Z\alpha + \frac{1}{8} Z\alpha + \omega \\
&= \omega \left[\frac{4}{3} \left(\frac{1}{4} - \frac{1}{n^2} \right) + y \right]
\end{aligned} \tag{4.82}$$

for the bound state sum, and (using $a_Z = 1$)

$$\begin{aligned} E_q - E_2 + \omega &= \frac{q^2}{2m} mZ\alpha + \frac{1}{8}Z\alpha + \omega \\ &= \omega_0 \left(\frac{4q^2}{3} + \frac{1}{3} + y \right) \end{aligned} \tag{4.83}$$

for the continuous state integral. Making these substitutions and collecting the powers of ω_0 outside the integral allows us to write the decay rate as

$$\Gamma_{2E1} = \frac{4}{27\pi}\omega_0^5 \alpha^2 \int_0^1 y^3(1-y)^3 |G_{2s,1s}(y) + G_{2s,1s}(1-y)|^2 dy \tag{4.84}$$

where $G_{2s,1s}$ is just the dimensionless analogue of $F_{2s,1s}$

$$G_{2s,1s}(y) = \sum_{n=2}^{\infty} \frac{\langle R_{1s}|r|R_{n1}\rangle\langle R_{n1}|r|R_{2s}\rangle}{\frac{4}{3}(\frac{1}{4} - \frac{1}{n^2}) + y} + \int_0^{\infty} \frac{\langle R_{1s}|r|R_{q1}\rangle\langle R_{q1}|r|R_{2s}\rangle}{\frac{4q^2}{3} + \frac{1}{3} + y} dq \tag{4.85}$$

In order to restore natural units, we must multiply by a_Z^4, and also use $\omega_0 = 3/8m(Z\alpha)^2$. With these changes in mind, the transition rate in natural units is given by

$$\Gamma_{2E1} = \frac{4}{27\pi}\omega_0^5 \alpha^2 a_Z^4 \int_0^1 y^3(1-y)^3 |G_{2s,1s}(y) + G_{2s,1s}(1-y)|^2 dy \tag{4.86}$$

As we have pulled out all relevant parameters from the remaining integral, we see that the two-photon 2E1 transition scales as

$$\Gamma_{2E1} \sim \omega_0^5 \alpha^2 a_Z^4 \sim m^5 (Z\alpha)^{10} \alpha^2 \frac{1}{m^4 (Z\alpha)^4} = (Z\alpha)^6 m\alpha^2 \tag{4.87}$$

Evalution of the 2E1 decay rate now involves summing over the p-wave states, integrating over the continuum states, squaring the result and integrating over the frequency of one emitted photon. It should be obvious that a numerical approach is best suited here as it allows the inclusion of many p-wave states, and numerical integration. As we will later be interested in generalizing this approach to the finite-size nuclear affects (where we will have discretized the radial coordinate in order to iteratively solved the Schrödinger equation), it will be handy to use techniques that will generalize easily. Thus we want to approximate our integrals by sums over discrete sets. For the moment, we will use the analytic results above, and discretize the integral over the fractional photon energy y. This is done by defining a uniformly distributed 1 x m array with values $0 \leq y \leq 1$. As the radial matrix elements are know (Eqs. 4.78 and 4.79), we can approximate the integral crudely as a sum of rectangles. If we denote the integral by f(y), and our array of fractional photon energies by y(i), with $1 \leq i \leq m$ indexing array positions, we have

$$\begin{aligned} \Gamma_{2E1} &= \frac{4}{27\pi}\omega_0^5 \alpha^2 a_Z^4 \int_0^1 f(y) dy \\ &\approx \frac{4}{27\pi}\omega_0^5 \alpha^2 a_Z^4 \sum_{i=1}^{m} f(y(i)) \times \frac{1}{m} \end{aligned} \tag{4.88}$$

where $f(y(i))$ is the value of the integrand evaluated at array position i, and $1/m$ is the width of the rectangle (the discretized dy line element). For our purpose, we have taken the number of rectangles to be $m = 10000$, and with reference to 4.7, we see that the curve does not change appreciably over the size 1/10 000.

We can also study how many p-wave states to include (i.e. up to a certain principal quantum number n_{max}). We have evaluated the 2E1 decay rate for $1 \leq n_{max} \leq 100$, with results summarized in table 4.3. The results have been written in SI units via division by $\hbar$ in order to compare our results against those from the literature.

For large n_{max}, our result is similar to that quoted in Johnson, $\Gamma_{2E1} = 8.2290 s^{-1}$, and including only the first 4-pwave states (up to R_{51}) gives an estimate accurate to roughly 6%.

4.3 The Two Photon Transition for the Perturbed Muonic Zirconium State

Our muonic zirconium scenario is slightly more complicated. Firstly, the $2s$ state only appears in our perturbation, so the actual energy available for the transition is the energy of nuclear excitation, which is smaller than the ususal $2s \to 1s$ energy by a factor of $\sim$2. Moreover, the muonic wavefunctions are significantly altered near the origin

Table 4.3: Two Photon transition rates for Hydrogen, varying the total number of p-wave states considered

Quantum Number "n_{max}"	Decay Width (s^{-1})
2	14.044
3	9.867
4	9.078
5	8.735
10	8.364
25	8.265
50	8.251
100	8.247

due to finite-size nuclear affects. Since the available transition energy is smaller by a factor of ~ 2, we might expect the result to be smaller by a factor of $\sim 2^5$, however the ratios $\omega_0 : E_n$ are also different, and hence the denominator of the function $F_{2s,1s}$ will behave differently, so it is important to evaluate the effect. The first effect should lessen the 2E1 transition more significantly than the M1 transition, as the 2E1 transition goes as ω_0^5, compared to the M1 transition, which goes as ω_0^3. The second effect turns out to have order one changes to the radial matrix elements, but the effect of the energy ratios in the denominator on the final result is harder to estimate. We will see that the first effect has the most significant impact, and hence we expect the M1 decay width should be larger than the 2E1 decay width. For convenience, we will refer to the usual $2s \to 1s$ transition in a hydrogen-like atom as the regular two photon transition. We will also refer to the muonic zirconium transition $|100\rangle|1\rangle \to |100\rangle|0\rangle$ as the muonic zirconium transition.

Taking into account the changes discussed above means that our transition rate formula becomes

$$\Gamma_{2E1} = \frac{1}{2}\int_0^{E_{Nuc}} d\Gamma(\omega) = \frac{4}{27\pi}\int_0^{E_{Nuc}} \omega^3 (E_{Nuc}-\omega)^3 \alpha^2 |F_{2s,1s}(\omega) + F_{2s,1s}(\omega_0-\omega)|^2 d\omega \tag{4.89}$$

where the function $F_{2s,1s}(\omega)$ is now given by

$$\begin{aligned} F_{2s,1s}(\omega) &= \sum_{n=2}^{\infty} \frac{\langle R_{1s,FS}|r|R_{n1,FS}\rangle\langle R_{n1,FS}|r|R_{2s,FS}\rangle}{E_n - (E_1+E_{Nuc}) + \omega} + \int \frac{\langle R_{1s,FS}|r|R_{q1,FS}\rangle\langle R_{q1,FS}|r|R_{2s,FS}\rangle}{E_q - (E_1+E_{Nuc}) + \omega} dq \\ &\approx \sum_{n=2}^{\infty} \frac{\langle R_{1s,FS}|r|R_{n1}\rangle\langle R_{n1}|r|R_{2s,FS}\rangle}{E_n - (E_1+E_{Nuc}) + \omega} + \int \frac{\langle R_{1s,FS}|r|R_{q1}\rangle\langle R_{q1}|r|R_{2s,FS}\rangle}{E_q - (E_1+E_{Nuc}) + \omega} dq \end{aligned} \tag{4.90}$$

There are two changes to the formula in the first line. We have introduced the subscript FS (Finite Size) on all the radial wavefunctions, to indicate that they are in fact the numerical solutions incorporating the finite size nuclear effects. Secondly, as mentioned above, our original state is actually given by $\psi_i \approx |100\rangle|1\rangle + \epsilon_{i,1s}|100\rangle|0\rangle + \epsilon_{i,2s}|200\rangle|0\rangle + \ldots$, so that the actual energy of the original state is $E_1 + E_{Nuc}$ instead of E_2. In the second line, we have replaced the finite size p-wave states by their hydrogen-like counterpart. As we previously saw, finite size does not have a significant effect on the non s-wave states, thus we can replace them with their hydrogen-like solutions for convenience. We also do this for the continuum p-wave states. As before, we will factor out all energies from the differential decay rate in order to make our integrand dimensionless. The result is identical to Eq. 4.84 with the replacement $\omega_0 \to E_{Nuc}$, except that the functions $G_{2s,1s}(y)$ are given by

$$G_{2s,1s}(y) = \sum_{n=2}^{\infty} \frac{\langle R_{1s,FS}|r|R_{n1}\rangle\langle R_{n1}|r|R_{2s,FS}\rangle}{1.0699 - 2.5578/n^2 + y} + \int_0^{\infty} \frac{\langle R_{1s,FS}|r|R_{q1}\rangle\langle R_{q1}|r|R_{2s,FS}\rangle}{2.5564q^2 + 1.0699 + y} dx \tag{4.91}$$

The numbers in the denominators are the relevant energy quantities, normalized by the transition energy, E_{Nuc}. For example, the discrete case has the energy factor

$$\begin{aligned} E_n - (E_1+E_{Nuc}) + \omega &= E_{Nuc}\left(\frac{E_n}{E_{Nuc}} - \frac{E_1}{E_{Nuc}} - 1 + \frac{\omega}{E_{Nuc}}\right) \\ &= E_{Nuc}\left(\frac{-4503.53\text{keV}/n^2}{1760.71\text{keV}} - \frac{-3596.20\text{keV}}{1760.71\text{keV}} - 1 + y\right) \\ &= E_{Nuc}(-2.5578/n^2 + 2.0699 - 1 + y) \end{aligned} \tag{4.92}$$

where we have used $E_n = m_\mu(Z\alpha)^2/2$ for the energies of the p-wave states, and the numerical energies for E_1. The case for the continuum is similar. We quickly note that all intermediate p-wave states must be virtual so

there is no possibility of resonance because there are no p-wave states with energies in between the energy of the initial state (ψ_i), and the full ground state (ψ_f). Had we been interested in the 2E1 transition of the actual muonic 2s state to the ground state (both being in the nuclear ground state), then we do get a resonance term because $E_1 < E_{2p} < E_{2s}$, with $E_{2s} - E_{2p} \approx 125$ keV. Hence in the $|200\rangle|0\rangle \to |100\rangle|0\rangle$ we can have a cascade where the 2s state can decay to the 1s state via a real intermediate 2p state, that is, two distinct electric dipole transitions $2s \to 2p \to 1s$. The real intermediate 2p state is in contrast to the virtual 2p states in the treatment done above for the 2E1 transition.

In order to compute Eq. 4.91, we discretize the radial position (r), the momentum space (q), and finally the fractional photon energy space (y). As before we will want to work in units where $a_{Z,\mu} = 1/(Z\alpha m_\mu) = 1$. In order to understand how "pixelated" our spaces should be (i.e. the step size for each space), we can gain some intuition from the hydrogen case studied above. We need to compute three nested integrals, first over the radial space to find the radial matrix elements, then over the momentum space, and finally over the fractional photon energy.

We first focus on the discrete-continuum integral, given by the second term in Eq. 4.91. Although it seems like we should first study the radial integrals, it will prove simpler to first understand the momentum integrand. For simplicity, define

$$A_{FS}(q) \equiv \frac{\langle R_{1s,FS}|r|R_{q1}\rangle\langle R_{q1}|r|R_{2s,FS}\rangle}{2.05564q^2 + 1.0669 + y} \qquad A_{PL}(q) \equiv \frac{\langle R_{1s,PL}|r|R_{q1}\rangle\langle R_{q1}|r|R_{2s,PL}\rangle}{\frac{4q^2}{3} + \frac{1}{3} + y} \tag{4.93}$$

The functions $A_{FS}(q)$ and $A_{PL}(q)$ are plotted in figure 4.3 and 4.6 for 3 values of the fractional photon energy, y. Importantly, both functions drops off significantly for momentum $q \geq 1$ and is nearly vanishing for $q \geq 5$. In the analytic case, roughly 2% of the total area exists in the interval $q \in (1, \infty)$, whereas only 3×10^{-5}% of the area exists in the interval $q \in (5, \infty)$ (these numbers do not depend significantly on the values of y). Since both curves display similar behaviour, we can impose a momentum cut-off scale at $q_{max} = 5$. There is nothing particularly special about the cut-off scale chosen, a smaller or larger value of q_{max} could be chosen, as long as the majority of the integrated curve is contained before q_{max}. In other words, we need $\int_0^{q_{max}} A(q)dq$ to be very small. Although finite size effects push the peak of $A_{FS}(q)$ further our compared to its pointlike counterpart, we can still impose a momentum cutoff at which point the continuum states do not contribute significantly.

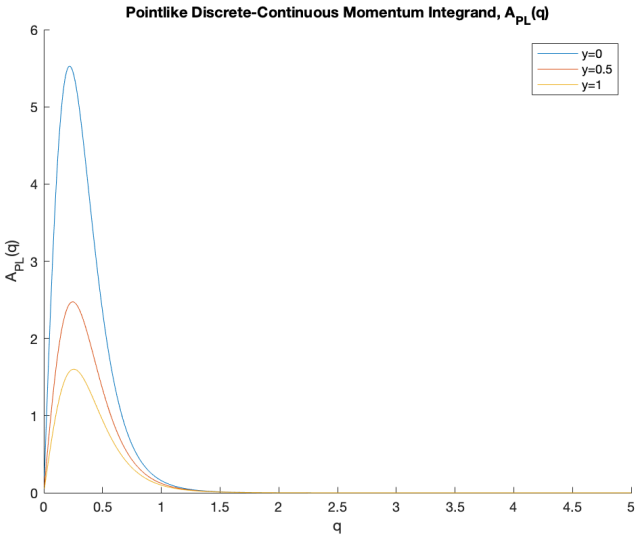

Figure 4.3: Analytic radial matrix elements for various values of fractional photon energy.

This also gives us a sense of the size of the discretization needed. Significant changes happen over the interval $q \in (0, 1)$, so our discretization size q_s must be satisfy $q_s \ll 1$. We choose to discretize the momentum line $(0, 5)$ into 1000 steps, so that the step size is $q_s = 1/200 \ll 1$.

We now study the radial integral and radial matrix element integrals. In order to properly discretize the space, we need to understand the characteristic size of the s-wave bound states and the continuum wavefunctions. We already know that the characteristic size of the s-wave bound states is comparable to the Bohr radius (recall we are using units where $a_Z = 1$). Although our numerical solutions are significantly differently near the origin, they display similar exponential decay behaviour outside a distance comparable to the Bohr radius. A selection of various continuum wavefunctions for $0 \leq q \leq 5$ are displayed below

As expected, states with higher momentum oscillate more rapidly in the radial space. We need to integrate over all possible momentum states, so naively it would seem like discretizing the radial position is impossible

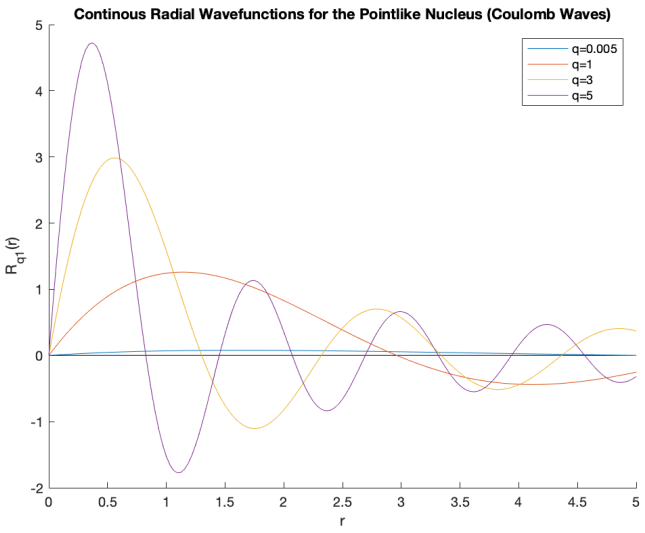

Figure 4.4: Radial wavefunctions for the continuum states, for momentum $0 \leq q \leq 5$. We have zoomed in on the region $0 \leq r \leq 5$ to better show the oscillation rate of higher momentum waves.

because there are always momentum states which oscillate more rapidly than any potential radial step size. However we also expect that when the momentum is larger enough, the oscillations occur on a radial scale much smaller than the Bohr radius, so their contribution becomes insignificant to the momentum integral. This is where the study of the momentum integrand $A_{PL}(q)$ becomes useful. Recall we have seen that the analytic expression for $A_{PL}(q)$ is greatly suppressed for momentum $q \gtrsim 5$. Glancing at figure 4.4, it is not obvious to see why this is the case for momentum $q \gtrsim 5$, since the continuous wavefunction with momentum $q = 5$ oscillates on a scale comparable to the Bohr radius. We need to also consider other factors in the integrand, a factor of r from the dipole operator, and a factor of r^2 from the volume factor. Taking these factors into effect, we see the r^3 factor effectively spreads out the scale on which the non-continuum part of the integrand (i.e. $r^3 R_{10}(r)$) is significant. In other words, the characteristic scale of $\psi_{1s}(r)r^3$ is larger than the Bohr radius, see figure 4.5a. Hence the oscillations of the continuum wavefunctions become quick compared to the scale of the rest of the integrand, which results in a significant suppression. For a graphical perspective, the integrand of the radial matrix element $\langle R_{10}|r|Rq1\rangle$ is depicted in figure 4.5, comparing momentum values $q = 0.5$ and $q = 5$ (values near the peak and far along the tail of the function $A_{PL}(q)$, see figure 4.3). The blue curve depicts the matrix element for a low momentum continuous wavefunction. The red curve displays the matrix element for a $q = 5$ momentum continuous wavefunction, and we can see that the oscillations are much quicker than the previous case. It is easy to see why this contribution is suppressed compared to the low momentum state, the quicker oscillations result in the cancellations discussed above. Although this is graphically depicted for the $1s$ wavefunction, the $2s$ state behaves in a similar manner.

Now that we have more understanding of the characteristic size of the continuum wavefunctions, we are in a position to discretize the radial space. We have just seen that there is a oscillatory suppression in the radial matrix elements for larger momentum values, and we have imposed a momentum cut-off at $q = 5$. Hence the smallest scale of interest results from the integrand containing the $q = 5$ continuum radial wavefunction, depicted in figure 4.5b. We see the oscillations occur on the scale $r \sim 1$ hence our radial step size r_s should satisfy $r_s \ll 1$. From our numerical solutions to the finite nuclear size, the muon wavefunction values extend out to $r \approx 40$. With this in mind, we choose the discretize the radial space in 1000 steps, so that the step size is $r_s = 1/25 \ll 1$. Although it may seem like we should choose a smaller step size to get more accurate results, we will find that this approximation will be suitable (later we estimate this contributes a 2% error to the total decay rate). One reason not to choose a significantly smaller step size is that computation requires evaluating a hypergeometric function (part of the continuum radial wavefunctions) on an already 1000 x 1000 array (over q and r discrete values), which takes some time in MATLAB.

We can perform the radial integral and plot the resulting momentum spectrum, comparing it to the analytic results we had previously studied. It is important to note that these are displayed for the regular $2s \to 1s$ transition in the hydrogen-like atom. The curves do not match exactly (as depicted in figure 4.6a), but are very close. Although a smaller radial step size would bring these curves closer together, it is an extremely small effect.

The equivalent curve for the excited muonic zirconium two-photon transition displays similar behaviour, although the shape is slightly different near the tail due to the finite nuclear size effects of the s-wave wavefunctions, and also the ratio of the energies as compared to the transition energy. The muonic curve is also significantly smaller than the regular two photon curve, this is primarily due to the energy ratios.

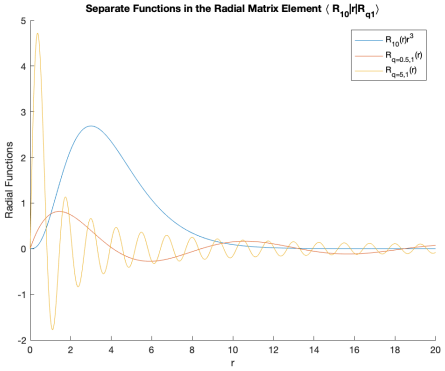

(a) Factors in the radial integrand

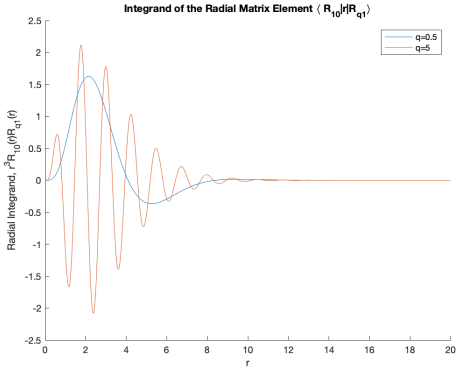

(b) The full radial integrand

Figure 4.5: The first figure (left) displays the "spreading" effect of the r^3 term on the muonic 1s wavefunction, and compares the size of the resulting function to the size of two continuum radial wavefunctions. The second figure (right) displays the oscillatory behaviour of the radial integrand for the same two continuum radial wavefunctions. The momentum values are chosen so that the resulting value of the integral is near the peak ($q = 0.5$) of the spectrum in figure 4.3, where as the other is far out on the tail to the right ($q = 5$)

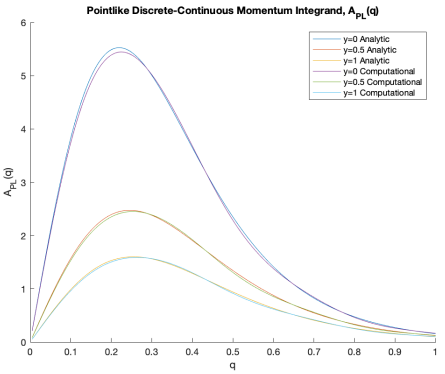

(a) Analytic and computational momentum integrand $A_{PL}(q)$ for the pointlike nuclear two photon decay

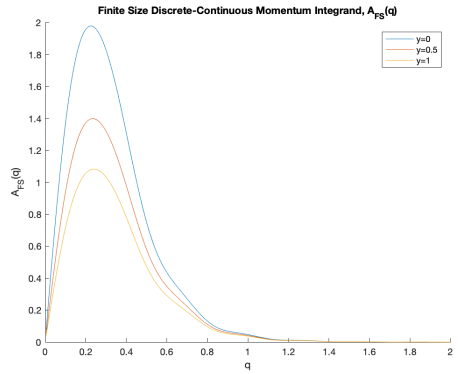

(b) Computational momentum integrand $A_{FS}(q)$ for the two photon decay in muonic zirconium

Figure 4.6: The first figure (left) displays the comparison between the analytic and computational methods used to compute the momentum integrand, $A_{PL}(q)$ for a few different values of the fractional photon energy y. Note that the analytic results are the same as those displayed above in figure 4.3, and we have now included the computational results derived using the discretization discussed above. We have only shown momentum values $q \in (0, 1)$ to better display the differences between the analytic and computational results. The second figure (right) displays the same momentum integrand, but as applied to the muonic zirconium transition, $A_{FS}(q)$. The differences arise due to the different energy ratio that appears in the denominator (cf. Eq. 4.93) and the fact that we are using the finite size s-wave states. We show the integrand for momentum values $q \in (0, 2)$ to highlight the differences, since the integrand displays similar suppression for $q \geq 2$ as in the regular two photon case.

Once these integrals are done, we also have to discretize the fractional photon energy space. The resulting differential photon energy distribution, $f(y) \equiv y^3(1-y)^3|G_{2d,1s}(y) + G_{2d,1s}(1-y)|^2$ (the dimensionless integrand appearing in Eqs. 4.91 and 4.84) is plotted for the regular hydrogen-like $2s \to 1s$ and the muonic zirconium two photon transitions in figure 4.7. Note that both these curves were generated by only taking into account the first 4 p-wave states.

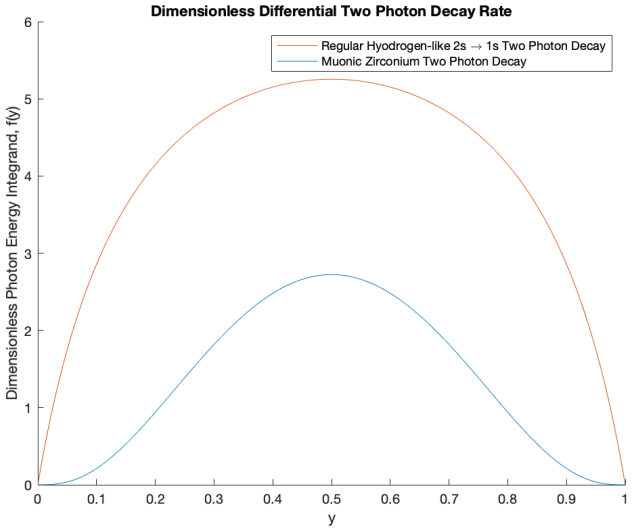

Figure 4.7: Dimensionless differential decay rate for the regular hydrogen-like $2s \to 1s$ and muonic zirconium two photon transition, using intermediate p-wave bound states up to n = 5 ($n_{max} = 5$)

Both curves are symmetric about $y = 0.5$ due to the symmetry of $y \to (1-y)$ which leaves the integrand invariant. There are two important features of the muon curve that are different from the regular $2s \to 1s$ two photon curve, the maximum height of the curve, and its behaviour near the endpoints. Both arise from the same consideration: the energy ratios appearing in the original matrix element (Eq. 4.62). In the regular case, the contribution of the $2p$ states are very important. The energy of the intial $2s$ and intermediate $2p$ state are equal in the pointlike analysis (hence the factor of $1/4 - 1/n^2$ in Eq. 4.84), so for small y the function $|G_{2s,1s}(y)|^2$ behaves as $1/y^2$. Near the origin, the other important factor is the y^3 factor, which yields linear behaviour. However in the muonic case, the initial energy is due to the muonic ground state and the nuclear excitation energy, which does not cancel with the energy of the $2p$ state (the energy difference is $1.0699 - 2.5578/n^2 \neq 0$ in Eq. 4.91). Hence for small y the contribution of the $2p$ state (and all p-wave states) is just a constant, so the function behaviour is mainly due to the y^3 term, which is reflected in the cubic behaviour of the muon curve (more suppression at the origin). The fact that the total height of the curve is smaller is likely due to the same reason, together with a difference in the radial matrix elements. To see this, the contribution to the regular curve at midpoint $y = 0.5$ from only the 2p bound state is given by

$$\frac{\langle R_{1s}|r|R_{21}\rangle\langle R_{21}|r|R_{2s}\rangle}{E_{2p} - E_{2s} + 0.5} \approx -13.4 \tag{4.94}$$

whereas the contribution to the muonic curve is at the same point is given by

$$\frac{\langle R_{1s,FS}|r|R_{21}\rangle\langle R_{21}|r|R_{2s,FS}\rangle}{E_{2p} - (E_{1s} + E_{Nuc}) + 0.5} \approx -9.4 \tag{4.95}$$

We see the point on the regular curve is larger by $13.4/9.4 \approx 1.4$. A similar decrease by a factor of roughly 2.7 is observed in the continuous Coulomb wave contribution, as seen in figure 4.6. From figure 4.7, we see the regular curve is larger by approximately $5/3 \approx 1.7$, which is probably a weighted average of the two contributions.

There is another effect which could cause the suppression of the muonic curve. In the regular hydrogen-like case, there is destructive interference between the $2p$ and other p-wave states. The $2p$ state is so dominant because (as mentioned above) there is a cancellation between energy factors in the denominator. In the muon case, we do not have this cancellation, so it is suspected that the $2p$ contribution is not as dominant, and the interference from the other p-wave states would be more significant, causing the curve to be lower.

In order to evaluate the integral over the photon energy, we discretize the fractional photon energy into 10 000 steps, since this integral is computationally simple. It should be clear that this produces a step size y_s that is smaller than any scale appearing in figure 4.7. Writing

$$I = \int_0^1 y^3(1-y)^3|G_{2s,1s}(y) + G_{2s,1s}(1-y)|^2 dy \tag{4.96}$$

and referring back to Eqs. 4.84 and 4.91, we have the 2E1 decay rate as

$$\Gamma_{2E1} = \frac{4}{27\pi}\omega_0^5\alpha^2 a_{Z,\mu}^4 \times I \tag{4.97}$$

where we have converted back to natural units by multiplying by a_Z^4. We now need to add the perturbative mixing depicted in figure 4.1. In a similar manner to the M1 transition, this modifies the decay rate by an additional factor of $|\epsilon_{f,2s} + \epsilon_{i,2s}|^2 = 1.67 \times 10^{-7}$. Evaluating the integral using the techniques developed above gives $I = 1.3616$. Substituting $E_{Nuc} = 1760.71\text{keV}$ and other relevant parameters gives the decay rate as

$$\begin{aligned}\Gamma_{2E1} &= \frac{4}{27\pi}\frac{(1760.71\text{keV})^5}{137^2}\frac{137^4}{(40 \times 105658\text{keV})^4} \times 1.67 \times 10^{-7} \times 1.3616 \\ &= 1.0732 \times 10^{-14}\text{keV}\end{aligned} \tag{4.98}$$

Converting this via $\hbar = 6.582 \times 10^{-16}\text{eV·s}$ gives the decay rate as

$$\Gamma_{2E1} = 1.63 \times 10^4 \text{s}^{-1} \tag{4.99}$$

Comparing this to the M1 transition, we see it is about an order of magnitude smaller

$$\frac{\Gamma_{M1}}{\Gamma_{2E1}} = \frac{2.28 \times 10^5 \text{s}^{-1}}{1.63 \times 10^4 \text{s}^{-1}} \approx 14 \tag{4.100}$$

4.3.1 Improvements on the Calculation

There are several sources of error that could be addressed.

- Firstly, one could include more p-wave bound states, since we have only summed over the first four. With reference to Table 1, including up to 100 p-wave states would decrease the decay rate by roughly 6% (assuming the higher p-wave states affect the muonic transition by a similar amount).
- Secondly, one could increase the number of steps in the discretization of the radial space, with the goal of more accurately matching the curves in figure 4.6a. As the approximate curve is larger, the contribution from the continuum states is overestimated. This continuum intermediate state integral destructively interferes with the bound-state sum, so it is difficult to understand how much this error contributes. Comparing the integrals of the analytic and approximate functions for fractional photon energies y = 0.1,0.2,...1 gives the average approximate integral to be roughly 10% larger than the analytic integral. For the hydrogen-like case, ignoring the continuum states gives a decay rate of approximately $10s^{-1}$, compared to the true decay rate of approximately $8s^{-1}$. This leads us to believe that the effect of the continuum states decreases the overall decay rate by approximately 20%. Multiplying these factors together yields the naive estimate that the discretization error would increase the decay rate by approximately $0.2 \times 10\% = 2\%$.
- In our derivation, we made the approximation $e^{ikr} \approx 1$, which is valid for $1/(Z\alpha) >> 1$. For muonic zirconium, Z = 40, so $1/(Z\alpha) \approx 3.4$. Therefore other terms in the exponential expansion could also contribute.
- One could also numerically solve the Schrödinger equation for the positive energy Coulomb wavefunctions using the finite size potential. This effect is likely insignificant compared to the others, since only the p-wave positive energy solutions are used, which are not effected significantly by the finite size effect.
- Lastly, one could do this computation using the relativistic framework. Johnson [36] notes that the relativistic treatment decreases the 2E1 decay rate for hydrogen-like atoms by approximately 7.4% (for Z=40, using linear interpolation between the Z = 38 and Z = 42 results).

Since all these errors contribute less than 10% each, they would not change the result of the 2E1 transition rate being a factor of ~ 10 smaller than the M1 transition rate.

4.4 Comparison to the Electron Electric Monopole Transition

We have been considering the muonic zirconium atom as if the muon is the only orbiting particle, because its Bohr radius is significantly smaller then the electronic Bohr radius, so the presence of the electrons is not appreciably felt by the muon. However there are still 2 electrons which occupy the $|100\rangle|1\rangle$ state which means there are four competing methods we have considered for nuclear de-excitation:

1. E0 transition due to electrons

2. Electron-Positron pair production

3. M1 transition due to the muon

4. 2E1 transition due to the muon

There is actually another way the muonic atom in the nuclear ground state can be destroyed, via weak muon capture. The muon can interact with a proton via a W^+ boson, converting the proton to a neutron and the muon into a muon neutrino. For the case of zirconium, the experimental lifetime for weak muon capture is 110.4ns [37], which is roughly twice as large as the lifetime of the excited nuclear state, so this does not pose a significant issue.

We have the decay rate for each of the above transitions, so we can compare them to determine their relative probabilities. Before doing this, we quickly note that due to screening, the electronic E0 transition in this case is not the same as in the previous case. The probability that the muon is within the electron Bohr radius is given by (assuming Schrödinger wavefunctions) is given by

$$\begin{aligned} P &= \int_0^{a_{Z,e}} |R_{10,\mu}(r)|^2 r^2 dr \\ &= \frac{4}{a_{Z,\mu}} \int_0^{a_{Z,e}} r^2 \exp(-2r/a_{Z,\mu}) dr \\ &= 1 - e^{-2m_\mu/m_e}\left[1 + 2\frac{m_\mu}{m_e} + 2\frac{m_\mu^2}{m_e^2}\right] \\ &= 1 - 2 \times 10^{-175} \end{aligned} \tag{4.101}$$

The nuclear charge is effectively screened by the entire muon charge, so the orbiting electron feels a charge of $Z_{eff} = 39$. Since the E0 transition behaves as Z^3 in its most simple form (plane wave Schrödinger approximation, see section 2.2), we will modify the E0 decay rate by a factor of $(Z_{eff}/Z)^3 = (39/40)^3 = 0.9269$. Screening also affects the electron-positron pair production ratio. Based on the work of Thomas [22], as well as Soff et al. [38], the pair production rate approximately increases linearly with atomic charge, so the pair production decay rate would be modified by a factor of $Z_{eff}/Z = 39/40 = 0.975$

This transition rates are thus

$$\begin{aligned} &\Gamma_{E0,e,Z_{eff}=39} = 0.9269\Gamma_{E0,e,Z=40} = 1.05 \times 10^7 \text{s}^{-1} \\ &\Gamma_{PP,e,Z_{eff}=39} = 0.975\Gamma_{PP,e,Z=40} = 4.34 \times 10^6 \text{s}^{-1} \\ &\Gamma_{M1,\mu} = 2.28 \times 10^5 \text{s}^{-1} \\ &\Gamma_{2E1,\mu} = 1.63 \times 10^4 \text{s}^{-1} \\ &\Gamma_T = \Gamma_{E0,e,Z_{eff}=39} + \Gamma_{PP,e,Z_{eff}=39} + \Gamma_{M1,\mu} + \Gamma_{2E1,\mu} = 1.51 \times 10^7 \text{s}^{-1} \end{aligned} \tag{4.102}$$

Note that both the electronic transitions produce unbound electrons (and positrons in the pair production case). The muon decay also produces electrons and neutrinos. The E0 transition would give a sharp spectrum with ejected electron having energy $E_f = 1739$keV, whereas the pair production would give a continuous spectrum with maximum energy of 717keV.

In contrast, both the muon transitions involve emitted photons. The M1 transition would give a sharp spectrum at 1760.71keV, whereas the two photon transition would give a continuous spectrum with a maximum photon energy 1760.71keV, and a peak at 880.34keV. Since we want to make a measurement of a muonic transition, the ideal observable would be the M1 photon since it is mono-energetic and it corresponds to the most probable muonic transition.

Unfortunately, the M1 decay occurs rarely in comparison to the electron decays. Compounded with the probability of populating the $|100\rangle|1\rangle$ state being roughly $5 \times 10^{-6}\%$, we would need a significant experimental run time to achieve reasonable statistics.

4.5 A Quick Note on Parity Violating Effects

We previously mentionned that forbidden M1 transitions are interested due to parity violating effects. Having developed the perturbative mechanics necessary to describe the muonic system, we are now in a position to elaborate further. Recall that the nuclear excited state and full ground states only admitted mixing with other muonic s-wave state, see figure 4.1. This was due to the orthogonality of the spherical harmonics, relying on parity. If O is a parity violating operator arising from neutral currents, then the initial and final states will be

$$\begin{aligned} \psi_i &\equiv |100\rangle|1\rangle + \epsilon_{i,1s}|100\rangle|0\rangle + \epsilon_{i,2s}|200\rangle|0\rangle + \epsilon_{i,2p}|210\rangle|0\rangle + \cdots \\ \psi_f &\equiv |100\rangle|0\rangle + \epsilon_{f,1s}|100\rangle|1\rangle + \epsilon_{f,2s}|200\rangle|1\rangle + \epsilon_{f,2p}|210\rangle|1\rangle \cdots \end{aligned} \tag{4.103}$$

where $\epsilon_{i,f,2p}$ are the perturbative mixing parameters induced by the operator O. Since we now have mixing involve p-wave states, it is now possible to have en electric dipole transition, with matrix element

$$(\epsilon_{i,2p} + \epsilon_{f,2p})\langle 100|r|210\rangle \tag{4.104}$$

Although the perturbative mixings $\epsilon_{i,f,2p}$ will be small because parity violating operators are already constrained, the E1 transition is significantly faster than the other modes of nuclear de-excitation. Observations (or lack thereof) of this E1 transition would give constraints on the operator O.

Chapter 5

Transition Energy Variation due to Excited Nuclear Charge Radius

In the analysis above, we discussed the observable photon radiation from the M1 transition, with photon energy equal to the nuclear de-excitation energy. In both the initial and final states, the muon is in the $1s$ state, so the only energy available comes from the nuclear de-excitation. This is only an approximation, however, because the binding energy is not only dependent on the total charge, but also on the charge radius of the nucleus as we saw in Chapter 3. In the initial state, the muon's binding energy will change slightly if the charge radius of the excited nuclear is different than the charge radius of the ground state. In particular a larger charge radius will yield a lower binding energy. This follows from our numerical finite nuclear size binding energies which are lower than the corresponding pointlike nuclear binding energies. The final state muon state is bound to the nuclear ground state, and hence its binding energy is as calculated above (see table 3.1). Hence the actually transition energy would be modified slightly from E_{Nuc} to something slightly larger. We expect the nuclear excited state would have a slightly larger charge radius, implying a smaller binding energy for the intial state, and hence a transition energy which is slightly larger than the nuclear de-excitation energy. If we can observe a difference, the size of the difference will be able to give us information on the nuclear charge radius of the excited state.

We want to investigate the change in the transition energy for a small change in the charge radius. Quantitatively, we want to find the coefficient C in the expression

$$C\frac{dE}{dR_{Nuc}} = \frac{E_{Nuc}}{R_{Nuc}} \tag{5.1}$$

Since we dont have an analytic expression for the binding energy, we will approximate this by solving the Schrödinger equation using a charge distribution with a nuclear radius given by $R'_{Nuc} = R_{Nuc} + \Delta R$, and finding a ground state energy of $E'_{1s} = E_{1s} + \Delta E$. In the previous expressions, the superscript $'$ denotes parameters corresponding to the nuclear excited state. As discussed above, ΔR is a positive quantity, and because the binding energy is smaller, ΔE is positive (since E_{1s} is negative). Rearranging our previous expression yields

$$C = \frac{E_{Nuc}}{R_{Nuc}}\frac{\Delta R}{\Delta E} \tag{5.2}$$

Using $\Delta E = E'_{1s} - E_{1s}$, and $\Delta R = R'_{Nuc} - R_{Nuc}$, we can solve for the coeffcient C via

$$\begin{aligned} C &= \frac{E_{Nuc}}{E'_{1s} - E_{1s}}\frac{\Delta R}{R_{Nuc}} \\ &= \frac{E_{Nuc}}{E'_{1s} - E_{1s}}\frac{R_{\%}}{100} \end{aligned} \tag{5.3}$$

where $R_{\%} = \Delta R/R_{Nuc} \times 100\%$ is the percentage increase in the nuclear charge radius. Solving this relation with a one percent increase in the nuclear charge radius ($R_{\%} = 1\%$) yields the coefficient

$$C = 2.24 \tag{5.4}$$

Note that this implies a 1% change in the nuclear radius gives a binding energy change of $\Delta E = 7.86$keV, or a 0.45% change. In principle, we could introduce this change in energy to the de-excitation calculations done in the previous section, however the effect would not be significant. We can also use this to determine how sensitive observations are to an increase in the nuclear radius. If an experiment is sensitive to changes in photon energy

of ΔE, then the smallest percent change in the nuclear charge radius is given by

$$\begin{aligned} R_{\%} &= C\frac{\Delta E}{E_{Nuc}}100\% \\ &= 2.24\frac{\Delta E}{1760.71\text{keV}}100\% \\ &= 0.127\%\frac{\Delta E}{\text{keV}} \end{aligned} \tag{5.5}$$

Experiments which are less sensitive to photon energy changes are less sensitive to changes in the nuclear radius, as expected. Typical Germanium detectors have a photon resolution on the order of a few keV [39], which means they would be sensitive to changes in the nuclear radius on the order of 0.2-0.5%.

The High Intensity Proton Accelerator (HIPA) facility at the Paul Scherrer Institute (PSI) typically produces order 10^4 muons/s [39], but is capable of producing 10^6 muons/s. Since the probability of a muonic atom populating the nuclear excited state and subsequently undergoing the M1 transition is roughly 10^{-9}, we would obtain an M1 photon once every 10^3s $\approx$ 17 minutes, or approximately 10 M1 photons every 3 hours, at 10^6 muons/s.

Chapter 6

Conclusion

We began by studying the electron undergoing an electric monopole transition in zirconium in order to develop a perturbative approach to treat the muonic atom. We compared our E0 perturbative model to the more common approach, highlighting why our model was better suited to treat the muonic atom. We then studied how to populate the muonic excited nuclear state, starting from the $2p$ or $3p$ muonic states. After a quick calculation using the pointlike nuclear approximation, we found that finite nuclear size effects caused a significant decrease in the branching ratios by nearly 2 orders of magnitude, with the final branching ratios on the order of 10^{-8}. We then studied the decay channels of the excited nuclear state to gain insight into what the common signals associated with muonic transitions. We found that the mono-energetic M1 transition was the most significant muonic transition, followed by the two photon transition. Both muonic transitions involved photons, compared to the other transitions involving ejected electrons or electron-positron pairs, which made the signal easier to detect. However the M1 transition has a small chance of occurring, increasing the time necessary to run an experiment which produces a fixed number of muonic zirconium atoms per second. Lastly we studied the sensitivity of the physical transition energy to the charge radius of the excited state. We found that Germanium detectors, with a photon sensitivity of a few keV, would be able to detect a change in the nuclear charge radius as small as a few tenths of a percent.

In the present case the PSI experiment has the best experimental setup to perform this measurement, with Germanium photon detectors sensitive to 2-3keV and the experiment is capable of producing up to 10^6 muons/s. This yields approximately 10 M1 photons every 3 hours of experimental run time. Ultimately the low probability of populating the excited nuclear state results in current experiments requiring a long run time to get good statistics.

Bibliography

[1] Ernest Rutherford. Lxxix. the scattering of α and β particles by matter and the structure of the atom. *The London, Edinburgh, and Dublin Philosophical Magazine and Journal of Science*, 21(125):669–688, 1911.

[2] Niels Bohr. Xxxvii. on the constitution of atoms and molecules. *The London, Edinburgh, and Dublin Philosophical Magazine and Journal of Science*, 26(153):476–502, 1913.

[3] Erwin Schrödinger. An undulatory theory of the mechanics of atoms and molecules. *Physical review*, 28(6):1049, 1926.

[4] David J Griffiths. *Introduction to quantum mechanics*. Pearson, 2005.

[5] Stephen Gasiorowicz. *Quantum physics*. John Wiley & Sons, 2007.

[6] LD Landau and EM Lifshitz. Theoretical physics, vol. 3: Quantum mechanics. *Nonrelativistic Theory*, 1977.

[7] Vladimir Borisovich Berestetskii, Lev Davydovič Landau, Evgenii Mikhailovich Lifshitz, and LP Pitaevskii. *Quantum electrodynamics*, volume 4. Butterworth-Heinemann, 1982.

[8] Michael E Peskin and Daniel V Schroeder. An introduction to quantum field theory. 1995.

[9] Bruce R Barrett, Petr Navrátil, and James P Vary. Ab initio no core shell model. *Progress in Particle and Nuclear Physics*, 69:131–181, 2013.

[10] Kenneth S Krane, David Halliday, et al. *Introductory nuclear physics*. 1987.

[11] H Backe, R Engfer, E Kankeleit, R Link, R Michaelsen, C Petitjean, L Schellenberg, H Schneuwly, WU Schröder, JL Vuilleumier, et al. Nuclear excitation and isomer shifts in muonic atoms:(i). experiment and evaluation. *Nuclear Physics A*, 234(2):469–503, 1974.

[12] Michael Nessin, TH Kruse, and KE Eklund. Nuclear electric monopole transitions in o 16, ca 40, ge 72, and zr 90. *Physical Review*, 125(2):639, 1962.

[13] RP Singhal, SW Brain, CS Curran, WA Gillespie, A Johnston, EW Lees, and AG Slight. Inelastic scattering of electrons for 90zr. *Journal of Physics G: Nuclear Physics*, 1(5):558, 1975.

[14] Kurt Alder and Rolf M Steffen. Electromagnetic moments of excited nuclear states. *Annual review of nuclear science*, 14(1):403–482, 1964.

[15] D Burch, P Russo, H Swanson, and EG Adelberger. Lifetime of the first excited state in 96zr. *Physics Letters B*, 40(3):357–359, 1972.

[16] Yasuyuki Nakayama. Two-photon decay of the 1.76-mev 0^+ state of ^{90}Zr. *Phys. Rev. C*, 7:322–330, Jan 1973.

[17] JM Dong, W Zuo, HF Zhang, W Scheid, JZ Gu, and YZ Wang. Correlation between muonic levels and nuclear structure in muonic atoms. *Physics Letters B*, 704(5):600–603, 2011.

[18] Aldo Antognini. Muonic atoms and the nuclear structure, 2015.

[19] EL Church and J Weneser. Electric-monopole transitions in atomic nuclei. *Physical Review*, 103(4):1035, 1956.

[20] David J Griffiths. Introduction to electrodynamics, 2005.

[21] Tibor Kibedi and Ray H Spear. Electric monopole transitions between 0+ states for nuclei throughout the periodic table. *Atomic Data and Nuclear Data Tables*, 89(1):77–100, 2005.

[22] R Thomas. Internal pair production in radium c′. *Physical Review*, 58(8):714, 1940.

[23] JR Oppenheimer and JS Schwinger. On pair emission in the proton bombardment of fluorine. *Physical Review*, 56(10):1066, 1939.

[24] Marco D'Arienzo. Emission of $\beta+$ particles via internal pair production in the 0+–0+ transition of 90zr: Historical background and current applications in nuclear medicine imaging. *zAtoms*, 1(1):2–12, 2013.

[25] Roger Boudet. A relativistic calculation of the matrix elements used in the photoeffect and the lamb shift. *Foundations of physics*, 29(1):49–66, 1999.

[26] EL Church and J Weneser. Electric-monopole transitions in atomic nuclei. *Physical Review Letters*, 100(3):943, 1955.

[27] TQ Phan, P Bergem, A Rüetschi, LA Schaller, and L Schellenberg. Nuclear polarization in muonic zr 90. *Physical Review C*, 32(2):609, 1985.

[28] K Alder and RM Steffen. The electromagnetic interaction in nuclear spectroscopy ed wd hamilton, 1975.

[29] J Chluba and RA Sunyaev. Two-photon transitions in hydrogen and cosmological recombination. *Astronomy & Astrophysics*, 480(3):629–645, 2008.

[30] N Bezginov, T Valdez, M Horbatsch, A Marsman, AC Vutha, and EA Hessels. A measurement of the atomic hydrogen lamb shift and the proton charge radius. *Science*, 365(6457):1007–1012, 2019.

[31] W Xiong, A Gasparian, H Gao, D Dutta, M Khandaker, N Liyanage, E Pasyuk, C Peng, X Bai, L Ye, et al. A small proton charge radius from an electron–proton scattering experiment. *Nature*, 575(7781):147–150, 2019.

[32] Beat Hahn, DG Ravenhall, and Robert Hofstadter. High-energy electron scattering and the charge distributions of selected nuclei. *Physical Review*, 101(3):1131, 1956.

[33] FA Parpia and AK Mohanty. Relativistic basis-set calculations for atoms with fermi nuclei. *Physical Review A*, 46(7):3735, 1992.

[34] BV Noumerov. A method of extrapolation of perturbations. *Monthly Notices of the Royal Astronomical Society*, 84:592–592, 1924.

[35] Anders W. Sandvik. Lecture notes in computational physics, Fall 2018.

[36] WR Johnson. Radiative decay rates of metastable one-electron atoms. *Physical Review Letters*, 29(17):1123, 1972.

[37] David F Measday. The nuclear physics of muon capture. *Physics Reports*, 354(4-5):243–409, 2001.

[38] Gerhard Soff, Paul Schlüter, and Walter Greiner. Internal electron-positron pair production from electric monopole transitions. *Zeitschrift für Physik A Atoms and Nuclei*, 303(3):189–198, 1981.

[39] A Antognini, N Berger, TE Cocolios, R Dressler, R Eichler, A Eggenberger, P Indelicato, K-P Jungmann, CH Keitel, K Kirch, et al. The measurement of the quadrupole moment of 185-re and 187-re from the hyperfine structure of muonic x rays. *arXiv preprint arXiv:2003.02481*, 2020.